Linear Aerospike Contour Design using Angelino's Method and CFD Validation

(versão final após defesa)

João Pedro Cristóvão Silva

Dissertação para obtenção do Grau de Mestre em
Engenharia Aeronáutica
(mestrado integrado)

Orientador: Prof. Doutor Francisco Miguel Ribeiro Proença Brójo

Covilhã, 12 julho de 2023.

Declaração de Integridade

Eu, João Pedro Cristóvão Silva, que abaixo assino, estudante com o número de inscrição 41136 do Mestrado Integrado em Engenharia Aeronáutica da Faculdade de Engenharia, declaro ter desenvolvido o presente trabalho e elaborado o presente texto em total consonância com o **Código de Integridades da Universidade da Beira Interior**.

Mais concretamente afirmo não ter incorrido em qualquer das variedades de Fraude Académica, e que aqui declaro conhecer, que em particular atendi à exigida referenciação de frases, extratos, imagens e outras formas de trabalho intelectual, e assumindo assim na íntegra as responsabilidades da autoria.

Universidade da Beira Interior, Covilhã 02/08/2023

Assinado por: **João Pedro Cristóvão Silva**
Num. de Identificação: 15735740
Data: 2023.08.02 13:13:13+01'00'

CHAVE MÓVEL

Dedication

For my parents

Acknowledgements

I would like to begin by expressing my gratitude to Professor Francisco Brójo, not only for his support throughout the development of this dissertation but also for the knowledge he imparted in the classroom that sparked my interest in the field of rocket science.

I am deeply grateful to my parents for their unwavering encouragement and for providing me with all the resources I needed to reach this point in my academic journey. I would also like to extend my thanks to my entire family for their support.

Lastly, I would like to express my heartfelt appreciation to my friends, who have become my chosen family. In particular, I would like to thank Pedro Nunes for his endless support, João Cleto for his constant presence and Beatriz ”Priscilla” Fernandes for her unwavering friendship.

Resumo

Veículos de estágio único para órbita (EUPO) têm o potencial de aumentar a confiabilidade do transporte espacial e reduzir os custos. No entanto, as tubeiras tradicionais cónicas e em formato de sino, têm uma capacidade limitada para fornecer um desempenho ideal em todo o envelope de voo. Como resultado, diversos designs avançados de tubeiras adaptativas à altitude têm sido propostos, entre os quais os conceitos de bocais em sino duplo, E-D e aerospike têm mostrado maior potencial. Esta dissertação concentra-se no aerospike, com o objetivo de projetar e avaliar um contorno utilizando ferramentas numéricas. Para atingir esse objetivo, o método de Angelino é implementado em Python para gerar o contorno para uma altitude operacional de 15545 metros, correspondente a uma razão de pressão (RP) de 188 no ponto de projeto. Os parâmetros fornecidos ao código incluem um Número de Mach à saída de 4,16, um índice adiabático de 1,4 e a especificação de 100 linhas de expansão. O processo de CFD, para os estudos numéricos que validam o contorno, é realizado no Ansys Workbench, especificamente utilizando o SpaceClaim para projetar a geometria do volume de controle e o Fluent para resolver o escoamento. No Fluent, é usado um solver baseado em densidade e dois modelos de viscosidade diferentes são considerados na análise: invíscido e realizable k-ε. Além das condições de projeto, três RP adicionais são simuladas: 20 (nível do mar), 288 (altitude de 18285 m) e 20480 (altitude de 47750 m). Concluiu-se que, tanto o modelo inviscido, quer o realizable k-ε, apresentam uma previsão de desempenho similar da tubeira à medida que o aerospike opera em diferentes altitudes, conforme indicado pelo impulso específico. Mas, foi o modelo realizable k-ε que demonstrou um maior nível de captura de detalhes de fenômenos do escoamento em comparação com investigações experimentais disponíveis. Inclui características como melhor caracterização do diamante de Mach e uma temperatura máxima registrada de mais de 7000 K. Em relação à adaptabilidade à altitude, a performance melhora com o aumento desta. Condições de subexpansão demonstraram um jato quase axial, destacando a capacidade do aerospike em manter a eficiência em altitude. Contudo, em sobreexpansão há um menor impulso específico. Estes resultados destacam as vantagens do aerospike em relação às tubeiras tradicionais, que geralmente têm maiores dificuldades em cenários de subexpansão.

Palavras-chave

EUPO (Estágio Único Para Órbita), Tubeiras de Foguete Avançadas, Aerospike Linear, Design de Contorno de Tubeira, Dinâmica dos Fluidos Computacional

Abstract

Single-stage-to-orbit (SSTO) vehicles have the potential to enhance space transportation reliability and reduce costs. However, traditional nozzles with conical and bell-shaped contours are limited in their ability to deliver ideal performance across the entire flight envelope. As a result, various advanced rocket designs with altitude adaptive characteristics have been proposed, among which the dual-bell, E-D, and aerospike concepts have shown the most promise. This dissertation focuses specifically on the aerospike concept, aiming to design and evaluate a contour using numerical tools. To achieve this objective, Angelino's method is implemented using Python to generate the aerospike contour for a specific operating altitude of 15545 meters, corresponding to a pressure ratio (PR) of 188 at the design point. The input parameters provided to the Python code include an exit Mach number of 4.16, an adiabatic index of 1.4 and the specification of 100 expansion lines. The CFD process for the numerical studies of the contour validation is performed using Ansys Workbench, specifically utilizing SpaceClaim for designing the control volume geometry and Fluent for solving the flow. In Fluent, a density-based solver is employed to analyze the flow behavior. Two different viscosity models are considered in the analysis: inviscid and realizable k-ε. In addition to the design conditions, three additional PR are simulated: 20 (sea-level), 288 (altitude of 18285 m), and 20480 (altitude of 47750 m). It was concluded that both the inviscid and realizable k-ε models exhibit a similar performance prediciton of the aerospike nozzle as it operates at different altitudes, as indicated by the specific impulse. Still, it was the realizable k-ε model that demonstrated a higher level of detail in capturing flow phenomena compared to available experimental investigations. This included features such as better modeled Mach diamond and a temperature distribution with values above 7000 K. Regarding the altitude adaptability of the aerospike nozzle, its performance was observed to improve with increasing altitude. Underexpanded conditions demonstrated a nearly axial exhaust plume, showcasing the aerospike's capability in maintaining thrust efficiency. In contrast, overexpanded conditions resulted in the lowest specific impulse. These findings highlight the advantages of the aerospike nozzle over traditional nozzles, which typically struggle in underexpansion scenarios.

Keywords

SSTO (Single-Stage-To-Orbit), Advanced Rocket Nozzle, Linear Aerospike, Nozzle Contour Design, CFD (Computational Fluid Dynamics)

Contents

List of Figures

List of Tables

Nomenclature

A	Area	m^2
a	Speed of Sound	m/s
C_F	Thrust Coefficient	-
C_p	Heat Capacity at Constant Pressure	J/K
c_p	Specific Heat Capacity at Constant Pressure	$J/(kg.K)$
C_v	Heat Capacity at Constant Volume	J/K
c_v	Specific Heat Capacity at Constant Volume	$J/(kg.K)$
ε	Turbulence Dissipation Rate	m^2/s^3
γ	Adiabatic Index	-
F	Force/Thrust	N
I_{sp}	Specific Impulse	s
I_t	Total Impulse	$N.s$
k	Turbulence Kinetic Energy	m^2/s^2
M	Mach Number	-
$\dot{m}$	Mass Flow Rate	kg/s
n	Quantity of Matter	mol
P	Pressure	Pa
ρ	Density	kg/m^3
Q	Heat	J
R	Universal Gas Constant	$J/(kg.K)$
Re	Reynolds Number	-
T	Temperature	K
t	Time	s
τ	Fluid Compressibility	Pa^{-1}
$\bar{\bar{\tau}}$	Viscous Stress Tensor	Pa
S	Entropy	J/K
U	Internal Energy	J
u	Axial Velocity	m/s
U^+	Dimensionless Velocity	-
V	Velocity	m/s
$\overrightarrow{V}$	Velocity Vector	m/s
v	Vertical Velocity	m/s
vol	Volume	m^3
ν	Prandtl Meyer Angle	$^{\circ}$
μ	Mach Angle	$^{\circ}$
μ_f	Dynamic Viscosity	$Pa.s$
μ_t	Turbulent Viscosity	$Pa.s$
y^+	Dimensionless Distance to the Wall	-
ω	Turbulence Specific Dissipation Rate	$1/s$

List of Acronyms

AUSM	Advection Upstream Splitting Method
CAD	Computer-Aided Design
CFD	Computational Fluid Dynamics
CTIC	Compressed Truncated Ideal Contoured
EUPO	Estágio Único Para Órbita
ISRU	In Situ Resource Utilization
MN	Mach Number
MNG	Multi Nozzle Grids
MOC	Method of Characteristics
ODE	Ordinary Differential Equation
PDE	Partial Differential Equation
PR	Pressure Ratio
RANS	Reynolds Average Navier-Strokes
RNG	Renormalization Group (Theory)
Roe-FDS	Roe Flux-Difference Splitting
SSTO	Single-stage-to-orbit vehicles
TIC	Truncated Idealized Contoured
TOC	Thrust Optimized Contoured

Chapter 1

Introduction

1.1 Motivation

Throughout human history, progress and the perpetuation of civilizations have been closely linked to territorial expansion, which brought resources and the promise of a brighter future. For millennia, the ocean was considered the frontier that only the bravest individuals dared to cross, but in today's global world, the aspirations of many now turn towards the stars.

In Situ Resource Utilization (ISRU) is a multidisciplinary field that aims to propose solutions for mining, farming and utilizing space resources. These resources are vast and include water, volatile compounds from the solar wind, metals, minerals, solar energy, vacuum and zero gravity environments. The current challenges associated with ISRU are immense. One of these challenges involves ensuring a profitable operation, making any contribution that optimizes the process highly valuable [1].

The reduction of Earth-to-orbit launch costs through the strengthening of reliability and operational efficiency is one of the major engineering problems space transportations currently faces.

Single-stage-to-orbit vehicles (SSTO) are an exemplary concept of space vehicles with simple and efficient system design. But conventional nozzles are unable to provide the highly required efficiency to propel these state-of-the-art vehicles.

Due to their fixed geometry that boundaries the flow, conventional nozzles can't compensate the varying pressure during the rocket's ascent. Many solutions have been proposed throughout the years, with plug nozzles, mainly aerospikes, being one of the most developed ideas [2].

Linear or toroidal, plug nozzles can compensate the pressure changes felt during a rocket's ascension, since the exhaust flow is asymmetrical, with a free shear layer in contact with the ambient air [3].

At low altitude operation, the aerospike behaves almost as the ideal nozzle and even the more significant losses felt at vacuum operation are overcome by the ability of providing bigger area ratios that conventional nozzle, with a much smaller weight, with an increment of 6-8% in specific impulse.

Aerospike advantages include the ability of vector thrusting, smaller weight, more average specific impulse, more efficient rocket structure and improved reliability. Besides SSTO, aerospikes have been proposed for more applications like CubeSat, interplanetary travel and even in defense, as air-to-air missiles are launch and target a wide range of altitudes [4].

The desire to make a contribution, no matter how small, to the advancement of civilization serves as a powerful motivation. It is this motivation that drives me to explore advanced rocket nozzle designs, particularly aerospikes, and focus the present dissertation around them. By studing aerospikes, I aim to contribute to the understanding and development of more efficient and effective rocket propulsion systems. Even a small advancement in this field can have a profound impact on space exploration.

1.2 Objectives

SSTO vehicles play a pivotal role in advancing space exploration. The main goal of the present dissertation is to understand how traditional rocket's nozzles prevent the creation of this type of vehicles and exploring the aerospike, out of many proposed alternatives, by designing a contour and evaluating its performance through the ascension of a rocket.

To clarify the scope and relevance of the dissertation, the path towards achieving the main goal is divided into several steps, which contribute to the learning process. These steps include:

1. Understanding the theoretical concepts of compressible aerodynamics and thermodynamics.
2. Grasping how rockets generate thrust and the associated phenomena of nozzle performance, leading to the realization of the incompatibility of conventional nozzles with SSTO vehicles.
3. Enumerating various altitude-adapting nozzle concepts, with a special focus on aerospike nozzles, while analyzing their advantages and disadvantages to justify the chosen nozzle typology for the study.
4. Gaining an understanding of the Method of Characteristics, particularly Angelino's Rapid Method, and its suitability for designing the aerospike contour.
5. Implementing a Python algorithm capable of effectively designing the aerospike contour.
6. Learning fundamental concepts of Computational Fluid Dynamics and turbulence.
7. Designing and meshing an optimized volume control for simulating the expansion of exhaust flow in the aerospike using Fluent.
8. Obtaining a convergent solution for the exhaust flow.

9. Analyzing the results for various operating conditions and simulation (viscous) options.

It is indeed a goal of this document to be written in a manner that facilitates future understanding of rocket propulsion, the limitations of conventional nozzles, the relevance of aerospike engines, and the ability to replicate the numerical studies conducted. The document aims to provide comprehensive explanations, clear methodologies, and detailed results to serve as a valuable resource for individuals seeking knowledge in this field.

1.3 Dissertation Structure and Layout

The present dissertation has six Chapters, with the first setting the motivation and objectives of the developed work. It also includes one Appendix.

The second Chapter begins by providing a brief overview of the history of rocket propulsion. Then, it presents a characterization of rockets and explores conventional nozzles, including the distinction between ideal and real nozzles and an analysis of conical and bell designs. An explanation of the altitude limitation of these designs is also boarded. It goes on to introduce many advanced nozzles with altitude-adapting capabilities and presents some conclusions on those currently under investigation. Among these designs, the aerospike nozzle is analyzed in a dedicated section, where its advantages and disadvantages are summarized and compared. Lastly, some nozzle design philosophies are outlined.

The third chapter, ”Theoretical Background,” furnishes a comprehensive explanation of the necessary theoretical concepts that are relevant to the interpretation and explanation of the developed work. It commences by introducing basic concepts related to thermodynamics and compressible aerodynamics. It then delves into a more detailed examination of the altitude limitation phenomenon in nozzles and the reasoning behind the Method of Characteristics. Finally, some considerations related to Computational Fluid Dynamics are explored.

The forth Chapter presents the ”Methodology” used to obtain the results, also including the parameters and justifications of the study. First, the contour design algorithm is explained, including the justification for the usage of Angelino’s simplified method as so the choosing of Python as the coding language. The chosen physical parameters for the study are presented preceded by the description of the most important steps of the CFD process using SpaceClaim, Mesh Generator and Fluent.

As for the fifth Chapter, the numerical results for several operating simulations (including design, underexpansion and overexpansion) of the designed aerospike contour are presented, both for an inviscid and turbulent viscous model. It also includes a through analysis and reflection of said results.

Lastly, the sixth chapter reflects the developed work, balancing the goals achieved, difficulties felt and ways to improve the study, further deepening it.

To note that Appendix A contains the Python's code used to design the spike's contour.

Chapter 2

State-of-the-Art

This chapter discusses the state-of-the-art of rocket nozzles with special emphasis to their design and adaptability to different altitudes. It begins with a brief overview of the history of rockets and and their characterization, delving into the conventional conical and bell nozzles.

The differences between the concept of an ideal nozzle and a real nozzle are also discussed in this Chapter.

Later on, advanced nozzle designs that are capable of adapting to different altitudes are presented, with a dedicated section to discussing aerospike nozzles.

At last, the main philosophies to design the contour of a nozzle are boarded and briefly explained.

2.1 Rocket's History

Rockets and their fundamentals have been around humankind history for a while, with their bigger developments being associated with warfare. Starting as bamboo tubes filled with gunpowder used in religous celebrities, primitive rockets are invented in the 1^{st} century China. "Arrows of flying fire", resembling solid propellant rockets, are used in 1232 by the Chinese army to repel the Mongol invaders.

There are many reports of the usage of primitive rocketry, specially in belic scenarios, and, in 1650, Kazimierz Siemienowicz publishes the sketches of a staged rocket. A few years later, the publications of the three laws of motion by Sir Isaac Newton, sets the physics background for modern rocketry.

It's in the 20th century that modern rockets are hard developed into almost nowadays technology, being propelled by the needs of World War Two and the Cold War. The rampage starts by the publication of rocket equations by russian Konstantin Tsiolkovsky in the begining of the century.

Robert H. Goddard, an american engineer, designs and builds the first liquid propellant rocket. 34 rockets where launch between 1926 and 1941, getting to altitudes of up to 2.6 km and speeds as high as 885 km/h. Later, in 1945, he creates single and multi-stage rocket engines for both rocket and jet-assisted takeoff.

But first, german engineer Wernher von Braun develops the V-2, a liquid-propellant rocket missile used by the Axis Forces in World War Two. In the after math of the war, von Braun is recruited by NASA where he becomes a prominent figure in the developing of the Saturn V launcher.

During the height of the Space Race, driven by the Cold War, the development of rocket technology reached its peak, resulting in several notable milestones[5]:

- **1957** – The launch of the first Earth-orbiting artificial satellite, Sputnik I, by the USSR. Later that year, Sputnik II carried a dog named Laika into orbit.
- **1959** – The USSR's Luna 2 became the first human-made object to reach the surface of the moon.
- **1961** – The USSR's Venera 1 became the first probe to flyby Venus, being the first to reach another planet.
- **1962** – Yuri Gagarin became the first human in space onboard the USSR's Vostok spacecraft.
- **1969** – The American Apollo 11, powered by Saturn V rockets, successfully landed the first humans on the moon, Neil Armstrong and Buzz Aldrin.
- **2013** – Voyager 1, launched in 1977 by the USA, becomes the first human-made object to leave the solar system.

Nowadays, several nations like Europeans countries (under ESA), India, Japan, China, Brazil, among many others, have their own space programs, for which rockets, and their development, are crucial. Even more recently, the space industry stopped being a centralized state research to become also a private business, as recent Space X, Blue Origin and Virgin Galactic launches [6] prove.

2.2 Rocket's Characterization

Air vehicle's propulsion systems can be subdivided into air-breathing or non-air-breathing. Rockets carry both the fuel and the oxidizer, being placed in the second category. Rockets' biggest advantages are the possibility of operating regardless of the atmospheric composition, with no altitude ceiling, and the biggest thrust to engine weight. Yet, in some applications, such as missiles, a dual-mode engine is used which combines an air-breathing (such as ramjet, turbojet, or turbofan engines) and a rocket mode.

Rockets can be classified into chemical and nonchemical in its process to generate energy to be converted in thrust. The most common chemical rockets can have a liquid, solid, or hybrid propellant. As for the nonchemical ones, there are many concepts and actual deployments like electrical, thermal, solar and nuclear.

In general, the major components of a chemical rocket include containers for propellant, a combustion chamber, an exhaust nozzle, an igniter, navigation equipment, and a payload.

Figure 2.1 shows a solid chemical rocket, where both the fuel and oxidizer are contained in a casing that surrounds the combustion chamber. The casing contains all the ingredients necessary to sustain the combustion process and is burnt away during the production of thrust.

As for Figure 2.2, it displays a simplified configuration of a liquid chemical rocket, in which the fuel and oxidizer are stored separately and pumped at high pressure to the combustion chamber [5].

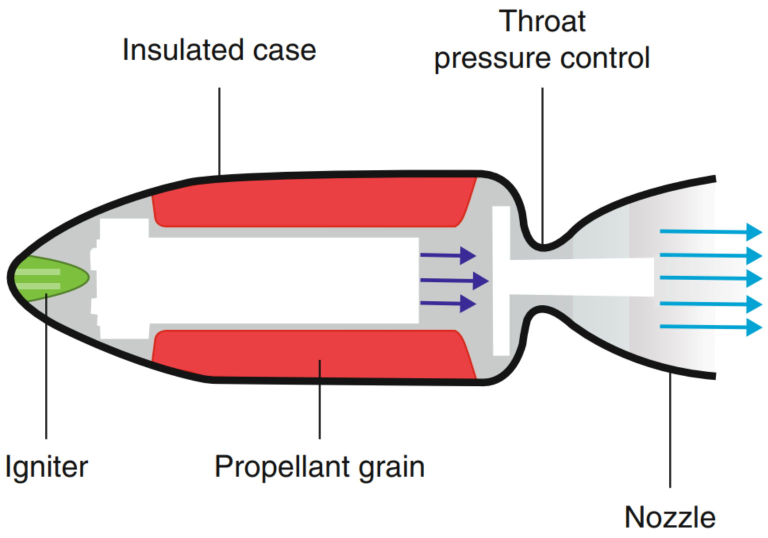

Figure 2.1: Simplified drawn of a solid-propellant rocket [5]

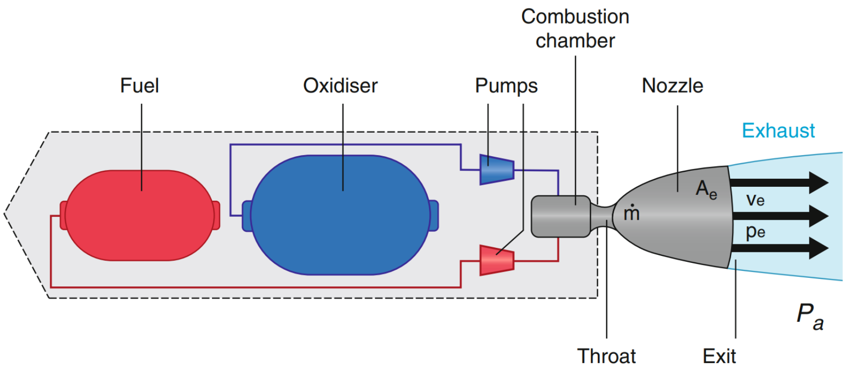

Figure 2.2: Simplified drawn of a liquid-propellant rocket [5]

For chemical rockets, the nozzle and its efficiency are crucial, as this component is the one responsible for converting the internal energy of the combustion gases into thrust. This process is explained in Subsection 2.3.1.

2.3 Conventional Rocket Nozzles

2.3.1 Thrust Production

Thrust is generated in most aerial vehicles by ejecting mass, utilizing Newton's third law. This can be calculated using Equation 2.1. In addition to the mass ejection, a second force is generated by the pressure difference between the flow at the exit and the ambient pressure, which also contributes to the overall thrust produced by the vehicle's engine [5].

$$F = \dot{m}u_e + (P_e - P_{amb})A_e \quad (2.1)$$

From Equation 2.1 and given the high exhaust flow from a chemical rocket engine, the rocket's thrust is predominantly given by the momentum that the exhaust gases, products of the combustion, provide when accelerated through the nozzle [7].

Nozzles where invented as means to change the properties of a flow such as velocity and pressure. The de Laval nozzle, containing a convergent followed by a divergent section, many times referred as convergent-divergent nozzle, does so in such a way that a supersonic flow can be obtain at the exit. Rockets integrate a de Laval nozzle with a combustion chamber. The flow behavior off such nozzle is observed in Figure 2.3 [8].

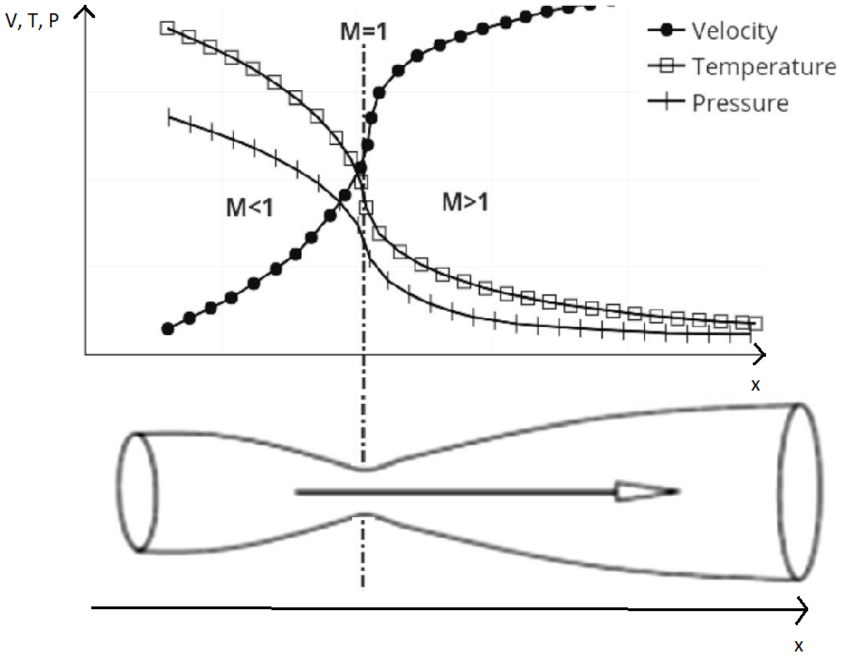

Figure 2.3: Velocity, Temperature and Pressure variation in a de Laval Nozzle [8]

A de Laval nozzle can be divided into three sections: the convergent (subsonic), the throat (sonic) and the divergent (supersonic). Each regions has different flow behavior, having different analysis methods to determinate its contribution for the production of thrust. Nonetheless, all regions have their performance greatly impacted by the conditions in the combustion chamber.

The convergent section accepts the exhaust gases from the combustion chamber, at almost static conditions, providing the first mean of acceleration until a sonic value. So, the convergent affects the mass flow and, at some degree, the efficiency of the combustion chamber.

At the throat, the flow reaches a sonic velocity, being choked, meaning it can not be accelerated further without area increases. Having a fixed area and Mach Number (MN), it's the throat, aligned with the conditions provided by the combustion chamber, that limits the mass flow through the nozzle, having a great impact on the thrust produced according to Equation 2.1.

At Equation 2.1, thrust is also greatly impacted by the exit velocity. Since the flow is choked at the throat, is in the divergent section that it accelerates further to supersonic values. Here, the comprehensible flow gains kinetic energy as a trade off by losing internal energy (as seen in Figure 2.3 by the decrease in temperature), with a pressure drop. The exit velocity is dependent on the ratio between exit and throat areas, outside conditions in relation to the chamber and the divergent section design.

So, the divergent section of the nozzle has been the major concern of nozzle's design, as it is the major topic of the present dissertation.

There are several numerical methods available for designing the divergent section of the nozzle. However, each method involves certain simplifications, which come with their respective limitations.

Although this dissertation mainly focuses on the fluid dynamics aspect of the design process, other factors are relevant, such as fabrication methods, cooling requirements, and the weight of the rocket [7].

Three major concepts are necessary to evaluate a nozzle's performance. The first concept, represented by Equation 2.2, is the specific impulse, which measures the thrust produced by the weight flow rate of propellant burned. It is important to understand the rocket's nozzle efficiency.

$$I_{sp} = \frac{F}{\dot{m} g_0} \quad (2.2)$$

The second concept, represented by Equation 2.3, is the total impulse, which measures the thrust produced over the entire duration of the engine's operation.

$$I_t = \int_0^t F dt \quad (2.3)$$

Finally, the thrust coefficient, exhibited in Equation 2.4, represents the dimensionless value of thrust obtained by dividing it by the chamber pressure and the throat area. This is a fair indicator of nozzle efficiency since, in theory, the thrust value depends solely on the pressure ratio between the chamber and the ambient, and the area ratio between the exit plane and the throat [9].

$$C_F = \frac{F}{p_1 A_t} \quad (2.4)$$

Parting from the concept of the ideal nozzle in Subsection 2.3.2, the two most used nozzle designs, the conical and bell nozzles, in Subsections 2.3.3 and 2.3.4, respectively, were developed and allowed almost all the advances in space exploration using chemical rockets.

2.3.2 Ideal Nozzle

The ideal nozzle is a concept that provides the best performance, which all nozzle designs try to match. A parallel flow and exit pressure matching external pressure are some consequences from this simplification [8].

Looking into more detail, the ideal nozzle involves the following considerations [9]:

1. The exhaust gases are in chemical equilibrium, with a homogeneous composition and in a gaseous state.
2. The exhaust gases obey the perfect gases law.
3. The flow is adiabatic, meaning there are no appreciable heat transfers to the wall.
4. The flow is isentropic, without discontinuities in properties and/or shock waves.
5. The boundary layer effects are neglected, with no significant wall friction.
6. The flow rate is constant and steady, without gas pulsations, turbulence, and with the transient effects of starting-up and shutting down neglected since they are of short duration.
7. The exit flow is parallel and unidimensional.
8. The flow's velocity, pressure, temperature, and density are uniform across any nozzle's normal section.
9. Before the combustion process, propellants are store at ambient temperature, expect for cryogenics which are at their boiling point.

Nonetheless, this are fair simplifications due to how fast the expansion occurs. For chemical rockets, tested efficiency parameters are usually just 1%-6% below these calculated ideal values[9].

2.3.3 Conical Nozzle

As shown in Figure 2.4, a conical nozzle is one of the simplest types of divergent nozzle contours. It is characterized by the throat diameter, exit diameter, and divergence angle α. Due to its practical manufacturing process, has historically been one of the most used contours [8].

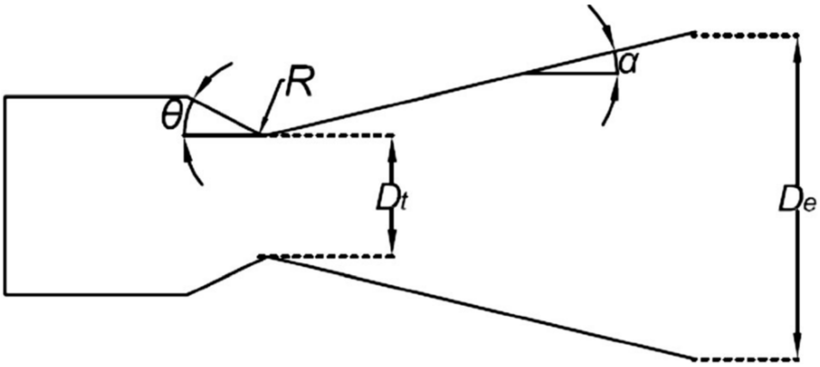

Figure 2.4: Conical nozzle's configuration [8]

The bigger the divergence angle, the shorter the nozzle will be, as this is the design desire, since length is a fair indicator of a nozzle's weight [10].

In theory, the flow velocity at the exit could be considered one-dimensional, covering all the exit's area, but due to the wall having an angle right before the exit, not all velocity vectors are parallel to the rocket, creating side loads and reducing the effective thrust [8].

This type of nozzle is very susceptible to flow separation and overexpansion at lower altitudes and the thrust losses increase with the decrease of nozzle length by manipulation of the divergence angle. Taking into account nozzle's length, performance and weight, a divergence angle of 15^{o} offers the best compromise.

Nonetheless, when a low area ration is desired, and fabrication simplicity is privileged in deterioration of aerodynamic performance, which are design parameters for some missiles, there's no need for more complex designs and conical nozzles offer a good tradeoff [11].

2.3.4 Bell Nozzle

As the divergence angle of a conical nozzle is increased, the flow divergence at the exit can increase significantly. To minimize this effect, more complex nozzle designs are necessary. For example, the bell nozzle is a more complex design that can provide a better performance.

Figure 2.5 shows a comparison between an equivalent conical nozzle and two bell nozzles with different lengths and contour angles. The bell nozzles are shorter, with lengths of 80% and 60% of the length of the conical nozzle, and have smaller contour angles at the exit, with values of 11° and 8.5° compared to the 15° of the conical nozzle. These design changes help to maintain a more axial flow at the exit, reducing the degree of divergence and improving the overall performance of the nozzle.

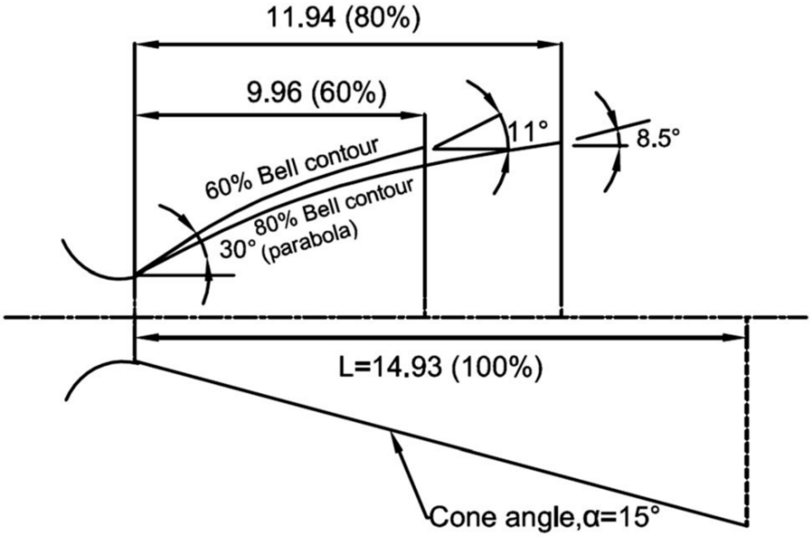

Figure 2.5: Bell nozzle's configuration and comparison with conical nozzle [8]

The gradual reverse of the divergence angle through the nozzle is possible by a 20°-50° divergence right after the nozzle, which does not introduce significant losses since the huge favorable pressure gradient permits this rapid expansion without separation.

This makes the bell nozzle the most widely used nozzle design in modern rocketry and from which most advanced designs in Section 2.4 are derived, as it already shows good performance and reliability results [8].

2.3.5 Real Nozzle

The level of precision required for rocket systems demands more accurate algorithms that involve a better understanding of energy losses, heat transfer and other physical or chemical phenomena.

In real nozzles, not all the chemical energy contained in the propellant is available as thermal energy, and not all the thermal energy can be converted into kinetic energy. Therefore, the performance of a rocket nozzle is affected by several factors that can cause losses in thrust and specific impulse.

The first factor, already stated before as a concern mostly of the conical nozzle, is the divergency losses resulting from a non-unidimensional flow profile at the exit plane. Another factor is that small chamber areas relative to the throat, lead to pressure losses in the chamber and a reduction of the exhaust exit velocity and thrust produced.

Boundary layer effects can also be significant, particularly for smaller nozzles with low area ratios, making a portion of the flow, ranging from 2% to 25%, subsonic. Due to the no-slip condition, the flow next to the wall has zero-speed and possesses high thermal energy that is dissipated to the wall and the nearby moving flow. The immediate flow is laminar and subsonic, devolving further from the wall into supersonic zones where turbulence can occur, before it joins the free stream.

Combustion in the rocket nozzle is typically unsteady, resulting in flow oscillations and lower chamber pressure during transient operations. Chemical reactions in the flow can cause losses of up to 0.5%, and incomplete mixing of the gas composition means that the gas constants are not uniform throughout the nozzle.

Small solid particles and liquid droplets also exist in the flow, which need to be accelerated, with little thermal energy contribution. If they are larger than 0.015mm and equivalent to more than 6% of the flow's mass, specific impulse losses can rise to 10%-20%. Although less significant, in high area ratio nozzles, aggressive expansion can lead to the precipitation of some exhaust constituents.

It still must be mentioned that uncooled materials suffer erosion, which is relevant for the throat since if its area increases, some chamber pressure is lost and also the area ratio decreased. Up to 0.7% of specific impulse can be lost.

And, at last, operating away from the design altitude reduces thrust and specific impulse for nozzles with fixed area ratio [9].

2.3.6 Altitude Limitations of Real Bell Nozzles

Figure 2.6 summarises the losses referred in Subsection 2.3.5 for a bell nozzle. Among them, the most significant for H_2-O_2 rockets, like viscous flow separation and uneven flow at the exit, are related with overexpansion and underexpansion.

The conventional nozzles used on current rockets, restrict the overall performance during the ascent of the vehicle due to their fixed geometry.

At low altitudes, the ambient pressure is higher than the nozzle's exit pressure causing a flow overexpansion. Oblique shocks radiate from the exit of the nozzle in order to rise the flow's pressure to match the ambient pressure.

In contrast, at high altitudes, the ambient pressure is inferior to the nozzle exit pressure,

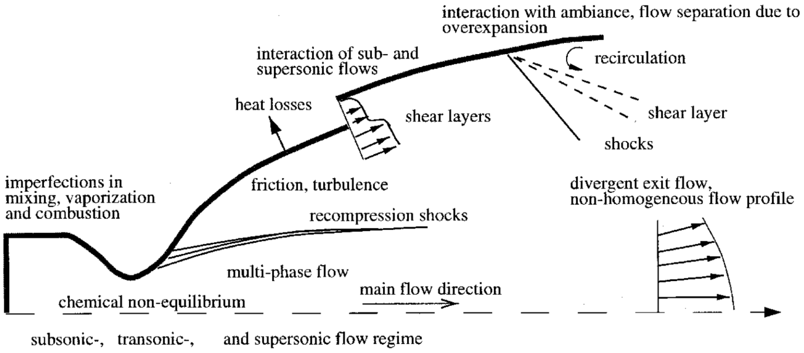

Figure 2.6: Losses in a real bell nozzle [2]

resulting in a flow underexpansion. After leaving the nozzle, the flow will suffer further expansion, so it equals the environmental pressure.

The referred phenomena cause nozzle performance losses compared to on-design testing and are explain with more theoretically detail in Section 3.3.

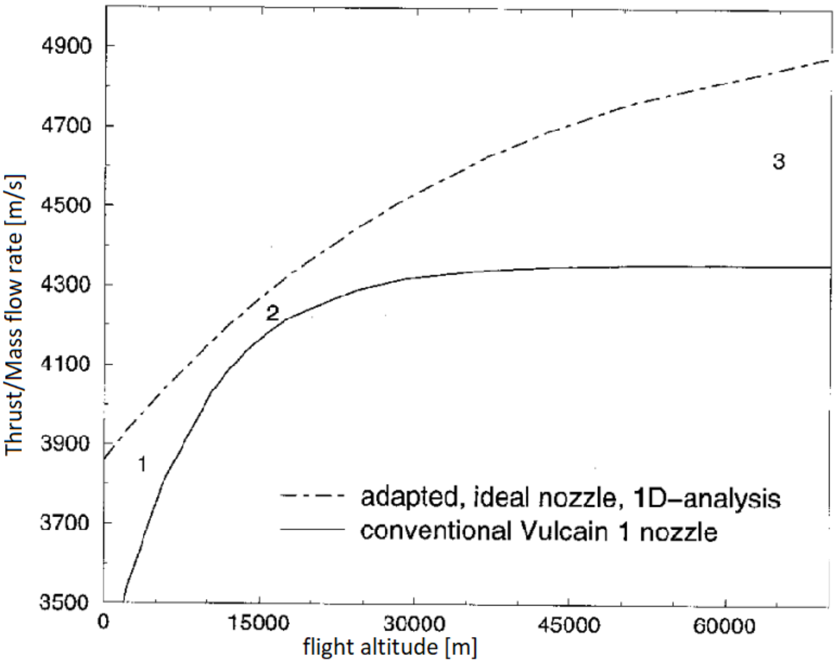

Figure 2.7: Vulcain 1 engine's nozzle specific impulse in function of altitude compared with ideal nozzle [2]

Figure 2.7 compares the specific impulse of the Vulcan 1 rocket engine, equipped with a conventional nozzle, to the ideal altitude adaptive nozzle. The Vulcan 1 is designed to be optimal at an ambient pressure of 0.18 bar, felt at a terrestrial altitude of 15km.

The overall losses ascend to 15% of performance. Looking at Figure 2.7, one could say the nozzle should be projected to achieve better vacuum performance, but, the higher area ratio would induct the separation of the flow inside the nozzle during low altitude operation, resulting in undesired side-loads [2].

2.4 Advanced Rocket Nozzles Designs

In this section, some different nozzle concepts upgrading the performance of conventional nozzles are presented. By being altitude adapting, these new concepts minimize the losses caused by overexpansion and underexpansion. It must be taken into consideration that conventional bell rocket nozzles are already very efficient in terms of internal losses effects like friction and non-uniformity.

2.4.1 Dual-Bell Nozzle

As illustrated on Figure 2.8, a dual-bell nozzle consists of a regular bell nozzle with an external extension. This promotes a net performance improvement just by the effects of the wall inflection.

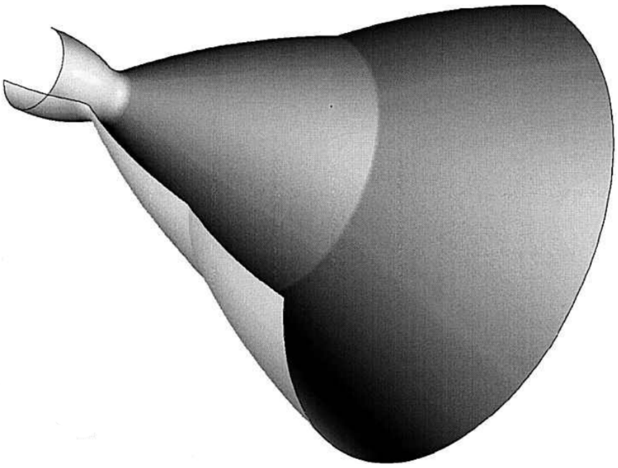

Figure 2.8: Dual-bell nozzle sketch [2]

Figure 2.9a) shows that at lower altitudes, the wall inflection boosts a controlled and symmetrical flow separation, reducing the effective area ratio.

For higher altitudes, as seen on Figure 2.9b), the flow stays attached to the wall all the way until the extension exit, utilizing the full geometrical area, with a high-quality vacuum performance.

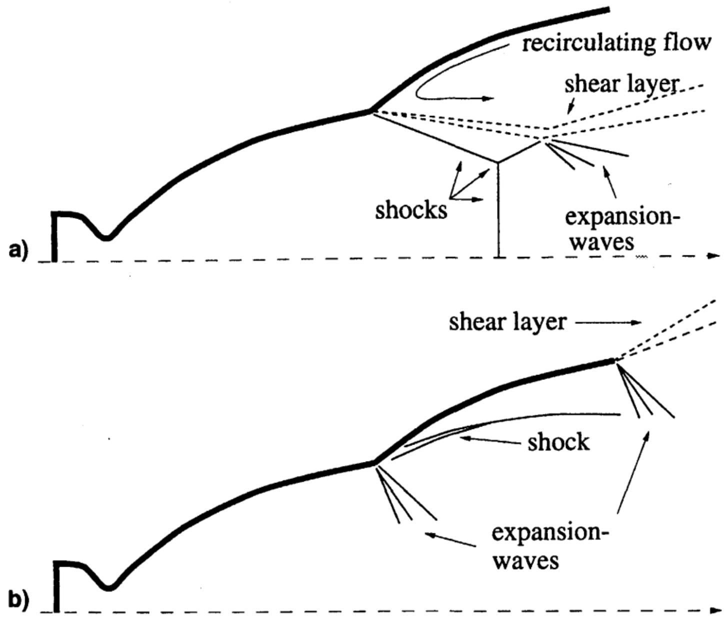

Figure 2.9: Flow phenomena inside a dual-bell nozzle: a) overexpanded with flow separation and b) underexpanded with fully attached flow [12]

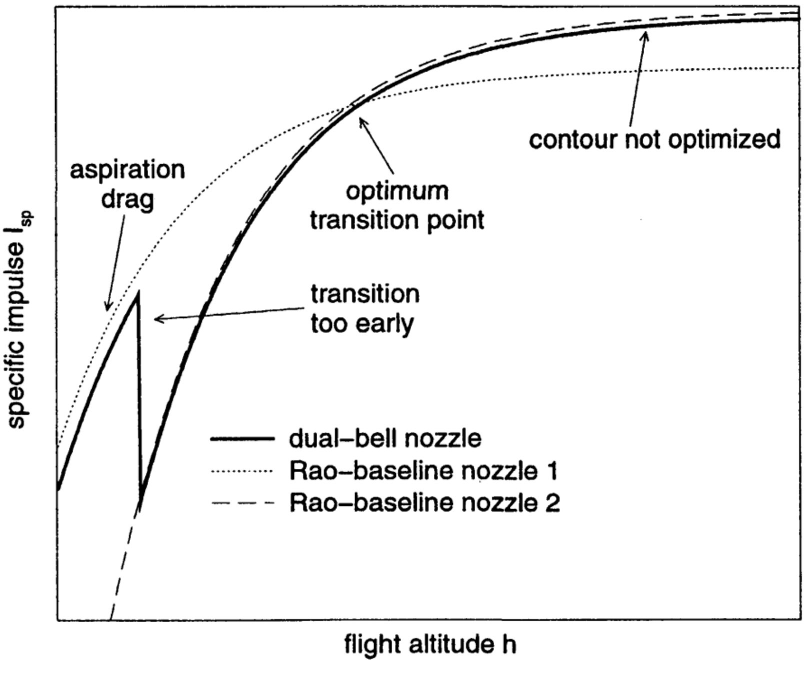

Figure 2.10: Dual-bell nozzle specific impulse in function of altitude compared with ideal nozzle, nozzle 1 (same area ratio as the dual-bell nozzle first segment) and nozzle 2 (same area ratio as the dual-bell nozzle including the extension) [12]

Some losses occur at some altitudes, in comparison with conventional single bell nozzles, as observed in Figure 2.10. For lower altitudes, aspiration drag, caused by a slight adverse pressure gradient at the exit, reduces the produced thrust in relation to nozzle 1 . Further losses result from the fact the flow adheres to the extension wall before the optimum transition point.

Even at higher altitudes, there's still thrust degradation in comparison to nozzle 2, due to the imperfect nozzle's counter. Still, during the rocket's ascension, the dual-bell nozzle provides a impulse net gain compared to the nozzle 1 or 2 alone, and all without any movable parts, providing good reliability [12].

2.4.2 Nozzles with Fixed Inserts

This type of bell achieves a similar behaviour and performance curve as the dual-bell nozzle by inserting a trip ring inside a conventional bell nozzle, responsible for causing the flow separation at low altitudes.

According to some literature [13], this ring can be as small as 10% of the local boundary-layer thickness in order to reduce the losses at vacuum performance.

The transition point between the sea level and vacuum operation depends on the wall pressure near the trip ring and the disturbance provoked by it, creating significant uncertainties. Although this is a simple and with low technology risk concept, the referred uncertainties led to the rejection of this concept [2].

2.4.3 Nozzles with Temporary Inserts

The presence of an insert within the nozzle negatively impacts vacuum performance. If the insert is removed before high altitudes are reached, the high performance of the baseline nozzle can be matched.

A modified RD-0120 engine with a secondary nozzle insert was previously hot-fire tested, resulting in a 12% performance gain at sea level, with the only losses compared to the ideal nozzle being caused by aspiration drag.

The challenge with this design is the ejection of the insert, which can lead to undesired side loads, shocks, and collisions near the exit plane. Although ablative inserts have been considered, the stability of the surface and the regression rate are still difficult to model with current technology [14].

2.4.4 Nozzles with Active Secondary Gas Injection

This concept proposes that a second gas flow can be injected inside the nozzle, normal to the wall, in order to force flow separation during sea level operation, reducing the nozzle's area ratio.

The injection is originated by a high-pressure reservoir, but the amount of fluid needed to induce flow separation is considerable, without expected net impulse gains [2].

2.4.5 Nozzles with Passive Secondary Gas Injection

Similar to the previous concept, but the injection is achieved by creating “slots” to let the ambient air enter the nozzle. The ”slots” are closed at high altitudes.

Unfortunately, this passive mechanism only works at lower altitudes, where the ambient pressure is high enough to enter the nozzle. This operational envelop is further shorted due to the stream around the rocket, that reduces the pressure at its end, near the engine’s nozzle [2].

2.4.6 Extendable Nozzles

This concept, seen in Figure 2.11 involves a truncated low area ratio nozzle that is used in sea-level conditions. It has an outer extendable component that attaches at higher altitudes, thereby increasing the area ratio. The nozzle can be design using the Method of Characteristics, for example, showing an improved performance.

However, the in-flight placement of the extendable component requires the use of mechanical devices, which increases the nozzle’s weight and reduces its reliability, posing engineering challenges for the cooling system. Some upper stages of rockets already use a similar concept to reduce packaging volume.

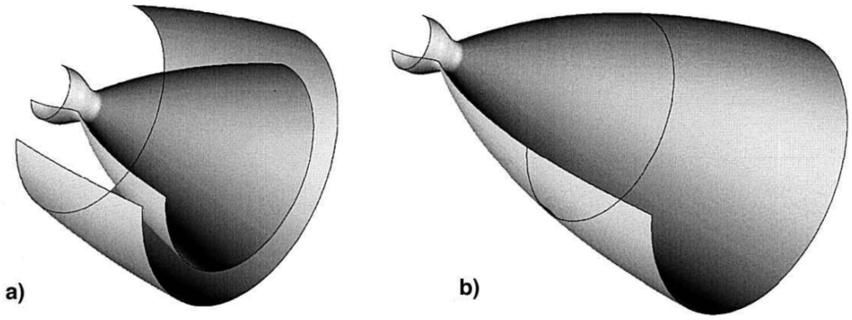

Figure 2.11: Extendable nozzle sketch at: a) sea-level and b) vacuum operations [2]

2.4.7 Plug Nozzles

Sometimes referred as an “inside out bell nozzle”, the outside gases are not contained by an outer boundary, being able to expand accordingly with the atmospheric pressure, staying the flow mostly axial [3]. The linear aerospike is a particular type of a plug nozzle, and being the subject of study of this dissertation, plug nozzles are further explained in Section 2.5.

2.4.8 E–D Nozzle

E-D stands for expansion-deflection and refers to a type of nozzle that has a central pintle directing the flow towards the nozzle's wall. It operates in an altitude-adaptive manner similar to that of plug nozzles, with the difference being that the expansion is controlled from within the nozzle.

Figure 2.12 illustrates the flow inside an E-D nozzle, where a system of compression and decompression waves direct and adapt the exit pressure of the flow. An open wake at the center of the exit flow creates aspiration drag, reducing the pressure in the wake to which the flow pressure will equal, leading to overexpansion.

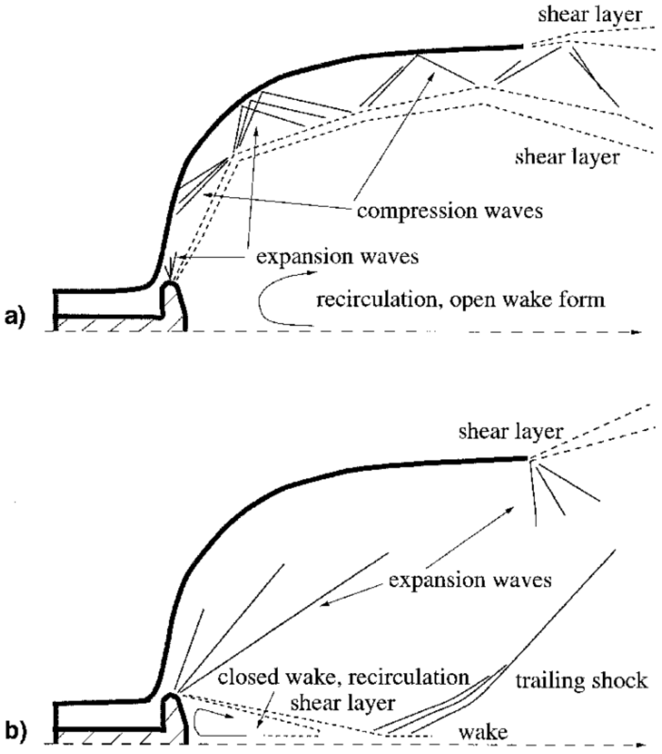

Figure 2.12: Flow phenomena inside an E-D nozzle at: a) sea-level operation (open wake) and b) vacuum operation (close wake) [2]

As the outside pressure drops, there's an increase in the area ratio, closing the wake. But the losses incurred from overexpansion, negatively impact the altitude adaptation of E-D nozzles, making them only more efficient if compared to high area ratio with a desired short length bell nozzles. Another challenge with this concept is the high heat fluxes in the throat and pintle [2].

2.4.9 Nozzles with Throat Area Varied by a Mechanical Pintle

The mechanical pintle, used to control thrust in some solid propellant rockets equipped with bell nozzles, is a proposed method to achieve altitude adaptiveness, for this and other types of propellant. The pintle works by adjusting the throat area, which in turn would alter the nozzle's area ratio.

However, the implementation of such a mechanism requires a complex and heavy actuator and cooling system, leading to increased weight and decreased reliability [2].

2.4.10 Dual-Throat Nozzle

The concept of the dual-throat nozzle involves two conventional combustion chambers, one concentric to the other, with both converging to the same fixed exit area, as depicted in Figure 2.13. The original purpose of the dual-throat nozzle was to regulate thrust, but it can also be altitude-adaptive.

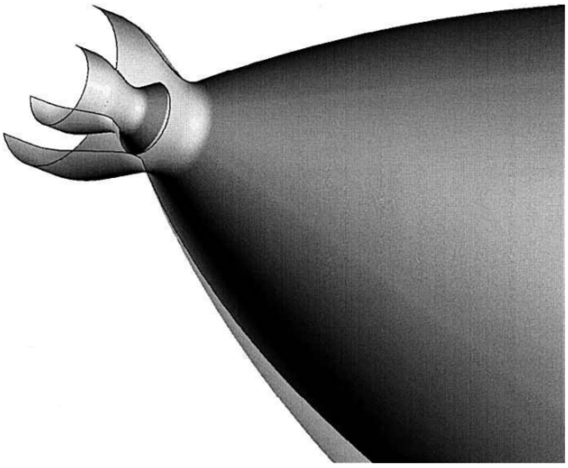

Figure 2.13: Dual-throat nozzle sketch [2]

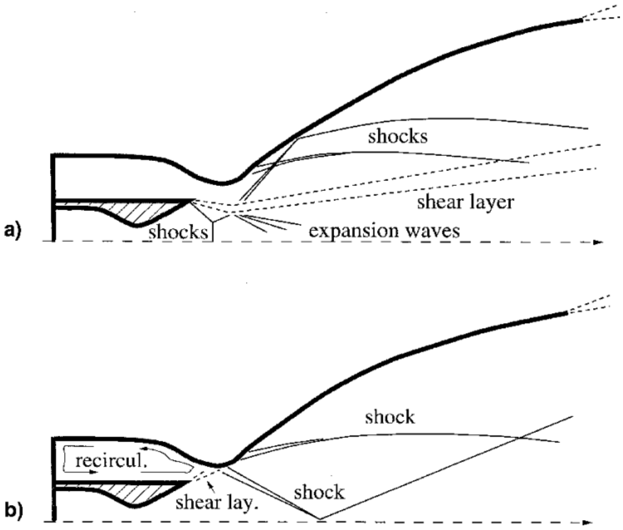

Figure 2.14: Flow phenomena inside a dual-throat nozzle at: a) sea-level and b) vacuum operations [2]

At low altitudes, both combustion chambers are active, resulting in a larger throat area and a lower area ratio, thereby preventing overexpansion. At a certain altitude, the outer chamber is shut off, reducing the throat area, increasing the area ratio, and allowing the flow to fully expand.

Both behaviors can be seen in Figure 2.14. Still, there are some losses in vacuum operation due to the discontinuity caused by the outer chamber and the resulting recirculation [2].

2.4.11 Dual-Expander Nozzles

Similar to the dual-throat nozzle concept, the dual-expander nozzle has the same geometry and altitude compensation behavior, with the difference that the inner chamber has a short divergent section and is the one that is shut down during vacuum operation.

Both behaviors can be seen in Figure 2.15. It is important to highlight the rapid expansion and subsequent recompression in Figure 2.15b), as it creates a recirculation zone. This issue can be addressed by bleeding air into the inner chamber, though there will be a small reduction in impulse due to the increased area ratio.

The major engineering challenges associated with this design include the potential structural disintegration of the inner chamber during vacuum operation due to high heat fluxes and pressure oscillations [2].

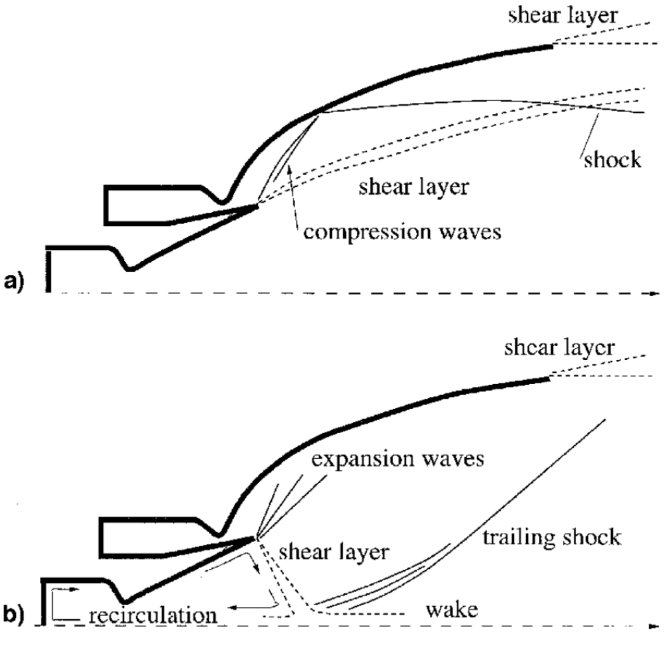

Figure 2.15: Flow phenomena inside a dual-expander nozzle at: a) sea-level and b) vacuum operations [2]

2.4.12 Multi Nozzle Grids (MNG)

With a transversal sketch depicted in Figure 2.16, where each triangle represents a ”nozzlettes”, MNG have been studied in recent years, not necessarily for their altitude adaptive behavior, but also for their potential to improve overall performance.

The way a MNG increases the expansion ratio is by adding more ”nozzlettes” rather than increasing the length, which adds little weight and has been shown to improve performance when designed with multidisciplinary methods.

Anyhow, the small throat area of each ”nozzlettes” leads to high ablative erosion, specially to the throat, which will drastically decrease performance over time [15].

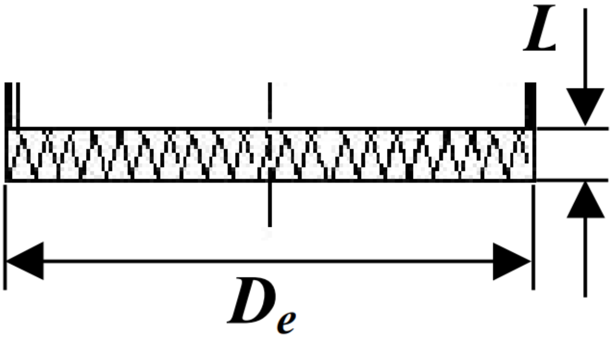

Figure 2.16: MNG sketch [15]

2.4.13 Most Promising Concepts that are Currently Under Investigation

Most of the previously referred concepts, despite their promising potential, were ultimately discarded due to technological limitations and the relatively minor advantages their usage could bring. By the end of the 20^{th} century, only a few of these concepts had survived and continued to be studied, by Academics and the Space Industry, through computer simulations and prototype testing.

The dual-bell nozzle is a concept that holds great promise due to its simple design. However, two major obstacles prevent its practical application: the early transition between the two modes and the resulting undesirable side loads caused by the asymmetric displacement of the separation line during the transition. Solutions to this issue have been proposed, such as fluidic control, in which slots near the inflection point add fluid stored in a dedicated tank, allowing the separation line to move symmetrically from the inflection point to the exit plane during the transition. For a launcher like Ariane-5, the net impulse gains from this concept could result in the ability to carry an additional 1.5 tons of payload to a reference geosynchronous transfer orbit [16].

E-D nozzles are also still under investigation, particularly because of their nearly optimal behavior at vacuum operation, characterized by a relatively small area ratio, as demonstrated through cold testing by the University of Bristol [17]. The central pintle is a critical aspect of E-D nozzles, as it significantly influences their performance by defining the transition point and its process. Some experimental results that show some pintle geometries with a smooth transition from open to closed wake can be implemented, leading to improved performance and the best thrust coefficient [18].

More recently, an expansion-deflection dual-bell nozzle has gained attention, consisting of a shorter dual-bell nozzle with a central throat pintle. At sea level, compared to a traditional dual-bell nozzle, it may experience some thrust losses due to the open wake causing recirculation. However, it compensates for this with improved average specific impulse because of a later transition and a slightly lighter structure due to the shorter nozzle [19].

Finally, plug nozzles, particularly aerospikes, have seen significant advancements, with numerous prototypes tested and various solutions proposed to address their engineering challenges. As the focus of the present dissertation, aerospikes will be discussed in greater detail in Section 2.5.

2.5 Aerospike Nozzle

2.5.1 Characterization

An aerospike nozzle is a type of plug nozzle, where the center-body, or plug, assumes the shape of a ”spike” . The term ”aerospike” actually refers to the existence of a truncation, where the solid spike is replaced by one that is aerodynamically fashioned [20].

The aerospike nozzle does not have any moving parts and obtains its altitude adaptive properties by lacking a rigid outer boundary, unlike conventional nozzles [3]. This allows it to adjust to the ambient pressure and meet the necessary pressure requirements without any constraints.

The nozzle’s mass is reduced by having a truncated spike, which also helps to avoid some extreme heat fluxes. However, this comes at the cost of the loss of some thrust delivery [2], as explained in Subsection 2.5.2.

During Lockheed Martin X-33 space shuttle development, an aerospike engine (Rocketdyne XRS-2200) was tested onboard a SR-71, with promising results. Eventually this aircraft program was abandoned in 2001 [20]. Since then, some cold and hot tests have been performed, basing most sources of comparison for numerical experiments.

2.5.2 Behavior

First, it must be noted that the exhaust gases are not expanded against a bounding wall, as in a conventional nozzle, so besides Equation 2.1, another term must be added so the force that the gases exert on the spike can be considered, being given by Equation 2.5. For truncated spikes, the base area also contributes for thrust as seen in Equation 2.6 [21].

$$F_{spike} = \int A_{spike}(p_{spike} - p_{atm})dA \quad (2.5)$$

$$F_{base} = (p_{base} - p_{atm})A_{base} \quad (2.6)$$

At low altitudes, as shown in Figure 2.17a), the high ambient pressure causes the exhaust flow to remain close to the nozzle's wall and be directed to the axial position through a series of expansion-compression fans. The flow is pressed against the wall to the extent that an open wake at ambient pressure is formed. Without truncation, shocks can occur, resulting in flow separation and reattachment, which will lead to undesired side loads.

At higher altitudes, as seen in 2.17c), the free boundary promotes the appearance of recompression shocks that enable the exhaust flow to remain primarily axial, even in a wider plume. The flow does not expand past the nozzle like in other underexpanded nozzles, thus contributing to thrust production.

At the design altitude, seen of Figure 2.17b), the wake is already closed, but the major difference from the underexpanded scenario is the plume is less wider, with a more axial flow, promoting a slightly higher thrust.

A secondary gas flow can be introduced into the truncated area to minimize losses arising from the transition from open to close wake [3].

The truncation of the spike also enhances the rocket's overall performance by reducing the weight of the nozzle. Nevertheless, it should be noted that the transition between open and closed wake occurs at lower altitudes as the truncation increases. Also, as the truncation is increased, and the base area augments, the advert pressure gradient at the open wake base has its effects amplified according to Equation 2.6.

At pressure ratios lower than the design point, the recirculation promotes a pressure lower than the ambient pressure, resulting in reduced thrust production. However, above the design point, the recirculation zone has a higher pressure than the environment, which positively contributes to thrust production. Therefore, the magnitude of the truncation must be carefully studied to optimize overall performance [2].

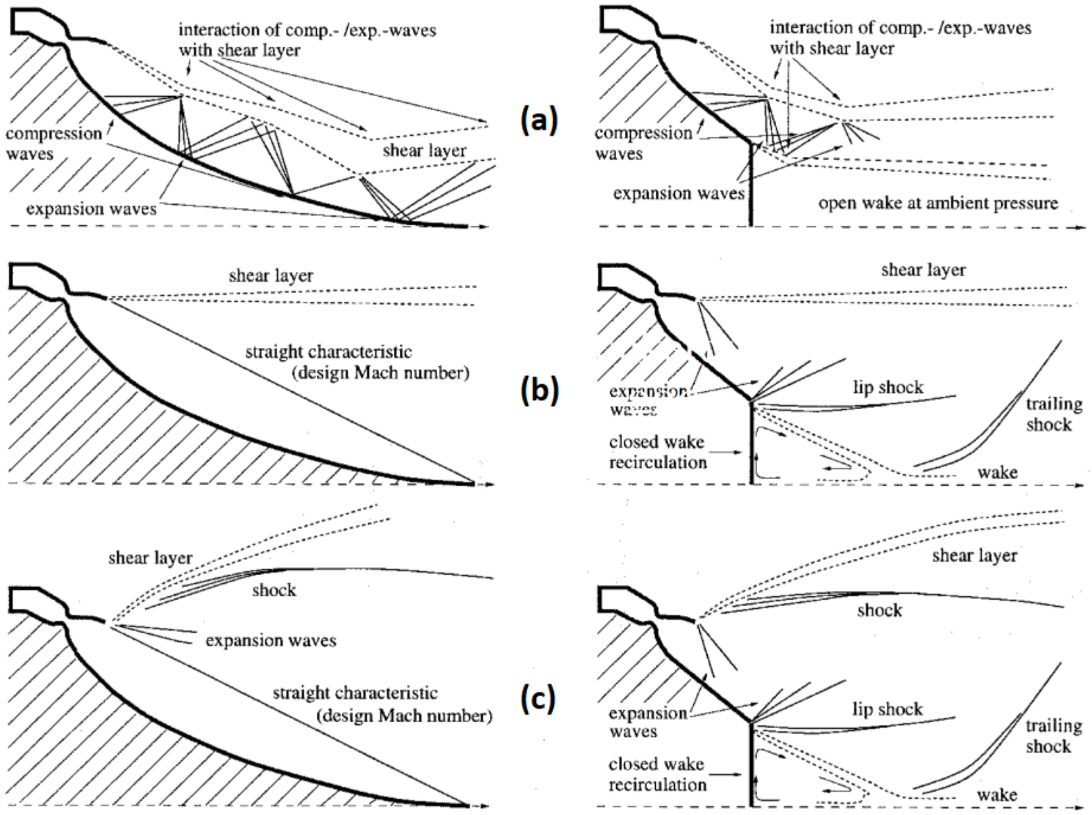

Figure 2.17: Flow phenomena at an aerospike nozzle at: a) sea-level or low PR b) design altitude/PR and c) vacuum or high PR operations [2]

2.5.3 Advantage and Disadvantages

In this subsection the disadvantages and advantages of aerospike nozzles are summarized and briefly explained.

Table 2.1: Aerospike disadvantages

Disadvantage	Project Field	Explanation	Possible Solution
Extreme flow condition (T=3000k) causing erosion	Materials	The truncation experiences high temperature, pressure, and heat fluxes, and its small volume makes it difficult to implement regenerative cooling and other solutions [22].	The usage of 90% H_2O_2 fuel leads to a decrease in the temperature of the exhaust gases to arround 1023K, which can be easily withstood by stell alloys [22].
Considerable weight (full spike)	Structure	The solid spike is typically made of heavy metal elements with complex coatings that can withstand the extreme conditions of the expanding flow [23].	Truncated nozzles can be made shorter, by truncation, but there is a tradeoff between weight and average impulse [23].
Base Pressure	Performance	Closing the wake before the design point results in a lower base pressure than the ambient pressure, which reduces thrust, as explained previously.	A secondary flow, prevenient from the gas-generator-cycle that powers the tanks pumps can be added at the base, increasing the local pressure and, therefore, the thrust produced [24].
Clustering flow interaction	Performance	When the flow from each module expands and interacts, it creates additional shocks, which decreases the produced thrust [25].	No solution was found but the performance losses are small and does not mean bell nozzles are more efficient [25].
Manufacturing challenges for throat and chamber	Materials, Manufacturing	The small area of the throat, coupled with the extreme heat flow, makes it difficult to assure continuous optimal performance [17]. Also, in most designs, the spike needs to be fixed inside the combustion chamber [2].	Additive manufacturing techniques can produce alloys and other advanced materials that are capable of withstanding the harsh environment arround the nozzle, while maintaining the desired dimensional accuracy [26].

Table 2.2: Aerospike advantages

Advantage	Project Field	Explanation	Improvement
Vector Thrust	Dynamic Control	Due to clustering of at least four different throats, it is possible to induce pitch, yawn and roll (just for linear) moments. More complex methods, such as flapping, are necessary to induce roll moments in toroidal aerospikes [27].	Eliminates the need for a gimbal or other movable piece, reducing the weight of the engine [28].
More Average Impulse	Performance	At low altitude, the aerospike behaves almost like the ideal nozzle, compensating more substantial losses felt at higher altitudes [23].	This proves aerospike engines are suitable and advantageous for low altitude operation and also for SSTO vehicles [23].
Less drag	Aerodynamics	The base of the rocket produces drag. In an aerospike, almost all this area is used to produce thrust instead [23].	Less exposed area implies less drag. Since all the base can be used to produce thrust, at vacuum operation, area ratios of up to 1:150 can be obtained [23].
Large source load	Structures	The thrust produced by the nozzle is transferred to the rocket as a distributed load and not as a point source load [23].	The distributed load allows a more efficient and lighter rocket's structure [23].
CubeSat application	Performance, Structure	Aerospikes can be design for vacuum operation, being easily scaled and integrated in CubeSat designs [29]. They will be much shorter than a Bell nozzle with the same area ratio [30].	Vector thrust, high area ratio, and low weight make a good trade-off for using aerospike engines in satellites with a low form factor [29].
Better Packing	Logistics, Structure	For high expansion ratios, it has a much shorter length and volume compared with an equivalent bell nozzle [30].	When multiple staging cannot be avoided, aerospikes are much easier to transport to high altitudes [30].
Improved Reliability	Safety	Clustering allows the several modules to operate independently. In case of a malfunctioning module, it can be shut down as so an 180° opposing one [30].	This way, the mission is not jeopardized, keeping the thrust vectoring with just the loss of some thrust [30].
Practical Landing	Dynamic Control, Structure	Clustering allows the several modules to operate independently. During landing, a reduction in thrust can be obtained by sequentially shutting down pairs of modules or reducing the flow in some [30].	This allows a more reliable landing method with only the need to develop controlling valvules. There's a reduction in "legs" weight as they can be shorter due to the shorter nozzle [30].

2.5.4 Overall Balance

Both toroidal and linear aerospike nozzles provide relatively efficient pressure adaptation, with almost ideal behavior below the design altitude. Still, their behavior above the design point is still non-optimal and even performs worse in terms of thrust due to clustering and truncation, compared with bell nozzle designs for higher area ratios [2].

When a wider analysis is performed, at vacuum operation, aerospikes provide a much lighter, shorter and easier to integrate nozzle compared with long bell nozzles. The thrust loss is compensated by providing an improved specific impulse [29].

Rocket engines with aerospike nozzles are significantly more efficient, improving not only the aerodynamic behavior of the exhaust flow but also enhancing the rocket in several key aspects, such as structure, stability, and control. However, according to the literature, there are still some engineering problems to be overcome. Recent developments in research fields such as materials science bring the commercial use of aerospike engines closer to reality.

2.6 Nozzle Design

The design of a shock-free nozzle can be utilized for a specific ambient pressure and exit Mach number. A one-dimensional calculation can be performed but, for more precise results, especially for contoured nozzles, a more complex analysis must be implemented.

The function of a rocket's nozzle is to produce the maximum thrust as possible for a certain mass flow of propellant. This is achieved by expanding the exhaust gases completely until the ambient pressure is reached, in an isentropic process, with a parallel uniform flow at the exit plane [10]. The divergent of a bell nozzle, referred on Subsection 2.3.4, can be divided into two zones: the expansion section and the straightening section [31].

The expansion section benefits from a large favorable pressure gradient, which expands the exhaust gases from sonic to supersonic and even hypersonic velocities. This pressure gradient is so negative that the contour of this section can be simplified, for instance, as a circle's arc [31].

In contrast, the straightening section requires a more complex contour because the flow must be made axial at the design point, without inducing isentropic losses such as recompression shocks. The Prandtl-Meyer expansion lines can be used through the Method of Characteristics, explained in further detail in Section 3.4, to define such a contour.

The Method of Characteristics sometimes leads to very long and heavy nozzles, so some truncation aspects must be considered. Plus, the straightening section is crucial to define the nozzles efficiency as it defines the axiality of the exit flow and part of its interaction with the ambient.

2.6.1 Truncated Idealized Contoured (TIC) Nozzle

This contour belongs to the Gradual Expansion Nozzle class, and it is designed to achieve an uniform one-dimensional flow that is totally axial at the exit. The straightening section of the nozzle ends with no slope to achieve this goal without inducing shocks. To do so, this design results in a very long and heavy nozzle that is only practical for wind tunnels, where an uniform flow is crucial [32].

2.6.2 Thrust Optimized Contoured (TOC) Nozzle or Rao's Nozzle

This methodology follows the philosophy of a minimum length nozzle, so it offers the best specific impulse, with rocket and missile applications.

This is achieved by designing a nozzle with a sharper expansion section that has a strong expansion wave emanating from the throat. This design starts from a previously defined nozzle length, resulting in a contour that provides maximum thrust possible for a nozzle of such length. The thrust provided by the TOC nozzle is greater than that of a TIC contour that is shortened to the given length. Overall, the TOC nozzle offers better performance, especially for higher area ratios, compared to a TIC nozzle [10].

2.6.3 Compressed Truncated Ideal Contoured (CTIC) Nozzle

A shorter TIC nozzle is proposed, with a null slope at the exit, where the characteristic lines converge into a weak oblique shock that straightens the flow. The shock represents isentropic losses, with a decrease in flow velocity and increase of its pressure, but, since its an oblique shock, these effects are small. Additionally to the flow straightening, the smaller exit Mach number is also partially compensated by the bigger pressure [33].

Nonetheless, Rao's nozzles always outperform CTIC nozzles, even though the specific impulse differences are not significant, being as low as 0.04% for some operating conditions [34].

2.6.4 Aerospike Design

The Method of Characteristics can be used to implement the Prandtl-Meyer characteristic lines in the design of aerospikes, which are sometimes referred to as inside-out bell nozzles. Additionally, the truncation of this nozzle is a crucial aspect that requires consideration.

While more complex methods that approximate ideal rocket assumptions can be used, the final design typically has little difference from the Method of Characteristics [35].

In some cases, a three-dimensional analysis may be necessary for accurate results due to the asymmetrical nature of bell nozzles. However, linear aerospikes lack the revolution symmetry, making the two-dimensional analysis theoretically sufficiently accurate.

H. Greer [36] proposes an approximated method using the centered expansion fan on the lip of the throat and some geometric and isentropic considerations. Later, G. Angelino [37] develops a similar method but with each point of the contour being independently calculated.

Chapter 3

Theoretical Background

In this chapter, all the pertinent theoretical concepts necessary to understand and interpret the present dissertation are shown.

3.1 Thermodynamics Fundamentals

In one cubic centimeter of sea level air, the number of molecules is on the order of 10^{19}. While Newton's laws can be applied to the interactions between atoms, at a macro scale, the number of differential equations would be impossible to solve. Additionally, at a macro scale, the level of detail of the atomic level can be overlooked as the processes occur at a much larger scale than the individual atoms' motion and size.

For systems with a large number of molecules, thermodynamics and statistical physics offer a mean of analyzing these systems' properties at a macro scale with sufficient accuracy for real-world engineering studies. Therefore, the fluid can be considered a continuous medium.

There are intensive properties like pressure and temperature that don't depend on the mass of the thermodynamic system. If a room was divided in two, each new smaller room would have the same temperature and pressure. The opposite are extensive properties, which are examples mass, volume and energy [38].

3.1.1 Pressure, Temperature and Volume

Pressure is the result of atoms bombarding the wall that enclosures a fluid. Some other properties, such as temperature and entropy, are non-mechanical. Temperature represents the kinetic energy of the particles of a system, and there are many scales, with the Kelvin scale being the commonly used by scientists. Volume is the three-dimensional space a given object ocupies.

On a Pressure and Volume plot, isothermal lines can be drawn, as in Equation 3.1. Thus, pressure and volume are related to each other for a particular temperature. For instances, if the pressure is fixed at ambient conditions, and the temperature increases, the volume changes, generating a proportional constant between volume and temperature.

$$\phi(P, vol) = T \quad (3.1)$$

These three properties can be related in the equation of state for a closed system, as stated in Equation 3.2. Therefore, if one property is unknown, it can be found by relating it to the other two. The most well-known equation of state is the one presented in Equation 3.3, corresponding to an ideal gas [38].

$$f(P, vol, T) = 0 \quad (3.2)$$

$$Pvol = \nu RT \quad (3.3)$$

3.1.2 Adiabatic Process

An adiabatic process is defined as occurring in a thermally isolated system, where there are no heat transfers, although work can be done by and to the system. Fast expansions and compressions can be considered adiabatic processes, as significant heat exchange takes time to occur [38].

3.1.3 Work and Internal Energy

There are two ways for the system and the environment to exchange energy: work and heat.

In mechanical terms, work can be defined as the energy transfered through a force during a certain displacement. According to Newton's third law, the work done on the system by the environment and the work done by the system on the environment are of the same magnitude but with different signs.

In thermodynamics, work is formulated by Equation 3.4. For example, if the system is compressed, it receives energy, and positive work is done on the system in both isobaric and isothermal adiabatic compressions.

$$\delta W = -Pdvol \quad (3.4)$$

In the interaction between a system and the environment, work can be divided into two components, seen on Equation 3.5. Configurational work corresponds to a reversible process provoked by externally controlled parameters, such as volume, while dissipative work, resulting, for example, from two surfaces rubbing or the stirring of a liquid, is irreversible and always adds energy to the system as stated in Inequation 3.6.

$$\delta W = \delta W_{configurational} + \delta W_{dissipative} \quad (3.5)$$

$$\delta W_{dissipative} \geq 0 \quad (3.6)$$

The internal energy of a system, U, represents the sum of the particles' kinetic and potential energies. For an adiabatic system, the internal energy is related to work according to Equation 3.7.

$$U_2 = U_1 + W_{12} \quad (3.7)$$

This state quantity can be expressed as a function of temperature and volume, as suggested by Equation 3.8, which is called the caloric equation of state. For ideal gases, it only depends on temperature, as indicated by Equation 3.9, which introduces the heat capacity that will be further explored in Subsection 3.1.5 [38].

$$U = U(T, vol) \quad (3.8)$$

$$U = CT \quad (3.9)$$

3.1.4 Heat

By abandoning the consideration of an adiabatic system, the thermal contact between the system and the environment establishes a new term in the internal energy equation, as shown in Equation 3.10. This equation now considers the heat received or ceded by the system. This new formulation of the equation represents the first law of thermodynamics.

$$dU = \delta Q + \delta W \quad (3.10)$$

It must be stated that both heat and work are path functions, which means that they not only depend on the initial and final states but also on the way the system was moved from one state to the other.

From the prespective of the system, dissipative work performed on it can be viewed as the addition of heat, and this energy can also be expelled from the system as real heat. Therefore, dissipative work can now be formally viewed as reversible, and in many thermodynamic analyses, it is included in the heat parcel [38].

3.1.5 Specific Heat

The heat capacity is defined as the amount of heat energy required to raise the temperature of the system in one unit of temperature, as shown in equation 3.11. Its value depends on the type of process.

$$C = \frac{\delta Q}{dT} \quad (3.11)$$

For a perfect gas, the heat capacities and, consequently, the adiabatic index are considered constant over a wide range of temperatures. If heat is added at constant volume, the isochoric heat capacity is given by Equation 3.12. In this case, no work is done, and all heat is converted to internal energy, resulting in an increase in temperature. Equation 3.13 gives the isobaric heat capacity, which is the heat exchanged at constant pressure. In this process, if heat is received, the system expands, resulting in negative work, so the increase in internal energy is smaller. This means that the isobaric heat capacity is usually greater in value.

$$C_V = \left(\frac{\delta Q}{dT}\right)_{vol} \quad (3.12)$$

$$C_P = \left(\frac{\delta Q}{dT}\right)_P \quad (3.13)$$

It should also be mentioned that for an isothermal process, the heat capacity is infinite since there is no change in temperature. For an adiabatic process, at constant entropy, the heat capacity is null since the system is not in thermal contact with the environment.

The relationship between the isobaric and isochoric heat capacities found in Equation 3.14 gives the adiabatic index, which is particularly pertinent for compressible flow studies [38].

$$\gamma = \frac{C_P}{C_V} \quad (3.14)$$

3.1.6 Second Law of Thermodynamics

In reality, heat flows only in the direction of a negative temperature gradient. That said, according to the first law of thermodynamics, the opposite could be possible. To avoid this misconception, the second law of thermodynamics was introduced to consider energy quality, in addition to quantity. Therefore, the system with a higher temperature has ”energy of better quality”.

For a process to occur, both the first and second laws of thermodynamics must be satisfied. The second law of thermodynamics explains the losses experienced by real systems and sets limits for engineering systems. No heat engine can have 100% efficiency. Heat flow through a positive temperature gradient is possible, but only with external sources of energy, such as, for example, the work from the compressor of a refrigerator.

A reversible process is a concept where both the system and the environment can return to the original state without leaving any traces. Engineering processes are inevitably irreversible, although the concept of a reversible process can be applied in some analyses [39].

3.1.7 Entropy

Entropy is a property of a system that results from the second law of thermodynamics. It is defined as the measure of the molecular disorder or randomness of a system. Entropy can be generated and transferred but cannot be destroyed. All processes occur in the direction of increasing entropy, and there is no conservation of entropy. This means that the entropy of the universe is continually increasing.

Entropy can be transferred through heat flow and mass flow, which means that an adiabatic process in a closed system is also isentropic. A reversible process can return to the original state without any generation of entropy. The irreversibility of a system that generates entropy, represents a degradation in its engineering performance.

An isentropic process is both adiabatic and reversible.

However, it is possible for a certain system to experience a negative entropy exchange, as stated in Equation 3.15, if the entropy generated is inferior to the one transferred to the surroundings through a heat or mass transfer [40].

$$S_{exchange} = S_{transfer} + S_{generated} \quad (3.15)$$

3.2 Compressible Flow

3.2.1 Definition of Flow and Characterization

Fluid mechanics is a branch of classical physics that studies phenomena related to fluids, as opposed to solid bodies. A flow results from the interaction with a fluid, which continuously deforms with time under a shear force, comparing to the bending and deformation experienced by solid bodies. Both the liquid and vapor phases are considered fluids.

To solve the motion of a fluid, it is necessary to apply some basic laws of physics, such as the conservation of mass, Newton's second law of motion, the first and second laws of thermodynamics, and the principle of angular momentum, among other related principles.

Similar to thermodynamics, the assumption of a continuum medium, which ignores molecular discontinuities, is valid as the phenomena studied occur on a much greater scale compared to molecular interactions. Therefore, properties such as velocity, temperature, and density are considered continuous in classical fluid mechanics, both in time and space.

There are several ways to visualize a flow:

- **Pathline** – Represents the path followed by a particular particle in the flow. It can be obtained by taking a long exposure photograph of the flow after adding a single point marker such as smoke or colorant.
- **Streakline** – A line that is obtained when the marker is continuously added at a certain point in the flow, connecting the particles that have passed through that given point in space.
- **Streamline** – At every point of the flow, lines tangent to the velocity vectors can be established due to continuity. Streamlines are very important as there can be no flow exchange between two streamlines. In a two-dimensional flow, a stream function can be set for the whole flow, with each streamline having a unique value.
- **Timeline** –A line that connects some adjacent particles at a given point in time and is followed for a given time interval. This is useful, for example, when observing the flow's displacement caused by a shear force.

By definition, a steady flow has a velocity field that remains constant over time. This implies that streamlines are constant, and particles always remain on the same line. Consequently, streamlines, pathlines, and streaklines coincide in a steady flow.

Similarly to a solid's elasticity, fluids also have associated viscosity. As stated before, shear stresses induce a flow, and the relation between the shear stress and the shear rate or displacement is defined as viscosity, being constant for Newtonian fluids. If the Reynolds number of the flow, showed in Equation 3.16, is high enough, the viscosity effects are small compared to other flow phenomena. Additionally, the flow's rotationality, associated with viscous effects, can also be studied, which represents the particles' rotation.

$$Re = -\frac{\rho V D}{\mu_f} \quad (3.16)$$

The Reynolds Number also allows to predict the behavior of a flow. If it is low, a laminar flow occurs, where particles move in smooth layers. However, if it is high enough, a turbulent flow occurs, where particles chaotically mix due to random three-dimensional velocity fluctuations.

Lastly, depending on density variation consideration, the flow can be characterized as compressible or incompressible [41].

3.2.2 Definition of Compressible Flow

In a compressible flow, density cannot be assumed to be constant. Examining Equation 3.17, if the pressure experienced by a finite volume of fluid increases, compression occurs, resulting in a reduction in volume and an increase in density. The symbol τ represents the compressibility of the gas, which has different values for isothermal and isentropic processes.

$$\tau = -\frac{1}{vol}\frac{dvol}{dP} \quad (3.17)$$

High-speed flows are often initiated and propelled by strong pressure gradients. Therefore, the impact of pressure on the gas density cannot be ignored. Equation 3.18 relates the three main properties for any two states in isentropic gaseous flows [42].

$$\frac{P_1}{P_2} = \left(\frac{\rho_1}{\rho_2}\right)^{\gamma} = \left(\frac{T_1}{T_2}\right)^{\frac{\gamma}{\gamma-1}} \quad (3.18)$$

3.2.3 Speed of Sound and Mach Number

All particles within a fluid move in random directions with a certain velocity, attributing the fluid a specific internal energy. When a perturbation is applied to the fluid, it will excite nearby molecules, which will eventually collide with other molecules, transmitting the disturbance at a specific mean speed. This random kinetic propagation speed is known as the speed of sound, and it is dependent on the fluid and its internal energy, as described by Equation 3.19 for thermally and calorically perfect gases.

$$a = \sqrt{\gamma R T} \quad (3.19)$$

The Mach Number (MN) is defined as the ratio between the velocity of the flow and the velocity of sound, as shown in Equation 3.20. It represents the relationship between the flow's kinetic energy and the random molecular kinetic energy. Based on the MN, different flow regimes can be established, including:

- **Incompressible (MN < 0.3)** – Density variations are small, mostly because these flows are not associated with strong pressure gradients. Hence, this flow can be assumed to possess constant density.
- **Subsonic (0.3 < MN < 0.8 at freestream)** – Property variations are always continuous, and the flow exhibits straight and parallel streamlines that move, converge, and shape around any obstacle. In every point, the flow has a MN less than 1, but compressibility effects cannot be ignored.
- **Transient (0.8 < MN < 1)** – As the flow approaches the speed of sound, it is not possible to guarantee that all the flow is subsonic since it may accelerate while contouring an object, creating supersonic ”pockets.” Shocks can appear, indicating discontinuous changes in properties.
- **Supersonic (MN > 1)** – The entire flow moves faster than the speed of sound. Streamlines do not bend around objects, except when encountering a shock or experiencing an expansion wave. After a shock, the flow must remain supersonic.
- **Hypersonic (MN > 5)** – At such high speeds, a shock wave causes explosive changes in properties. The temperature can increase so much that molecular dissociation effects must be considered. Nothing particularly special happens at M = 5, as the referred phenomena increase with the MN, being just a convention.

$$M = \frac{V}{a} \quad (3.20)$$

The MN allows the calculation of the Mach Angle, as shown in Equation 3.21, which is half of the Mach Cone's angle. This structure, illustrated in Figure 3.1, forms around a body moving faster than the speed of sound. When the object is at position A, it emits sound that travels in an expanding circumference. At the time instance t, the former circumference has a radius of at, but the body moves a distance of Vt, emitting, in the meanwhile, more sound waves that form smaller intermediate circles. All these circles can have BC as their tangent, forming the Mach Cone that travels with the body. To be noted that the outside of the cone is called the silence zone, where the presence of the moving object cannot be heard.

$$\mu = sin^{-1}\frac{1}{M} \quad (3.21)$$

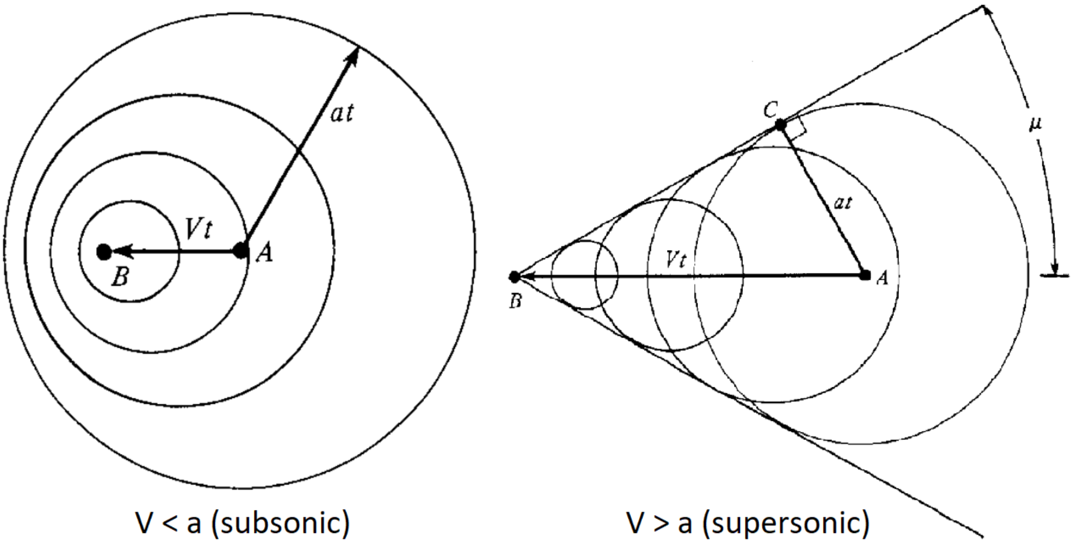

Figure 3.1: Propagation of a disturbance provoked by an object travelling at subsonic (left) and supersonic (right) speeds [42]

3.2.4 Stagnation Properties

All motion is described in relation to a reference frame. In compressible flow, an isentropic deceleration can be implemented until the flow becomes static in relation to such reference frame. The new values of the fluid's properties are called total or stagnation properties, identified with the suffix "0". In a rocket's nozzle, this reference state is the conditions at the combustion chamber, where the velocity can be ignored.

The static values of the properties are always associated with the stagnation ones and the velocity at which the fluid is moving, as described by Equations 3.22, 3.23 and 3.24. As the MN of the flow increases isentropically, these three static properties decrease.

$$\frac{T_0}{T} = 1 + \frac{\gamma - 1}{2} M^2 \quad (3.22)$$

$$\frac{P_0}{P} = \left(1 + \frac{\gamma - 1}{2} M^2\right)^{\frac{\gamma}{\gamma - 1}} \quad (3.23)$$

$$\frac{\rho_0}{\rho} = \left(1 + \frac{\gamma - 1}{2} M^2\right)^{\frac{1}{\gamma - 1}} \quad (3.24)$$

3.2.5 Reference State

The most common reference state for compressible flow is when the flow is accelerated or decelerated in an isentropic process until a sonic value is reached, which is highlighted with an asterisk. In a rocket's nozzle, this reference state is the condition at the throat.

By applying equations 3.22, 3.23, and 3.24 at MN equal to one, Equations 3.25, 3.26, and 3.27 are obtained, which establish the relation between the stagnation conditions and the reference state.

$$\frac{T^*}{T_0} = \frac{2}{\gamma + 1} = \left(\frac{a^*}{a_0}\right)^2 \quad (3.25)$$

$$\frac{P^*}{P_0} = \left(\frac{2}{\gamma + 1}\right)^{\frac{\gamma}{\gamma - 1}} \quad (3.26)$$

$$\frac{\rho^*}{\rho_0} = \left(\frac{2}{\gamma + 1}\right)^{\frac{1}{\gamma - 1}} \quad (3.27)$$

Equation 3.28 establishes a very important relation for nozzle's analyses, as it relates the reference state section area to the area the flow must isentropically expand to, so it achieves a certain MN. This comes from the assumptions of a quasi one-dimensional flow further explored in Subsection 3.2.9.

$$\frac{A}{A^*} = \frac{1}{M}\left[\frac{2}{\gamma+1}\left(1+\frac{\gamma-1}{2}M^2\right)\right]^{\frac{\gamma+1}{2(\gamma-1)}} \quad (3.28)$$

3.2.6 Normal or Strong Shock

Considering the normal shock depicted in Figure 3.2 and assuming steady flow, the absence of body forces, and the same area before and after the shock, Equation 3.29 represents flow continuity, taking into account the effects of compressibility. A normal shock is a very thin region characterized by a discontinuity in fluid properties. After passing through a normal shock, the pressure, density, and temperature increase, while the velocity decreases to subsonic values.

$$\rho_1 V_1 = \rho_2 V_2 \quad (3.29)$$

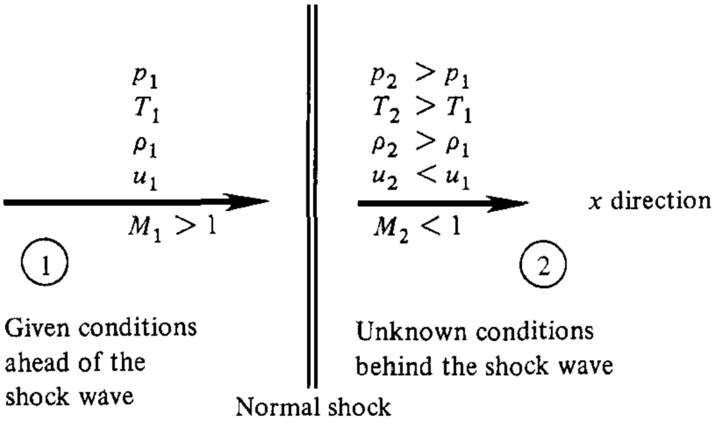

Figure 3.2: Schematics of a normal shock and properties' variations [42]

A shock represents a discontinuity in fluid properties that occurs in a very thin region with significant temperature and pressure gradients, where viscosity and dissipative effects are strongly felt. As a result, the process is not isentropic, and the relations in Equation 3.18 are no longer valid. But since no heat is added or removed from the flow, the process is adiabatic.

Equations 3.30, 3.31, 3.32, and 3.33 establish the properties of the flow across the normal shock through an adiabatic and irreversible process.

$$M_2^2 = \frac{1+\frac{\gamma-1}{2}M_1^2}{\gamma M_1^2 - \frac{\gamma-1}{2}} \quad (3.30)$$

$$\frac{\rho_2}{\rho_3} = \frac{(\gamma+1)M_1^2}{2+(\gamma-1)M_1^2} = \frac{V_1}{V_2} \quad (3.31)$$

$$\frac{P_2}{P_1} = 1 + \frac{2\gamma}{\gamma+1}(M_1^2 - 1) \quad (3.32)$$

$$\frac{T_2}{T_1} = \left[1 + \frac{2\gamma}{\gamma+1}(M_1^2 - 1)\right]\left[\frac{2+(\gamma-1)M_1^2}{(\gamma+1)M_1^2}\right] \quad (3.33)$$

Nonetheless, these equations admit that the flow before the shock can be subsonic (M<1). Therefore, the second law of thermodynamics must be taken into account through Equation 3.34. For an unitary MN, an isentropic $(s2 - s1 = 0)$ infinitely weak normal shock is obtained, and for a subsonic MN, a negative variation of entropy is predicted, which is physically impossible, as stated in Subsection 3.1.7.

$$s_2 - s_1 = c_p ln\left(\frac{T_2}{T_1}\right) - Rln\left(\frac{P_2}{P_1}\right) \quad (3.34)$$

Since this is an adiabatic process, the stagnation temperature remains the same. Nevertheless, the stagnation pressure drops, and it is related to the entropy gain as shown in Equation 3.35.

$$s_2 - s_1 = -Rln\left(\frac{P_{02}}{P_{01}}\right) \quad (3.35)$$

3.2.7 Oblique or Weak Shock

More broadly, shocks are considered oblique, as illustrated by Figure 3.3, and are formed when the flow must be deflected at a certain angle, θ, due to the presence of a concave surface. The streamlines are always parallel, changing direction discretely at the shock.

$$M_{n1} = M_1 \sin\beta \quad (3.36)$$

$$M_{t1} = M_1 \cos\beta \quad (3.37)$$

In Figure 3.4, the geometry of oblique shocks is depicted. The flow is decomposed into two components, one normal to the shock, according to Equations 3.36, which is analyzed as a normal shock, and one parallel component that is not affected by the shock, as per Equation 3.37. Note that β represents the shock angle that decomposes the velocity of the incoming flow, and θ represents the deviation experienced by the flow after the shock, coinciding with the concavity of the surface.

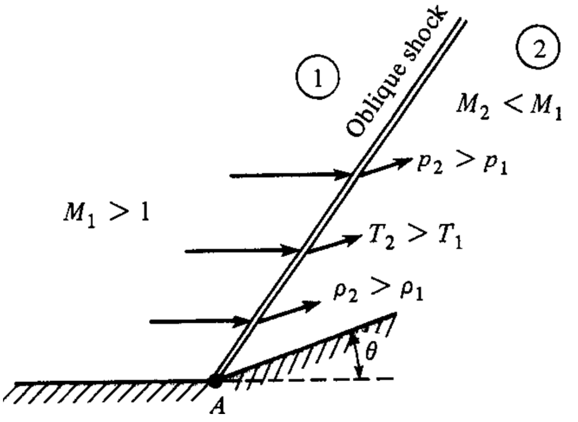

Figure 3.3: Schematics of an oblique shock and properties variations [42]

The MN after the oblique shock is obtained by Equation 3.38. The angles β and θ are related to each other according to Equation 3.39, which is graphically represented in Figure 3.5.

$$M_2 = \frac{M_{2n}}{\sin(\beta - \theta)} \quad (3.38)$$

$$\tan\theta = \frac{2}{\tan\beta}\left[\frac{M_1^2 \sin^2\beta - 1}{M_1^2(\gamma + \cos 2\beta) + 2}\right] \quad (3.39)$$

There is a maximum angle θ_{max} to which the flow can be deflected by a straight oblique shock. If the surface has $\theta > \theta_{max}$, the shock will be bent and flow detachment may be induced.

Similarly, if the deflection angle is fixed, as the MN decreases, the shock angle increases until it reaches the point where the previously defined θ equals the maximum possible deflection angle θ_{max} for that MN. Beyond this point, further decreases in the MN also do not have a straight shock solution.

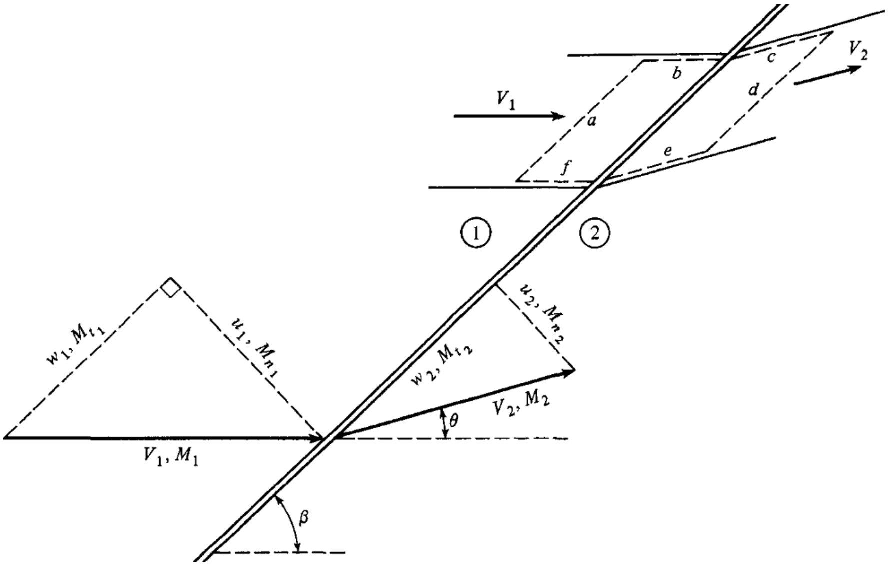

Figure 3.4: Detailed schematics of an oblique shock's geometry [42]

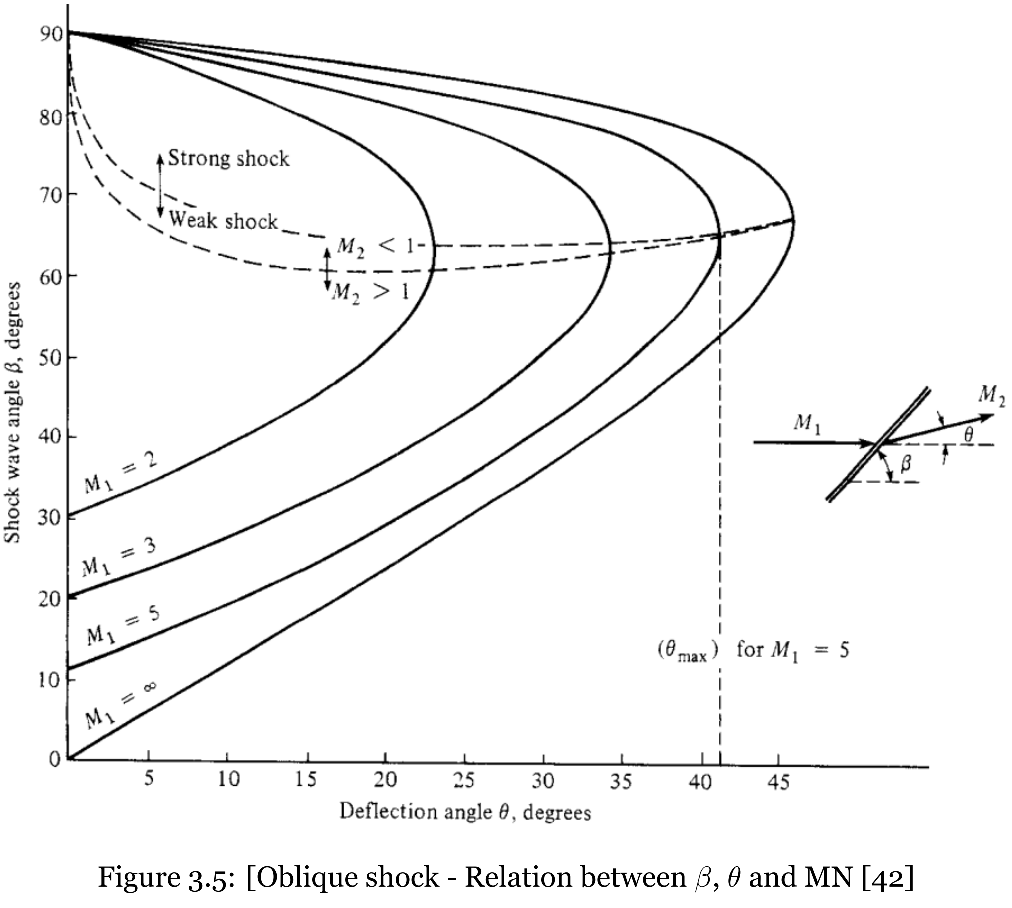

Figure 3.5: [Oblique shock - Relation between β, θ and MN [42]

For any given deflection angle, there are two possible shock wave angles. The smaller shock angle corresponds to the weak shock solution, with the flow after the shock remaining supersonic ($M_2 > 1$). The larger shock angle corresponds to the strong shock solution, with the flow after the shock being subsonic ($M_2 < 1$). The occurrence of each solution depends on the pressure conditions downstream in relation to the pre-shock flow. A strong pressure gradient will favor the strong shock solution, while a weaker gradient will favor the weak shock solution.

3.2.8 Prandtl-Meyer Expansion Fan

Looking at Figure 3.6, when a supersonic flow encounters a convex surface, it must deflect from itself, corresponding to an expansion, as opposed to an oblique shock. Here, the velocity increases, and the density, pressure, and temperature decrease. Also, these changes in properties are so smooth, that they can be assumed to be continuous, corresponding to an isentropic process. This occurs because the expansion is composed of a fan of waves, each of which contributes to infinitesimally accelerate the flow.

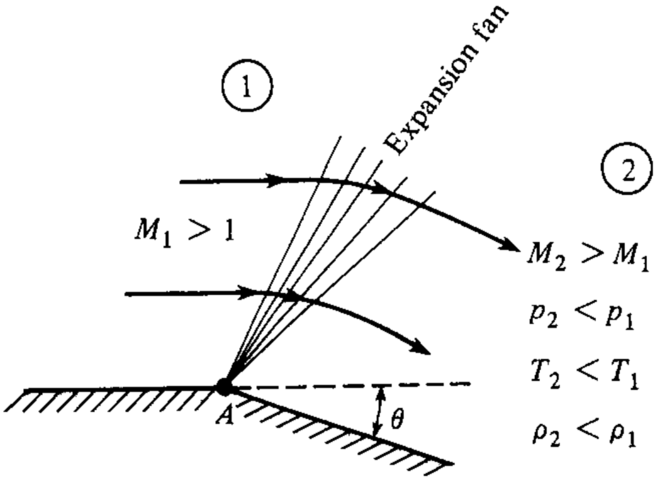

Figure 3.6: Schematics of a Prandtl-Meyer expansion centered fan and properties variations through it [42]

Basically, the vertex in Figure 3.6 promotes the creation of infinitesimal Mach lines, that emanate from it and expand the flow. This Mach lines are characteristic lines, with properties constant between them, as explained in Section 3.4.

Due to the isentropic behavior, the changes in the flow's temperature and pressure are given by Equations 3.40 and 3.41, respectively. Density can then be easily calculated using Equation 3.18.

$$\frac{T_2}{T_1} = \frac{1 + \frac{\gamma-1}{2} M_1^2}{1 + \frac{\gamma-1}{2} M_2^2} \quad (3.40)$$

$$\frac{P_2}{P_1} = \left[\frac{1+\frac{\gamma-1}{2}M_1^2}{1+\frac{\gamma-1}{2}M_2^2}\right]^{\frac{\gamma}{\gamma-1}} \quad (3.41)$$

The Prandtl-Meyer angle is defined by Equation 3.42 for a certain MN. As for the reflection angle, it is simply given as the difference between the Prandtl-Meyer angle before and after the expansion, as stated in Equation 3.43.

$$\nu(M) = \sqrt{\frac{\gamma+1}{\gamma-1}}\tan^{-1}\sqrt{\frac{\gamma-1}{\gamma+1}(M^2-1)} - \tan^{-1}\sqrt{M^2-1} \quad (3.42)$$

$$\theta = \nu(M_2) - \nu(M_1) \quad (3.43)$$

3.2.9 Quasi-One-Dimensional Flow

Similar to unidimensional flow, quasi-one-dimensional flow will also allow for variations in area. A control volume for quasi-one-dimensional flow can be suggested, as shown in Figure 3.7, but with smooth wall angles, to prevent shock formation. Although the geometry is two-dimensional, the fluid properties are still assumed to be dependent only on the direction of the flow, meaning that they are constant throughout any given cross-sectional area.

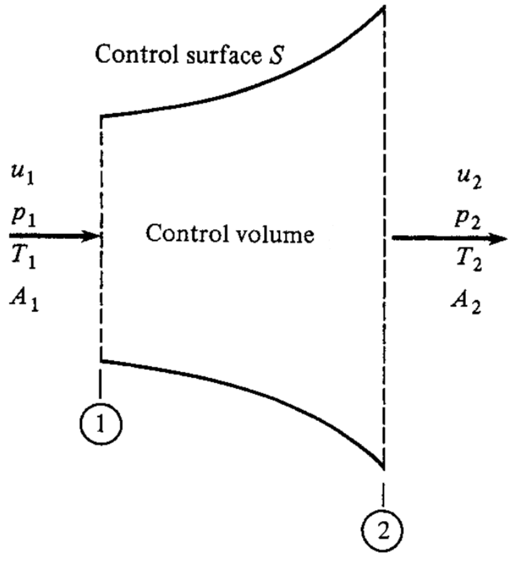

Figure 3.7: Control volume for quasi-one-dimensional flow [42]

This flow is considered adiabatic and isentropic. The continuity equation also considers the transversal area, as suggested in Equation 3.44. This leads to the relation between area and MN stated in equation 3.45.

$$\rho_1 V_1 A_1 = \rho_2 V_2 A_2 \quad (3.44)$$

$$\frac{dA}{A} = (M^2 - 1)\frac{du}{u} \quad (3.45)$$

For subsonic velocities, area and velocity vary in different directions. In a rocket nozzle, this results in a decreasing area in the convergent to accelerate the flow. For supersonic velocities, area and velocity follow the same trajectory. Therefore, if the area increases, as in a rocket nozzle's divergent, the velocity also increases. As for sonic velocities, Equation 3.46 suggests that a minimum area is reached, which in a rocket nozzle represents the throat.

$$\frac{dA}{A} = 0 \quad (3.46)$$

The area-MN relation, given by Equation 3.28, shows that the MN at any location in the duct is a function of the ratio between the local duct area and the sonic throat area. There are two solutions, a subsonic and a supersonic one. As this is an isentropic process, the relations for this type of process can be easily applied to solve the flow properties at any point in the duct.

3.2.10 Final Considerations about Compressible Flow

Real supersonic flows are complex, and many of the explanations previously stated involve inherent simplifications, such as considering an ideal gas, adiabatic and isentropic processes, among others. However, the scope of this dissertation is limited to supersonic flows with M<5, and a higher level of detail is not necessary, with the present explanations being sufficient to achieved the proposed goal.

3.3 Nozzle Phenomena

3.3.1 Operation Critical Points

Now that shocks waves and expansion fans are more deeply understood, the phenomena referred to in Subsection 2.3.6 can be look at with further detail, starting with understanding the flow behavior by manipulating the operational pressure ratio $(P_{chamber}/P_{amb})$ and changing the ambient pressure to which the flow must equal at the exit.

Flow begins subsonic through the entire nozzle when the outside pressure starts to drop from the chamber's pressure. As the pressure ratio increases, the flow accelerates until it reaches a sonic value at the throat, causing the flow to chock. Beyond the throat, the flow compresses in the divergent section, and it remains subsonic. This point is called the first critical point and is represented in Figure 3.8 by curve a. Any infinitesimal decrease in the outside pressure beyond the first critical point will cause the flow in the divergent section to change from subsonic to supersonic.

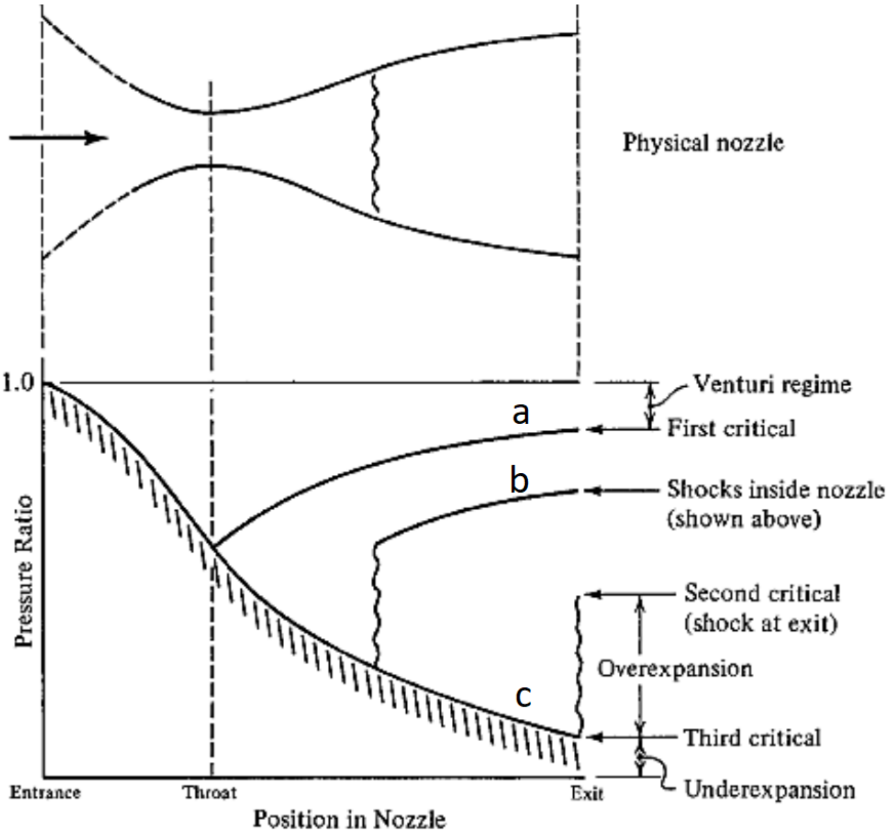

Figure 3.8: Nozzle's modes of operation [43]

Now that there is a supersonic flow in the divergent section, the greater pressure gradient promotes a more aggressive expansion than the one needed to equal the ambient pressure. Thus, a shock forms inside the divergent section, starting at the throat and moving to the exit plane as the pressure drops and a bigger non-isentropic compression is needed.

After the shock, the flow becomes subsonic and uses the remaining divergent section as a compressor. This is represented by line b in Figure 3.8. When the outside pressure is low enough, the shock reaches the exit plane, as suggested by line c in the same figure, representing the second critical point.

After the second critical point, the flow will not be able to expand much further even if the ambient pressure keeps dropping. However, it still reaches the exit plane at higher pressures than the ambient. Therefore, the normal shock at the exit begins to turn oblique, with its intensity/angle reducing as the outside pressure decreases. This phenomenon is known as an overexpanding nozzle.

The oblique shock will eventually reach a 0° angle, representing no shock at all, and the nozzle reaches its third critical point. At this point, the flow is isentropic and is used as the nozzle's design point.

Further decreases in outside pressure will cause the flow to have a pressure higher than the ambient pressure at the exit, which is known as underexpansion. In this case, expansion fans will be generated from the nozzle's lips to allow the flow to be further expanded beyond the exit plane.

3.3.2 Overexpansion and Underexpansion Phenomena

The overexpansion occurs when the ambient pressure is higher than the one at the third critical point. A weak shock is needed at the exit so that the flow pressure increases until it matches the ambient pressure.

But the oblique shock will deviate the flow, so a second shock is needed to realign the flow. This will increase the pressure, making it higher than the ambient pressure, so now an expansion fan is needed to expand the flow and match the ambient pressure once again.

The expansion fan also deviates the flow, requiring another expansion fan to straighten the flow, returning it to a state where its pressure is once again below the ambient pressure.

The process repeats itself, as shown in Figure 3.9b), forming a structure known as the Mach Diamond. The underexpansion process, depicted in Figure 3.9a), is similar, but starts with a pair of expansion fans at the exit .

3.4 Method of Characteristics

Quasi-one-dimensional flow allows for a simple analysis that predicts supersonic flow behavior through a nozzle. However, because it fails to consider the velocity and other flow properties in two dimensions, it cannot deliver contour analyses. To achieve this, a more complex two-dimensional analysis is needed, but it does not have an analytical solution.

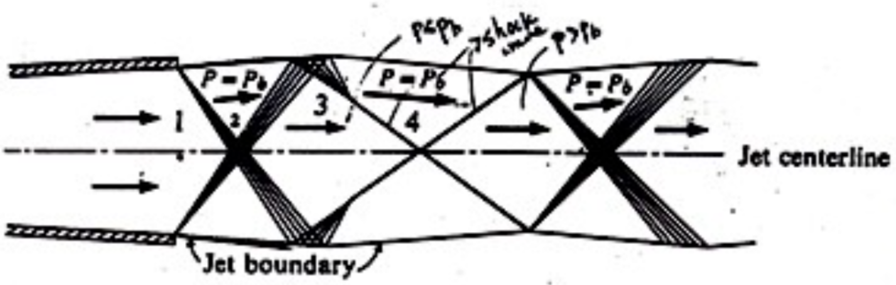

a) Underexpanded supersonic nozzle

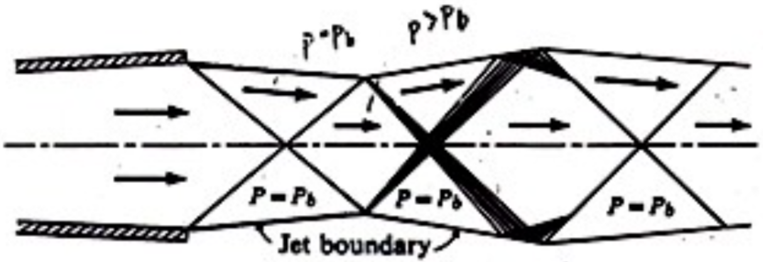

b) Overexpanded supersonic nozzle

Figure 3.9: Flow phenomena outside an a) underexpanded and b)overexpanded nozzle [44]

The Method of Characteristics (MOC) is considered part of Computational Fluid Dynamics (CFD), which seeks to discretely solve the flow for certain points and instances. It involves a discrete method of solving the potential velocity equation, which is a partial differential equation (PDE), such that in certain points, the velocity vectors are known.

To achieve this, the MOC utilizes characteristic lines, which are part of the mathematical definition of a PDE. These lines have a constant relation between some of the flow's velocity angles along them, which allows for the comparison of different points starting from ones where the flow is known.

In order to apply the MOC, the flow must be assumed to be supersonic, steady, inviscid (with boundary layer effects neglected), irrotational, and two-dimensional [42].

3.4.1 Finding a Characteristic Line

Let's begin by considering the velocity potential as a function in the two-dimensional reference frame, as stated in Equation 3.47. Each index represents a derivative, as indicated by Equation 3.48. Equation 3.49 represents the velocity vector, with its components given by Equations 3.50 and 3.51

$$\Phi = f(x, y) \quad (3.47)$$

$$\Phi_a = \frac{\partial \Phi}{\partial a} \quad and \quad \Phi_{ab} = \frac{\partial^2 \Phi}{\partial a \partial b} \quad (3.48)$$

$$\overrightarrow{V} = u\hat{\imath} + v\hat{\jmath} \quad (3.49)$$

$$u = V\cos\theta \quad (3.50)$$

$$v = V\sin\theta \quad (3.51)$$

The potential velocity in Equation 3.52 can be obtained by combining the continuity equation and Euler's equation for a two-dimensional, irrotational flow. This is a nonlinear (PDE) that becomes a hyperbolic equation if equation 3.53 is satisfied, which occurs for supersonic flow.

$$\left[1 - \frac{\Phi_x^2}{a^2}\right]\Phi_{xx} + \left[1 - \frac{\Phi_y^2}{a^2}\right]\Phi_{yy} - \frac{2\Phi_x\Phi_y}{a^2}\Phi_{xy} = 0 \quad (3.52)$$

$$\frac{\Phi_x^2 + \Phi_y^2}{a^2} > 1 \quad (3.53)$$

The direction lines that characterize the hyperbola are called characteristics, and in the case of the velocity potential in supersonic flows, they coincide with the Mach lines.

In this example, the velocity components are the flow properties being studied, and in theory, they should always be continuous if no shock is formed. Yet, the first derivative must be indeterminate along a characteristic line, allowing for several different flows (streamlines) to be crossed by this line. This statement applies to every flow property due to the relationships between velocity (or MN), pressure, density, and temperature.

The velocity potential is a function of x and y, and, therefore, its derivatives are given by Equations 3.54 and 3.55.

$$d(\Phi_x) = du = \Phi_{xx}dx + \Phi_{xy}dy \quad (3.54)$$

$$d(\Phi_y) = dv = \Phi_{xy}dx + \Phi_{yy}dy \quad (3.55)$$

By combining Equations 3.52, 3.54 and 3.55 in a system of linear algebraic equations with variables Φ_{xx}, Φ_{yy} and Φ_{xy}, and solving for Φ_{xy}, using Crammer's rule and applying the definitions of Equation 3.48, Equation 3.56 can be obtained.

$$\Phi_{xy} = \frac{\begin{vmatrix} 1-\frac{u^2}{a^2} & 0 & 1-\frac{v^2}{a^2} \\ dx & du & 0 \\ 0 & dv & dy \end{vmatrix}}{\begin{vmatrix} 1-\frac{u^2}{a^2} & \frac{-2uv}{a} & 1-\frac{v^2}{a^2} \\ dx & dy & 0 \\ 0 & dx & dy \end{vmatrix}} = \frac{Numerator}{Denominator} \quad (3.56)$$

As stated before, along a characteristic line, the derivatives of the flow are indeterminate, so mathematically, they can be found where both the numerator and denominator of Equation 3.56 equal zero. This occurs when moving in a direction dy/dx around a given point in the flow with known properties.

For a given point A, setting the denominator of Equation 3.56 to zero results in Equation 3.57. The slope of the characteristic lines that pass through the same point can then be obtained using Equation 3.59. Equation 3.58 represents a middle step between the two previous equations [31].

$$\left[1-\frac{u^2}{a^2}\right]\left(\frac{dy}{dx}\right)^2_{char} + \left[1-\frac{v^2}{a^2}\right] + \frac{2uv}{a^2}\left(\frac{dy}{dx}\right)^2_{char} = 0 \quad (3.57)$$

$$\left(\frac{dy}{dx}\right)_{char} = \frac{\frac{-uv}{a^2} \pm \sqrt{\frac{u^2+v^2}{a^2} - 1}}{1-\frac{u^2}{a^2}} \quad (3.58)$$

$$\left(\frac{dy}{dx}\right)_{char} = tan(\theta \pm \mu) \quad (3.59)$$

Taking Equation 3.59 into account, it is clear that, for supersonic flow, there are two characteristic lines passing through point A. If the flow is sonic, there is only one characteristic line whose slope equals the Mach angle. If the flow is subsonic, Equation 3.21 yields an imaginary Mach angle, indicating that the characteristic lines are elliptical [42].

Looking at Figure 3.11, two characteristics pass through a given point A: C_+ with a slope of $tan(\theta + \mu)$ and C_- with a slope of $tan(\theta - \mu)$.

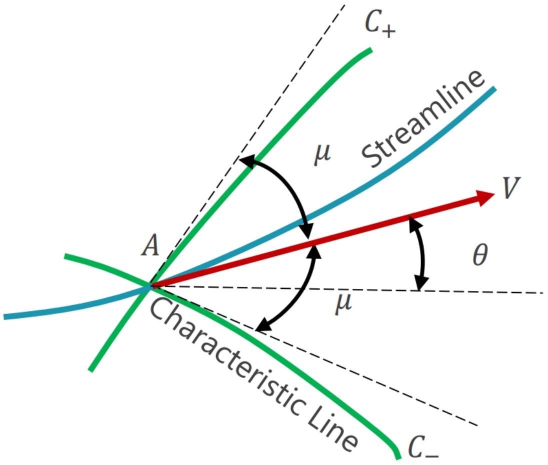

Figure 3.10: Characteristic lines passing a given point of a supersonic flow [31]

3.4.2 Using Characteristics to Solve the Flow

To solve the flow along a characteristic line, the governing PDE describing the flow reduces to ordinary differential equations (ODE), also known as compatibility equations. These equations are obtained by setting the determinant of the numerator in Equation 3.56 to zero, resulting in Equation 3.60.

$$\frac{dv}{du} = -\frac{1-\frac{u^2}{a^2}}{1-\frac{v^2}{a^2}}\left(\frac{dy}{dx}\right)_{char} \quad (3.60)$$

If only the denominator equals zero, Φ_{xy} will have an infinite value for the direction of the characteristic line, which is a physical inconsistency. Therefore, the numerator must also equal zero in such a direction so that a finite but indeterminate value of Φ_{xy} may exist. This is the fundamental principle that makes Equation 3.60 true in the direction of the characteristic lines [42].

Equation 3.61 represents the set of ODEs obtained from Equation 3.60 by performing some algebraic manipulation. After integrating, it is solved with the Prandtl-Meyer Equation, as shown in Equations 3.62 and 3.63.

$$d\theta = \pm\sqrt{M^2 - 1}\frac{dV}{V} \quad (3.61)$$

$$\theta + \nu(M) = c^{te.} = K_- \;\; along \;\; C_- \quad (3.62)$$

$$\theta - \nu(M) = c^{te.} = K_+ \;\; along \;\; C_+ \quad (3.63)$$

If the flow is unknown but its characteristic constants have been determined, Equations 3.64 and 3.65 can be used to obtain the flow deviation and Prandtl-Meyer angle, respectively. Then, Equation 3.42 can be applied to find the Mach number (MN). Assuming an isentropic expansion, Equations 3.40 and 3.41 can be used to calculate the temperature, pressure, and then density. Finally, the velocity of sound and flow velocity can also be found [31].

$$\theta = \frac{1}{2}\left[(K_-) + (K_+)\right] \quad (3.64)$$

$$\nu(M) = \frac{1}{2}\left[(K_-) - (K_+)\right] \quad (3.65)$$

In Figure 3.11, if θ and the MN are known for both point 1 and point 2, K_- and K_+ can be calculated using Equations 3.62 and 3.63. Once K_- and K_+ have been obtained, the flow in point 3 can be solved using equations 3.64 and 3.65.

3.4.3 Method of Characteristics for Nozzle Design

The implementation of the MOC for the nozzle contour design of an aerospike will be further explored in Section 4.1.2.

In a more general approach, the theory assumes that the flow properties are known for the throat, from which characteristic lines emanate to form a grid. The MOC is then used to solve the nodes of the formed grid until the desired exit MN is found and the flow is as

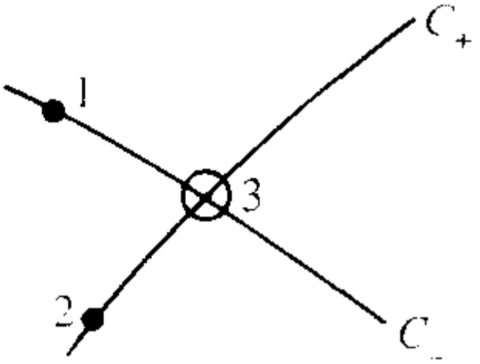

Figure 3.11: Unit process for the steady-flow, two-dimensional, irrotational MOC [42]

straight as desired. Essentially, the flow is mapped out throughout these nodes.

3.5 Computational Fluid Dynamics (CFD)

CFD is a powerful tool for studying flows and their interactions with surfaces. By creating a discrete fluid domain using finite elements and solving the governing equations iteratively, it is possible to obtain accurate values for the properties of the flow. Whether using Navier-Stokes or Lattice Boltzmann methods, the process culminates in analyzing the solved flow to consult the desired results [45].

3.5.1 Governing Equations

The goal of a CFD simulation is to solve a physical problem by respecting certain governing equations. For the scope of this dissertation, which involves a single-phase compressible flow without studying the effects of combustion or radiation, there are three governing equations that must be obeyed.

The first is Equation 3.66 and represents conservation of mass for a two-dimensional flow in Cartesian coordinates. It is based on the concept that mass cannot be created nor destroyed [46].

$$\frac{\partial \rho}{\partial t} + \nabla \cdot \rho \overrightarrow{V} = \frac{\partial \rho}{\partial t} + \frac{\partial (\rho u)}{\partial x} + \frac{\partial (\rho v)}{\partial y} = 0 \quad (3.66)$$

Next, Equation 3.67 represents the conservation of momentum, where F_b' stands for body forces that typically reduce to the force generated by gravitational acceleration. This equation is a rewriting of Newton's second law for flow analysis and takes into account Reynolds transport and divergence theorems. The viscous stress tensor can be solved with velocity derivatives, as suggested by Navier and Stokes, giving rise to Equation 3.68, where δ_{ij} is the Kronecker delta. Joining all these equations together results in Equation 3.69, which can be extended for a two-dimensional Cartesian geometry, as suggested by Equations 3.70 and 3.71 [47].

$$\frac{\partial(\rho\overrightarrow{V})}{\partial t} + \overrightarrow{V} \cdot \nabla(\rho\overrightarrow{V}) = -\nabla P + \nabla \cdot \bar{\bar{\tau}} + \overrightarrow{F_b'} \quad (3.67)$$

$$\bar{\bar{\tau}}_{ij} = 2\mu_f \left[\frac{1}{2}\left(\frac{\partial u_i}{\partial x_j} + \frac{\partial u_j}{\partial x_i}\right) - \frac{1}{3}\nabla \cdot \overrightarrow{V}\delta_{ij}\right] \quad (3.68)$$

$$\rho\left(\frac{\partial\overrightarrow{V}}{\partial t} + \overrightarrow{V} \cdot \nabla\overrightarrow{V}\right) = -\nabla P + \mu_f \nabla^2\overrightarrow{V} + \frac{1}{3}\mu_f\nabla(\nabla \cdot \overrightarrow{V}) + \overrightarrow{F_b'} \quad (3.69)$$

$$\rho\left(\frac{\partial u}{\partial t} + u\frac{\partial u}{\partial x} + v\frac{\partial u}{\partial y}\right) = -\frac{\partial P}{\partial x} + \frac{\partial}{\partial x}\left[2\mu_f\frac{\partial u}{\partial x} - \frac{2}{3}\mu_f\left(\frac{\partial u}{\partial x} + \frac{\partial v}{\partial y}\right)\right] + \frac{\partial}{\partial y}\left[\mu_f\left(\frac{\partial u}{\partial y} + \frac{\partial v}{\partial x}\right)\right] + F_{b,x} \quad (3.70)$$

$$\rho\left(\frac{\partial v}{\partial t} + u\frac{\partial v}{\partial x} + v\frac{\partial v}{\partial y}\right) = -\frac{\partial P}{\partial y} + \frac{\partial}{\partial x}\left[\mu_f\left(\frac{\partial v}{\partial x} + \frac{\partial u}{\partial y}\right)\right] + \frac{\partial}{\partial y}\left[2\mu_f\frac{\partial v}{\partial y} - \frac{2}{3}\mu_f\left(\frac{\partial u}{\partial x} + \frac{\partial v}{\partial y}\right)\right] + F_{b,y} \quad (3.71)$$

Lastly, Equation 3.72 represents the conservation of energy, and is a clear application of the first law of thermodynamics. It allows for the setting of another unknown property in the flow model, temperature, in addition to the properties of density, pressure and velocity components.

$$\frac{\partial(\rho e_t)}{\partial t} + \nabla \cdot \left[\overrightarrow{V}(\rho e_t + P)\right] = \nabla \cdot \left[k\nabla T + (\bar{\bar{\tau}} \cdot \overrightarrow{V})\right] + \dot{S}_g \quad (3.72)$$

With these governing equations and suitable boundary conditions, it is possible to solve the flow and determine its properties at every point. However, suitable modeling assumptions are necessary in order to reduce the complexity of the problem [48].

3.5.2 CFD Process

Commercial CFD tools are used to solve flow problems, and to achieve this goal, a group of actions must be implemented, known as the CFD process. These actions include [49]:

1. **Formulate the Flow Problem** –This involves answering questions about the objective of the analysis, the geometry and spatial dimensions, and the flow's characteristics, such as laminar or turbulent, inviscid or viscous, compressible or incompressible, among others.
2. **Model the Geometry and Flow Domain** –Using computer-aided design (CAD) software, the geometry of the flow domain must be created, including all objects in the flow's boundaries and free boundaries over which flow enters or leaves. The structure and topology of the grid generation must also be taken into account.
3. **Establish the Boundary and Initial Conditions** – The flow's domain is a finite volume that requires physical condition on its boundaries. The iterative model starts with a given initial solution that must be defined.
4. **Generate the Grid** – The flow's domain is discretized using finite elements, and the grid spacing must adapt to the expected behavior of the flow, thickening where big properties' gradient are expected. The clustering of the grid must be normal to a given surface, with the first point within the viscous sublayer with y^+ less than 1.
5. **Establish the Simulation Strategy** – Computational resources, available time, and desired accuracy must be balanced to choose a turbulence model.
6. **Establish the Input Parameters and Files** – The grid is uploaded, initial and boundary conditions are inserted and the chosen strategy is set.
7. **Perform the Simulation** – With everything set, the computer solves the flow. Interactive, batch, and distributed processing options are available.
8. **Monitor the Simulation for Completion** – The simulation is considered complete once the solution converges, meaning its residuals are smaller than those defined in the simulation strategy.
9. **Post-Process the Simulation to get the Results** - Once the flow is solved, graphics, streamlines, vector fields, etc..., can be obtained, as well as values like pressure forces.
10. **Make Comparisons of the Results** – To validate the obtained results, they must be compared with experimental studies or other computational methods.
11. **Repeat the Process to Examine Sensitivities** – For more in-depth studies, changing initial or boundary conditions, dimensions, models, etc..., allows for an increased understanding of the simulated phenomena.
12. **Document** – Writing documents that explain the entire process in detail and expose the findings.

3.5.3 Turbulence Models

The occurrence of laminar or turbulent flow is dependent on the relative influence of viscous and inertial effects, as described by the Reynolds number. As the Reynolds number increases, the development of a laminar flow into a turbulent flow becomes more likely.

Turbulent flow is characterized by the existence of eddies that create large fluctuations in velocity and other properties, as depicted in Figure 3.12. Reynolds' decomposition states that the value of a velocity component at a certain point is the sum of its average value and a fluctuation that is a function of time, as seen in Equations 3.73 and 3.74. It is important to note that turbulent motion is random, and therefore a statistical treatment is essential [50].

$$u(t) = \bar{u} + u'(t) \quad (3.73)$$

$$v(t) = \bar{v} + v'(t) \quad (3.74)$$

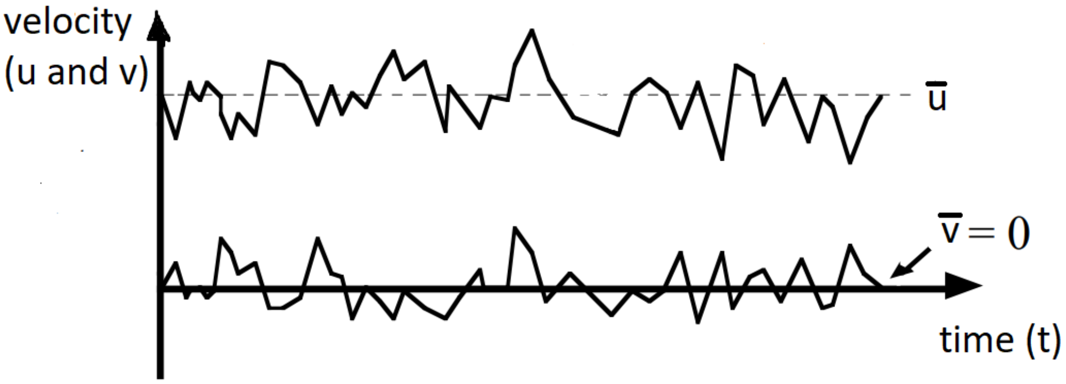

Figure 3.12: Velocity fluctuations in a fixed point of a turbulent flow [50]

In summary, turbulent flow is irregular, highly diffusive and dissipative, three-dimensional, and has a large Reynolds number. The eddies that characterize turbulence transfer their kinetic energy to smaller eddies in a process called the energy cascade. This continues until the eddies become so small that the viscous stresses are enough to dissipate the kinetic energy into internal energy. These small scales are also called Kolmogorov scales and are much smaller than the characteristic length of the flow. They can be approximated with isotropic properties, although the flow is still considered a continuum medium.

To model turbulence in CFD, Reynolds decomposition must be applied to the governing equations, such as the Reynolds-Averaged Navier-Stokes (RANS) equations. In RANS and other governing equations, the values of properties such as velocity, pressure and other scalars are replaced by their average, leaving a term called the Reynolds tensor, $\overline{u_i'u_j'}$, with the fluctuations. Turbulence models propose ways to handle the Reynolds tensor by adding more equations and variables to the physical model, reflecting assumptions [51].

The Reynolds tensor can be related to the mean velocity gradients through Equation 3.75 by adding a new variable, μ_t, called turbulent viscosity, which is dependent on the flow characteristics rather than the fluid conditions, unlike dynamic viscosity. This modulation of the Reynolds tensor is known as the Boussinesq Approach, and the turbulence models presented in this Subsection are introduced in order to compute the turbulent viscosity. It offers a relatively low computational cost since it assumes the turbulent viscosity to be an isotropic scalar, being sufficiently accurate for wall boundary layers, mixing layers, jets, etc.., where the flow's shear is dominated by only one of the turbulent shear stresses.

$$-\rho\overline{u_i'u_j'} = \mu_t\left(\frac{\partial u_i}{\partial x_j} + \frac{\partial u_j}{\partial x_i}\right) - \frac{2}{3}\left(\rho k + \mu_t\frac{\partial u_k}{\partial x_k}\right)\delta_{ij} \quad (3.75)$$

The Spalart-Allmaras model only adds one transport equation, representing the turbulent viscosity. It was specially developed for aerospace applications, namely, wall-bounded flows, with accurate results for adverse pressure gradients. Nonetheless, it shows larger errors for some free shear flows, especially plane and round jet flows.

The $k-\varepsilon$ model is a high-Reynolds number model and adds two equations: one to model the turbulence kinetic energy, k, and another to model the turbulence dissipation rate, ε. Very favored in industrial flow and heat transfer simulations, this semi-empirical model provides a fair accuracy for a wide range of flows with an economic usage of computational resources. In its standard form, it assumes that the flow is fully turbulent, ignoring the effects of molecular viscosity.

The RNG $k-\varepsilon$ model is more accurate and reliable for a wider class of flows, and derives from the standard version by adding a statistical technique called renormalization group theory (RNG). Some of the improvements are explained by: an extra term in the turbulence dissipation rate equation capable of improving the accuracy for rapidly strained flows, considering swirl effects, instead of user-specified and constant turbulent Prandtl numbers the statistics gives an analytical formula for it, and an analytically-derived differential formula for effective viscosity providing means to simulate low-Reynolds number flows.

The realizable $k-\varepsilon$ model is a relatively recent approach that satisfies mathematical constraints associated with Reynolds stresses. Therefore, this model offers improved correspondence to the physical phenomena observed in turbulent flows. It achieves this by employing an alternative modulation of turbulent viscosity and dissipation rate. The dissipation rate is obtained from an exact equation for the transport of mean-square vorticity fluctuations. Similar to the RNG $k - \varepsilon$ model, the realizable $k - \varepsilon$ model demonstrates superior performance, particularly in flows characterized by strong streamline curvature, vortices and rotation.

Lastly, the $k - \omega$ model is an empirical model and adds two equations: one to model the turbulence kinetic energy, k, and another to model the specific turbulence dissipation rate, ω. It suits low-Reynodls numbers, compressibility and shear flow spreading. Originally it was freestream sensitive but has been improved over the years so it can predict free shear flows [52].

3.5.4 Modeling the Flow Near the Wall

Due to the consideration of viscosity, the first layer of fluid immediately next to the wall has null velocity. This drastically changes the mean value of properties, so special attention needs to be taken in this zone of the flow. Moreover, the gradients of mean velocity provoked by the viscous damping between the free flow and the wall promote the creation of turbulent kinetic energy, which increases turbulent effects.

For an accurate turbulent simulation, wall effects must be considered as they are the main source of mean vorticity and turbulence. To do so, three regions must be considered, as shown in Figure 3.13:

- **Viscous Sublayer (y^+ < 5)** –Due to viscous damping, low velocity is felt in this region and the flow can be considered almost laminar. Molecular viscosity plays a key role in momentum and heat transfer.
- **Buffer Layer (5<y^+<30)** – It is an intermediate region where both viscosity and turbulent effects must be considered.
- **Fully Turbulent Region (y^+>30)** – Turbulent effects are intense and far superior to viscosity.

$$y^+ = \sqrt{\tau_w \rho} \frac{y}{\mu_f} \quad (3.76)$$

There are two ways to solve the flow in this region. The first approach, named the wall function approach, consists of creating "wall functions" that represent the contribution of the viscous region (sublayer and buffer), so the turbulent models don't need adjustments near the wall. As an alternative, the near-wall approach solves the viscous zones with a mesh that adapts to the higher gradients in the region with a more refined grid. Both approaches can be seen in Figure 3.14 [52].

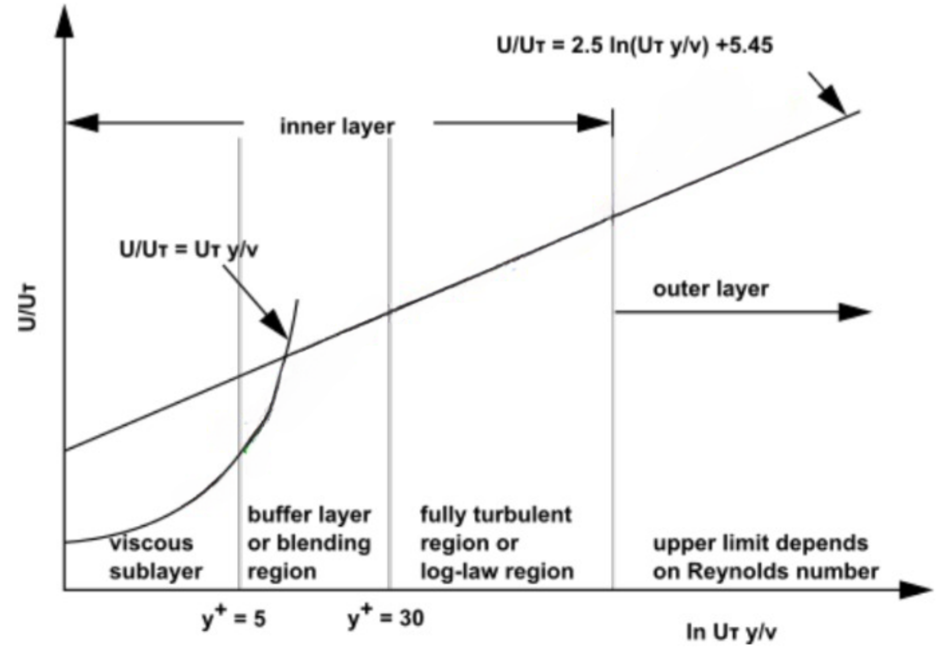

Figure 3.13: Subdivisions of the near-wall region, with y^+ being the dimensionless distance from the wall defined by Equation 3.76 [52]

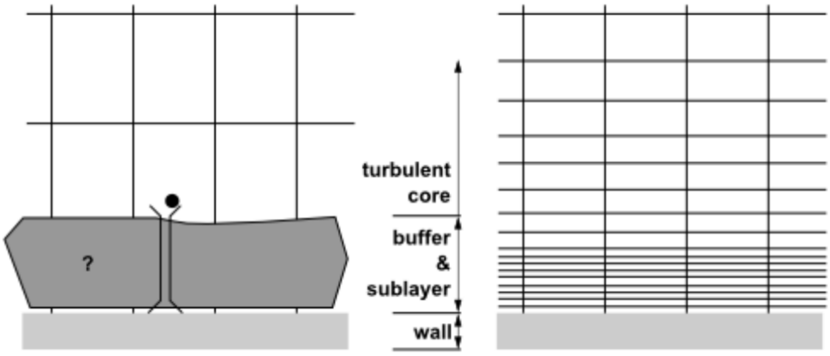

Figure 3.14: Mesh of the wall function left) and near-wall (right) approaches [52]

Typically, the mesh should have 10-20 cells near the wall in order to cover the boundary layer. It can be confirmed if the boundary layer is being sufficiently covered in the solution as the turbulent viscosity is maximum half way through it. The first cell should be placed around $y^+ = 1$ [52].

3.5.5 Other CFD concepts

During the CFD process, especially when establishing the simulation strategy in Ansys Fluent, there are several important concepts to consider [52]:

- **Convective Fluxes** - In the realm of CFD, convective fluxes refer to the solution of the governing equations of conservation. Various schemes, such as Roe-FDS and

AUSM, are available, with the latter being more suitable for accurately resolving contact and shock discontinuities.

- **Pseudo Transient Under-Relaxation** - Under-relaxation scalars control the magnitude of the influence of previous iterations on the next solution. The pseudo transient method is a form of implicit under-relaxation, controlled by a pseudo time step. It establishes time scales for solving the flow properties.
- **Spatial Discretization** - Upwind schemes are used to determine the face values of a particular cell by interpolating the convective values at its center. The first-order upwind scheme assumes that the cell-center field variable is the average within the cell, giving each face the same value as the center of the upstream cell. The second-order upwind scheme is more accurate, as it sets gradients across each cell through a Taylor series expansion of the cell-centered solution.

Chapter 4

Methodology

In this Chapter, all the justifications leading to the results obtained for the contour design and respective numerical analyses are presented, explained, and discussed.

4.1 Contour Design

The contour is generated through the implementation of a simplified version of the MOC using the high-level programming language Python. The simplified model will be explained, and its choice justified, as well as the reasons behind choosing Python as the programming language.

4.1.1 The Simplified Method

H. Greer [36] developed a method for rapidly designing an aerospike nozzle contour using the centered expansion fan and geometry relations that relate streamlines with solid surfaces. Basically, this method involves drawing a specific streamline that will serve as the contour of the spike.

The first assumption to implement this simplified method (and often also assumed in traditional MOC) is that at the throat, the flow is sonic in a straight line and not a curved line.

As seen in Figure 4.1, it must also be assumed that the flow expands solely due to the centered expansion fan on lip A. Mach lines, which are characteristic lines, will expand and straighten the flow so that the desired exit MN is achieved with full parallelism to the plug centerline.

The last assumption, more related to the design, is that if the flow is desired to be parallel to the centerline at the exit, the flow at the throat must be incident with an angle equal to the Prandtl-Meyer angle of the chosen exit MN.

G. Angelino [37] took Greer's work and developed an even simpler method where the contour points are calculated discreetly, with an improved accuracy expected. To do so, for an interval of MN from 1 to the desired exit MN, the length of the respective Mach line from lip A until it meets the streamline that passes through lip B is calculated, as well as the inclination angle in relation to the horizontal.

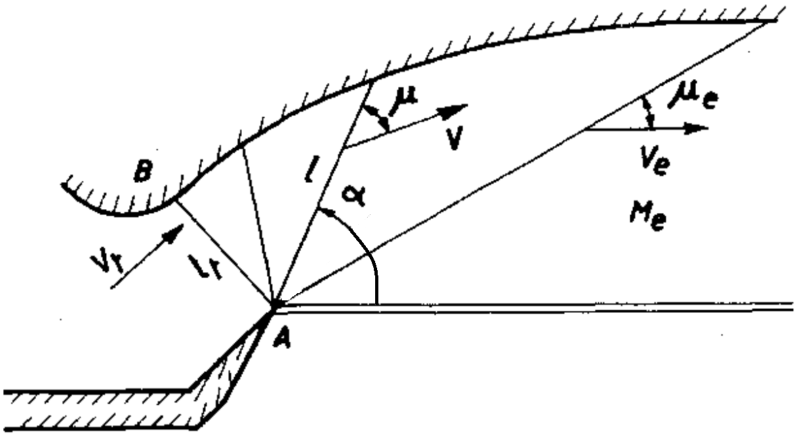

Figure 4.1: Sketch of the centered expansion fan of an aerospike [37]

Angelino's method has two steps for each MN to determine the position of the corresponding contouring point: calculating the distance from lip A to the contour streamline and the respective inclination. The length of such a line for a given MN can be obtained in a dimensionless value by the throat length, according to Equation 4.1, which relates the area of the throat with the area crossed by the velocity timeline that has that given MN. It can be further simplified into Equation 4.2, with $\varepsilon(M)$ being tgiven by Equation 3.28 and λ such dimensionless length. Lastly, the inclination is given in Equation 4.3, which is easily obtained with geometric relations.

$$\frac{l_{line}}{l_t} = \frac{A}{\sin\mu}\frac{1}{A_t} \quad (4.1)$$

$$\lambda(M) = M \times \varepsilon(M) \quad (4.2)$$

$$\alpha(M) = \nu(M_e) - \nu(M) + \mu(M) \quad (4.3)$$

4.1.2 Simplified Method Justification

The simplified method proposed by Angelino provides a nozzle contour that is pretty similar to the one obtained from the full MOC, as demonstrated in Figure 4.2. The produced contour only deviates slightly by the end of the nozzle, which can be truncated. Additionally, it is observed that the ratio between the pressure experienced by the flow and the stagnation pressure is quite coincident, with the bigger deviations happening at the end of the spike, which in many designs can be truncated.

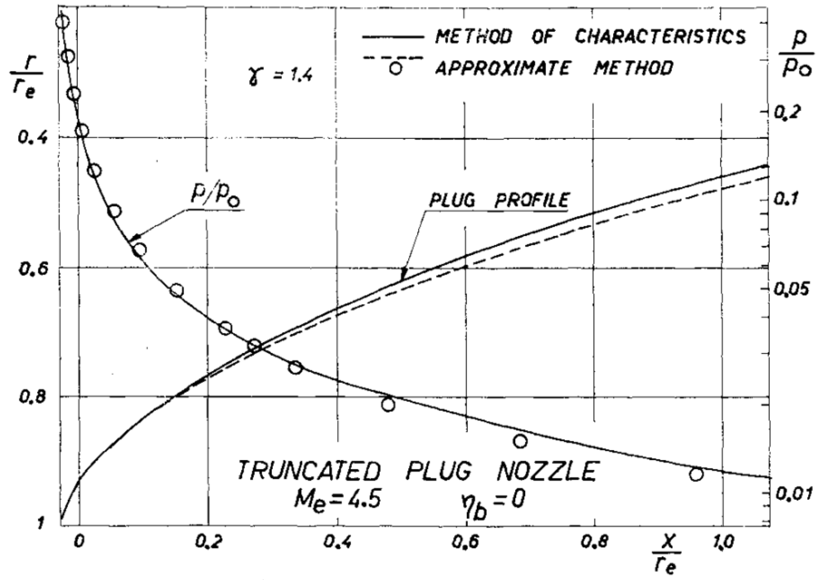

Figure 4.2: Comparison of approximate and exact solutions in linear aerospike nozzle design [37]

Nonetheless, Angelino simplified method calculates discreet points that need to be united. More complex methods, such as considering the points immediately after the throat are part of a circumference, don't produce much different contours then just interpolating all the points. In Reference [53] not only this is proven as also it is concluded Angelino's simplified method agrees with the results from more complex commercial numerical analyses tools and hot fire test experiments.

More examples of the usage of this simplified method are found in References [54], [55] and [56].

Therefore, for the scope of the present dissertation, this simplified method seems appropriate. Moreover, considering a large number of characteristic lines will lead to a more accurate contour, even without considering complex methods of interpolating the resulting points.

4.1.3 Python Considerations

Python is one of the most widely used programming languages in aerospace engineering, including by NASA, especially in non-safety critical systems [57]. It is characterized as a high-level programming language that emphasizes readability and encourages the creation of open-source libraries. Additionally, Python is free to use and does not require a compilation step, which accelerates the edit-test-debug cycle and prevents segmentation faults from incorrect user usage through the use of exceptions.

These qualities make Python a popular choice for Rapid Application Development and gluing existing code components. One of Python's biggest advantages is its similarity to the English language, which makes it easy to code and allows for increased attention to the result. As a high-level language, it also allows users to focus on programming without having to consider hard computer science concepts like architecture and memory management.

However, Python's interpreter nature means that it executes code line by line, which can slow down program execution and make it more time-consuming. Additionally, Python may not be suitable for memory-intensive tasks [58].

Nonetheless, Python is a good choice for implementing the simplified Angelino's method, as it strikes a balance between ease of implementation and loss of memory control and increased running time. Furthermore, Python's open-source libraries such as NumPy, pandas, and Matplotlib provide significant assistance in the proposed work.

4.1.4 Simplified Method Algorithm

The code used to compute the full aerospike nozzle contour can be found in Appendix A, with detailed comments provided for each step. The program begins by prompting the user to input the desired exit MN, the number of Mach lines to be considered, and the constant adiabatic index of the flow.

The program then sets the MN for each mach line and calculates its dimensionless length and angle using the equations previously mentioned. Subsequently, it draws the full contour and exports the computed contour points to an Excel file, along with the corresponding pressure ratio between the chamber (stagnation) and the ambient.

The output file provides the contour's coordinates for a throat gap of 1 mm, so they must be multiplied by the desired throat gap.

4.2 Numerical Studies

The contour designed with the Python code is imported and integrated into a control volume. The control volume is then meshed, and the flow is simulated, considering both inviscid and turbulent models.

The specific impulse, defined in Equation 2.2 is chosen as the performance parameter.

4.2.1 Control Volume Geometry

The goal of the control volume's geometry was to enable the capture of the full expansion of the exhaust flow while also allowing for the placement of a wall boundary at the farfield.

This positioning ensures that the expansive plume effects can be neglected at the farfield wall. To achieve this, the geometric dimensions are associated with the throat distance from the spike's central line (H) and its length (L).

The geometry was created using Ansys's SpaiceClaim and it can be seen in Figure 4.3.

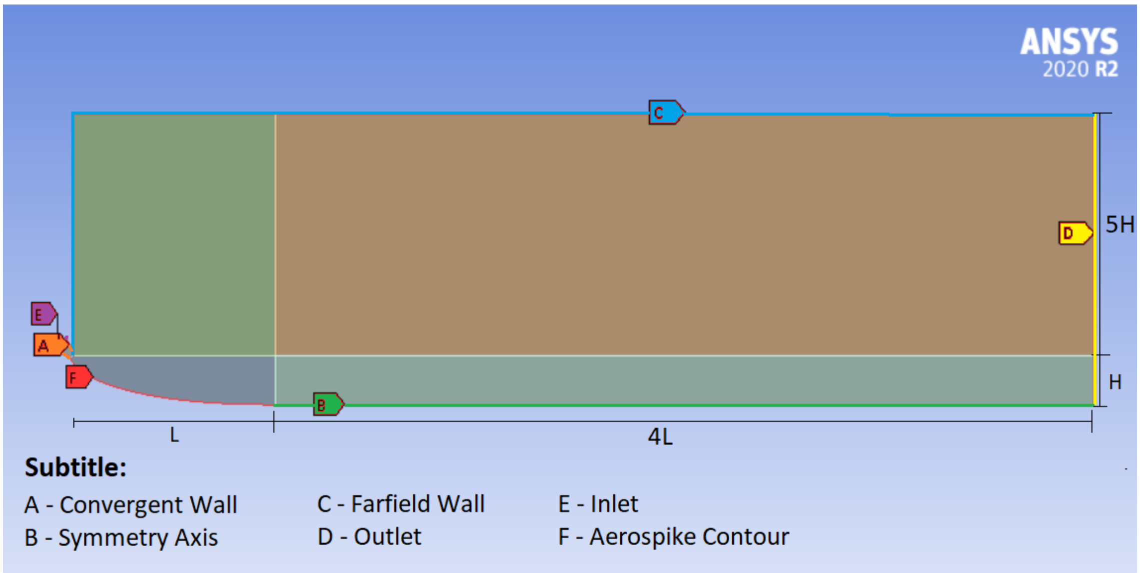

Figure 4.3: Control volume geometry and nomenclature of its surfaces

No deep analysis was conducted during the design of the convergent section, as its primary purpose is to accelerate the flow from an almost stagnation condition (MN of 0.21, in the defined geometry depicted in Figure 4.4). The convergent section is designed to achieve a choked, sonic flow at the throat, while maintaining the proper incidence. It bears resemblance to the one presented in Reference [59], but has been adapted for a linear plug configuration, being inserted relative to the contour in a similar manner as described in Reference [35].

4.2.2 Mesh

Once the geometry is established, it becomes crucial to achieve a high-quality mesh in order to ensure accurate simulations. A high-quality mesh is essential as it captures the gradients of the most relevant properties effectively, facilitating fast convergence.

In the specific case of the present dissertation, a more refined mesh is required near the aerospike contour to accurately model flow expansion. Additionally, to capture turbulence effects and maintain an appropriate y^+ value, a bias factor is applied to ensure that the mesh is more refined in the vicinity of the contour, allowing the proper running of the wall functions.

The mesh of the critical region can be observed in Figure 4.5. To ensure that the face meshing of the light blue region functions correctly, the walls of the convergent section,

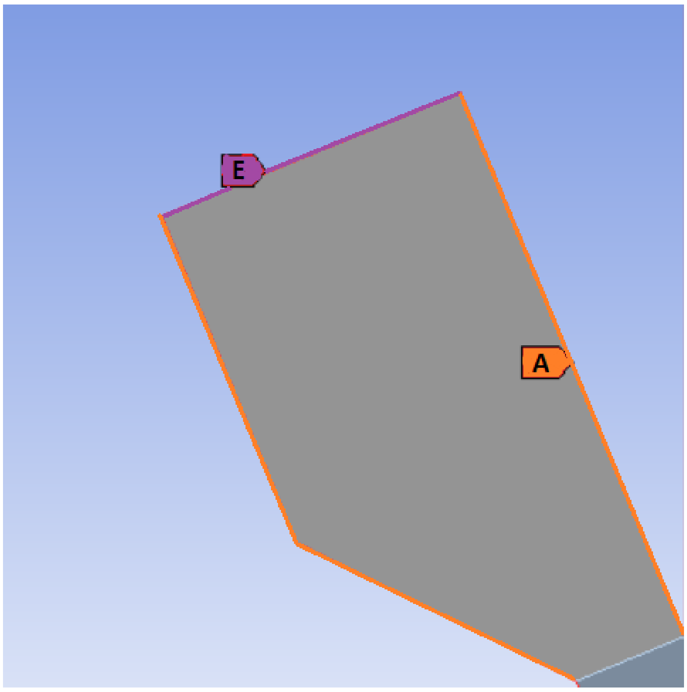

Figure 4.4: Convergent geometry close-up

aerospike contour, and the frontier region (which corresponds to the throat) are assigned a soft behavior. This approach results in an excessively refined grid in the convergent section, representing a necessary trade-off to ensure proper meshing of the light blue zone.

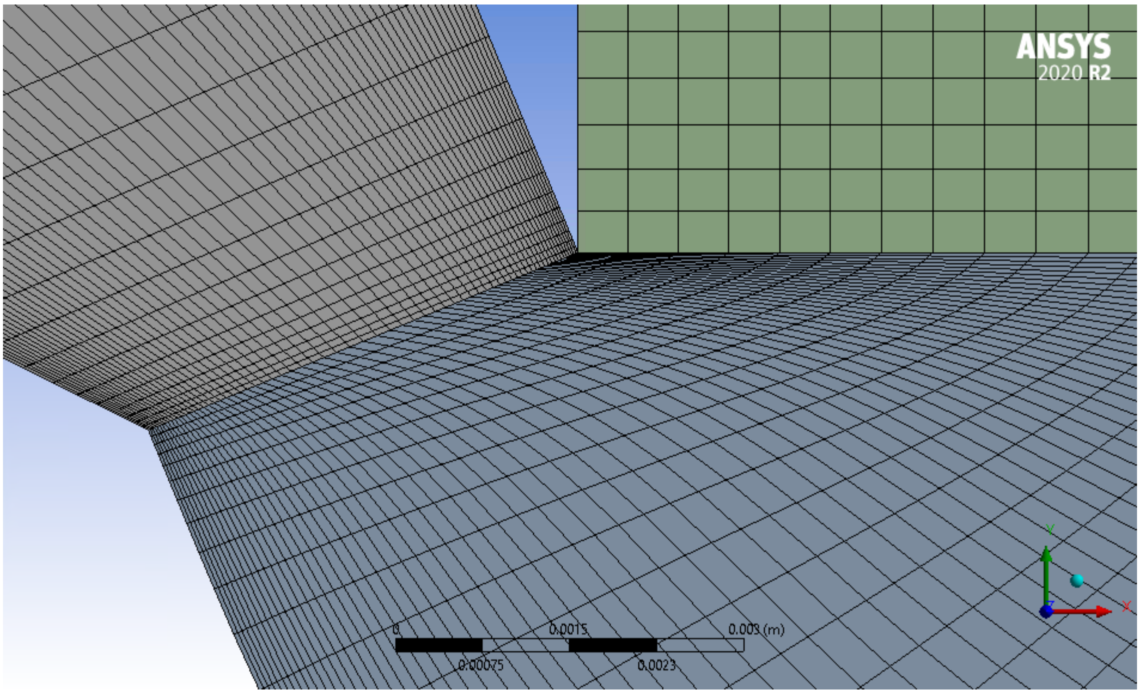

Figure 4.5: Mesh close-up

The remaining edges of the mesh are sized using a suitable bias and assigned a hard behavior to maintain coherence with the light blue region. This approach ensures that the mesh is more sparse in the right upper corner where minimal flow activity is anticipated. By adapting the mesh density according to the expected flow behavior, an optimized mesh is achieved.

To ensure a smooth manual mesh connection between different surfaces, the common edge between them is assigned the same sizing parameters. This approach enables a seamless transition node by node during the manual meshing process. The resulting final mesh, utilized for the numerical analysis, is displayed in Figure 4.6.

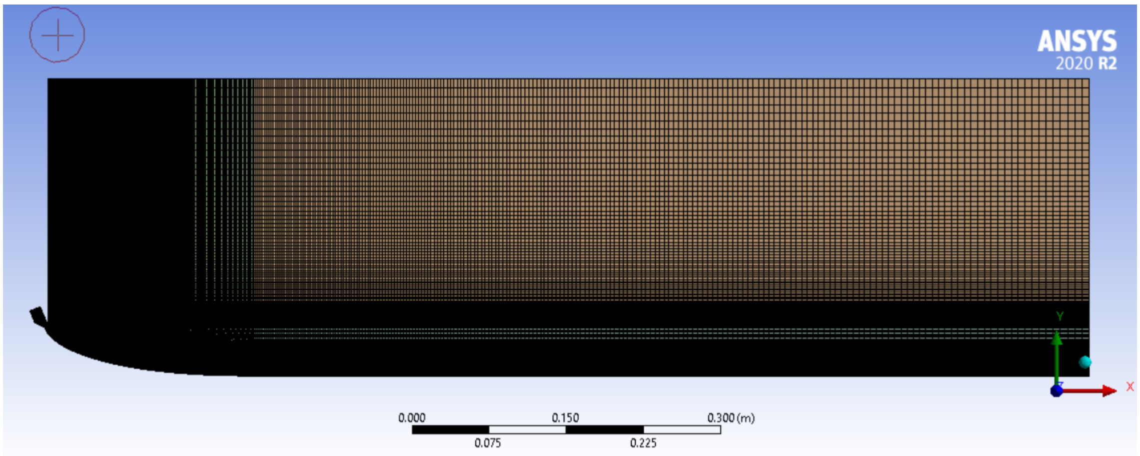

Figure 4.6: Mesh

To conduct the mesh independence study, the number of divisions for each edge is increased by factors of 1.25 and 1.5. The resulting number of nodes for each mesh configuration are summarized in Table 4.1.

Table 4.1: Mesh number of nodes for independence study

	Mesh x1	**Mesh x1.25**	**Mesh x1.5**
Number of Nodes	75759	118344	169084

4.2.3 Fluent

Table 4.2 presents a summary of the approaches and options implemented to acquire the results showcased in Chapter 5. All the options not referred are left at default values. A user-defined field variable is set so the thrust generated by Equation 2.5 can later be integrated and easily obtained.

Table 4.2: Methods and controls implemented in Fluent

<table>
<tr><th colspan="2"></th><th>Inviscid</th><th>Turbulent</th></tr>
<tr><td rowspan="3">Solver</td><td>Type</td><td colspan="2">Density-Based</td></tr>
<tr><td>Time</td><td colspan="2">Steady</td></tr>
<tr><td>Space</td><td colspan="2">Planar</td></tr>
<tr><td rowspan="3">Models</td><td>Energy</td><td colspan="2">On</td></tr>
<tr><td>Viscous</td><td>Inviscid</td><td>Realizable k-ε</td></tr>
<tr><td>Near-Wall Treatment</td><td>-</td><td>Enhanced Wall Treatment</td></tr>
<tr><td rowspan="2">Materials (air)</td><td>Density</td><td colspan="2">ideal-gas</td></tr>
<tr><td>Viscosity</td><td colspan="2">Sutherland (Two Coefficient Method)</td></tr>
<tr><td rowspan="7">Boundary Conditions</td><td>Convergent</td><td colspan="2">wall</td></tr>
<tr><td>Symmetry Axis</td><td colspan="2">symmetry</td></tr>
<tr><td>Falfield</td><td colspan="2">wall</td></tr>
<tr><td>Outlet</td><td colspan="2">pressure-outlet</td></tr>
<tr><td>Inlet</td><td colspan="2">pressure-inlet</td></tr>
<tr><td>Aerospike Contour</td><td colspan="2">wall</td></tr>
<tr><td>Operating Conditions</td><td colspan="2">0 Pa (Operating Pressure)</td></tr>
<tr><td colspan="2">Reference Values</td><td colspan="2">Computed from inlet</td></tr>
<tr><td rowspan="4">Methods</td><td>Flux Type</td><td colspan="2">AUSM</td></tr>
<tr><td>Spatial Discretization</td><td>First Order Upwind</td><td>Second Order Upwind</td></tr>
<tr><td>Options</td><td colspan="2">Pseudo Transient</td></tr>
<tr><td>Time Scale Factor</td><td colspan="2">between 0.0005 and 0.003</td></tr>
<tr><td colspan="2">Convergence Criteria</td><td colspan="2">Residuals below 5×10^{-5}
(5×10^{-4} for continuity)</td></tr>
<tr><td colspan="2">Initialization</td><td colspan="2">Hybrid</td></tr>
</table>

4.3 Parameters of the Study

To facilitate the contour and simulation validation, the design parameters are those of Reference [60].

4.3.1 Python Inputs

The Python code asks the user for three inputs, with the choosen values summarized in Table 4.3.

Table 4.3: Parameters for Python code

	Input Value
Mach Number	4.16
Addiabatic Index	1.4
Number of Lines	100

4.3.2 Fluent Parameters

The operating conditions inserted in Fluent are summarized in Table 4.4. To be noted that the values already have into account the PR calculated by the Python code, particularly in predicting the operating condition accordingly with the outlet pressure.

Table 4.4: Parameters for Fluent Boundaries

		Input Value
Inlet	Gauge Total Pressure	2068427 Pa
	Supersonic/Initial Gauge Pressure	2002837 Pa
	Total Temperature	3200 K
Outlet	Gauge Pressure	Overexpanded - 101325 Pa Design - 11032 Pa Underexpanded - 7171 Pa and 100 Pa
	Backflow Total Temperature	Overexpanded - 288 K Design - 217 K Underexpanded - 217 K and 270 K

Chapter 5

Results and Discussion

This chapter presents the aerospike's designed contour and discusses the results obtained from its operational simulation at various altitudes, considering different viscous simulation options, as so the simulation validation by comparison to published literature.

5.1 Python outputs and Contour Validation

By inserting the inputs mentioned in Subsection 4.3.1, the designed contour depicted in Figure 5.1 is obtained. The corresponding data and dimensions of the aerospike are provided in Table 5.1. It is important to note that the dimensions of the aerospike already takes into consideration a throat gap length of 4.005 mm.

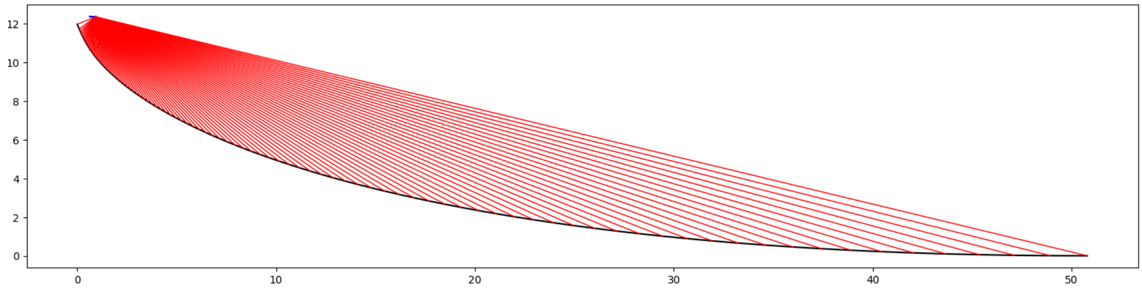

Figure 5.1: Aerospike contour designed with Angelino's method

Table 5.1: Outputs from the Python code

	Output (for a 4.005 mm throat gap)
Throat Angle (θ_t)	67.838 °
Pressure Ratio (PR)	187.52
Heigh (H)	49.46 mm
Length (L)	203.45 mm

The geometric dimensions of the aerospike coincide with those of Reference [60] ($H = 2$ in and $L = 8$ in), and the contour of the wall, as shown in Figure 5.2, also exhibits close resemblance. This similarities confirm the accuracy of the Python code used to generate the contour, as it produces the same results as the consulted bibliography.

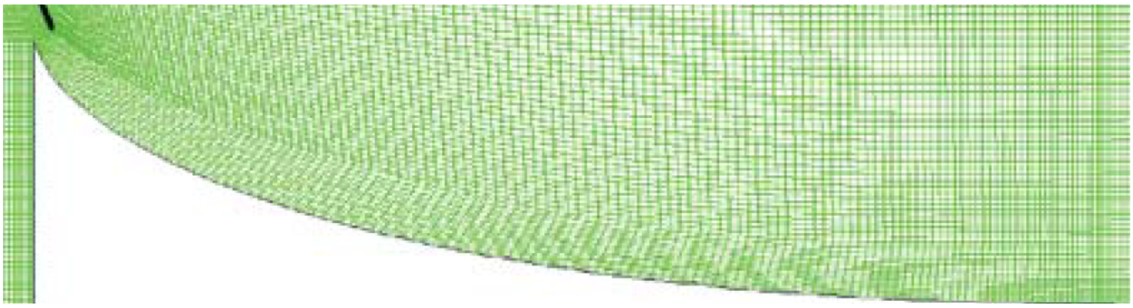

Figure 5.2: Aerospike's contour from Reference [60]

5.2 Numerical Results

This section presents the the post-processing of the CFD results obtained from the implementation of the study proposed in Section 4.2, using the parameters described in Subsection 4.3.2.

Subsections 5.2.1, 5.2.2, 5.2.3 and 5.2.4 will present Figures displaying the contour of the most relevant flow properties for both the inviscid and turbulent viscous models. These Figures will specifically focus on the aerospike operating at the design PR. Additionally, Figures of the MN, and other properties contours, for the operation at other PR values, and for the two different meshes used in the inviscid case at the design PR, will also be showcased. The purpose is to provide a comprehensive visualization of the flow properties, emphasizing the behavior of the aerospike under different operating conditions and perform a mesh independence study. The inviscid properties' contours will be compared to those of Reference [60] so the Fluent's implementation can be validated.

In Subsection 5.2.5, the essential flow properties required to evaluate the performance of the nozzle (if a 1 meter width is assumed) are summarized. These properties include the thrust produced, which is the sum of Equations 2.1 and 2.5, as well as the specific impulse calculated according to Equation 2.2. After summarizing the flow properties at the exit, in Subsection 5.2.6 an overall assessment of the nozzle's performance can be obtained by comparing the two simulation options for viscosity and considering how altitude affects performance.

5.2.1 Inviscid Simulation at Design Altitude

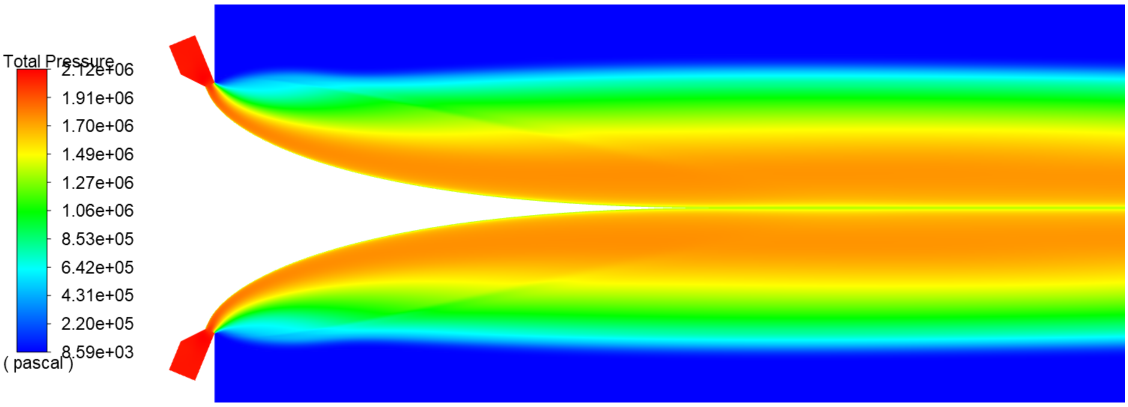

Figure 5.3: Total pressure (Pa) contour for inviscid model operating at a 188 PR

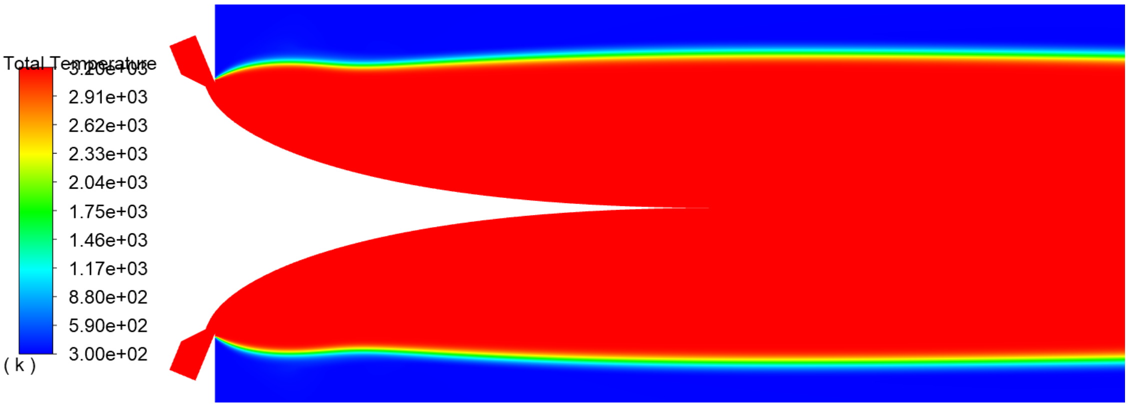

Figure 5.4: Total temperature (K) contour for inviscid model operating at a 188 PR

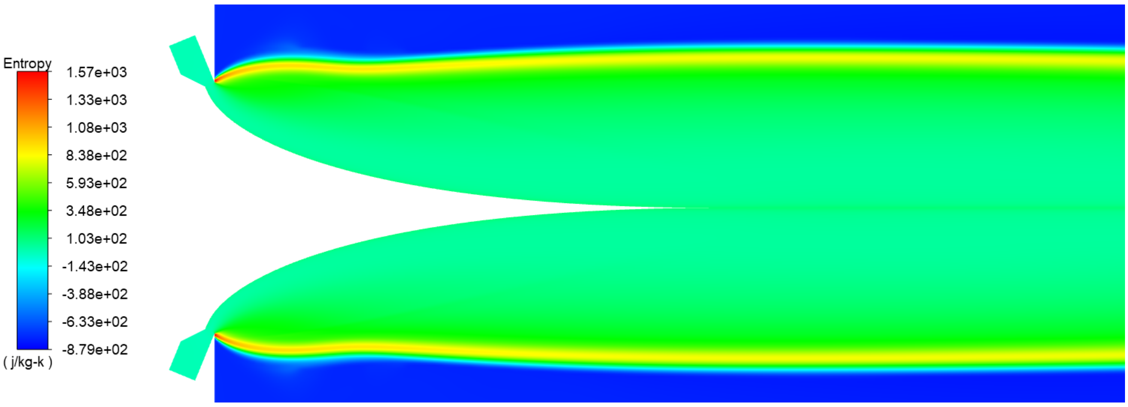

Figure 5.5: Entropy (J/kg.K) contour for inviscid model operating at a 188 PR

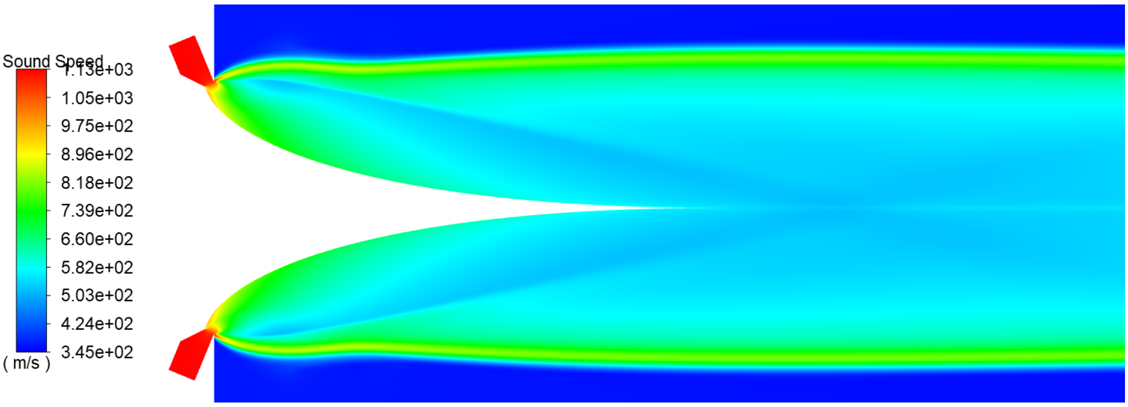

Figure 5.6: Sound speed (m/s) contour for inviscid model operating at a 188 PR

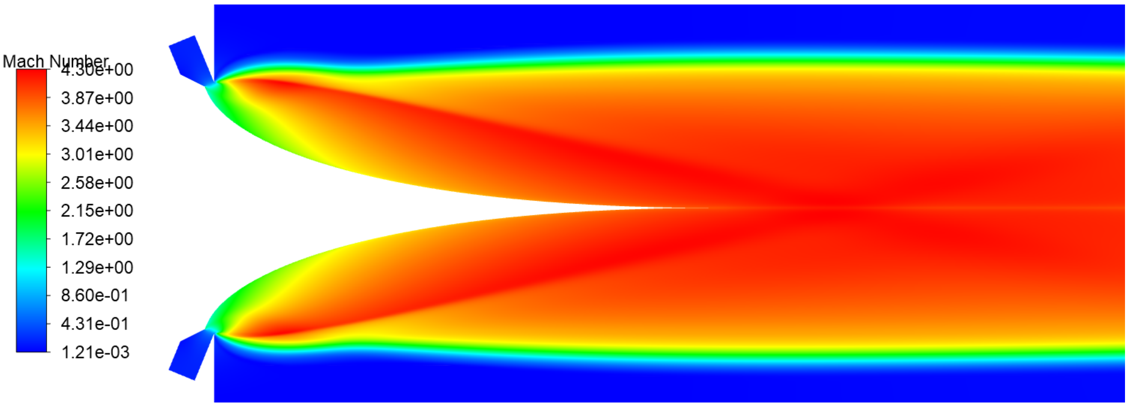

Figure 5.7: Mach number contour for inviscid model operating at a 188 PR

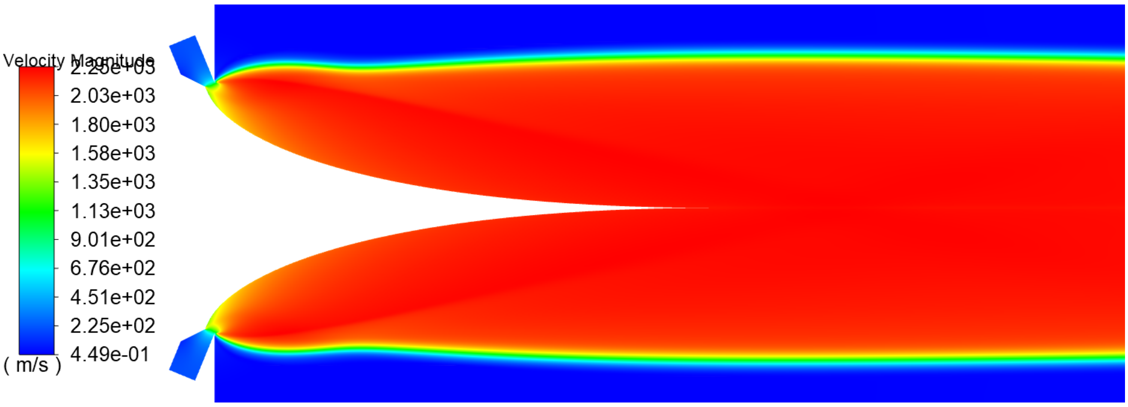

Figure 5.8: Velocity (m/s) contour for inviscid model operating at a 188 PR

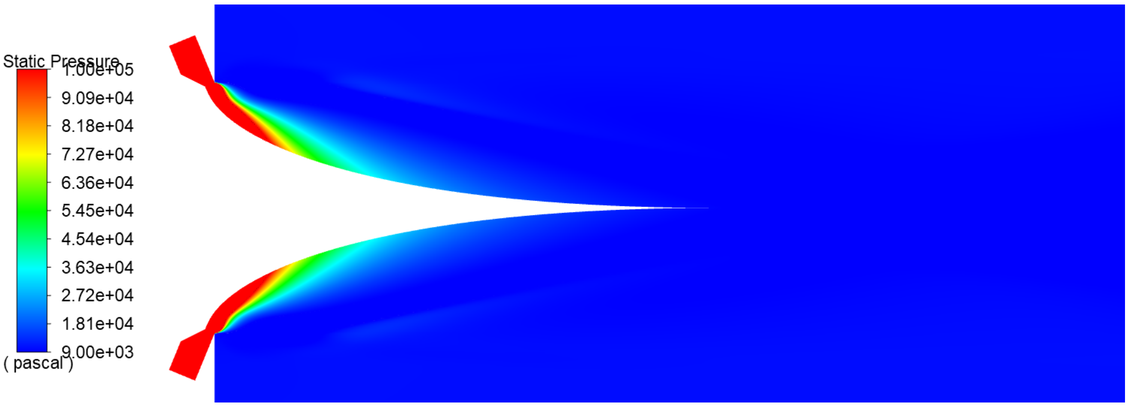

Figure 5.9: Static pressure (Pa) contour for inviscid model operating at a 188 PR

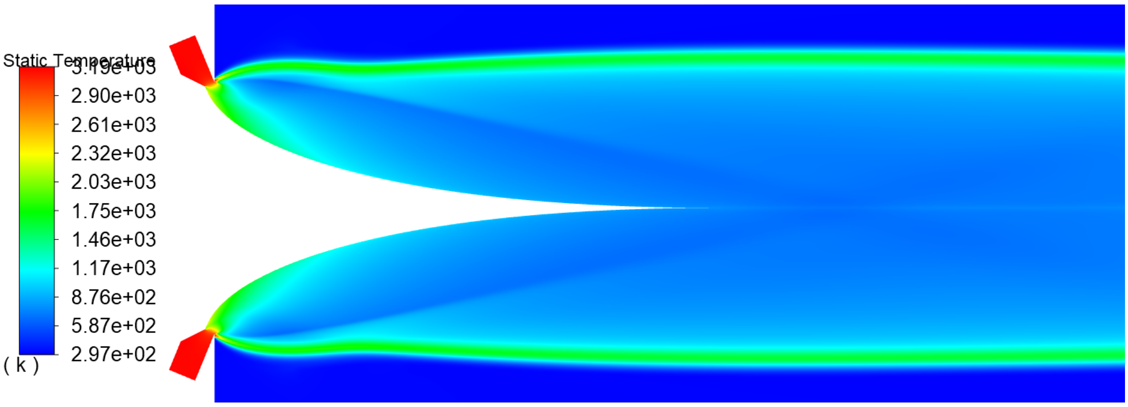

Figure 5.10: Static temperature (K) contour for inviscid model operating at a 188 PR

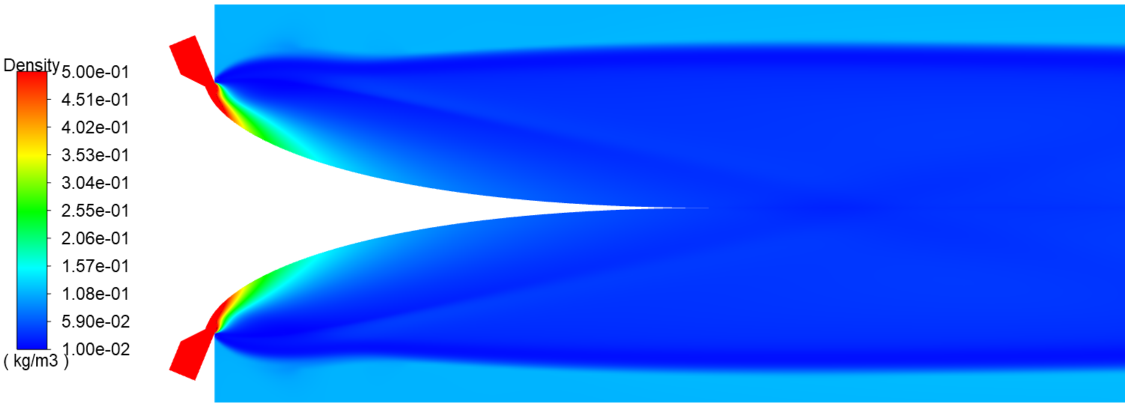

Figure 5.11: Density (kg/m^3) contour for inviscid model operating at a 188 PR

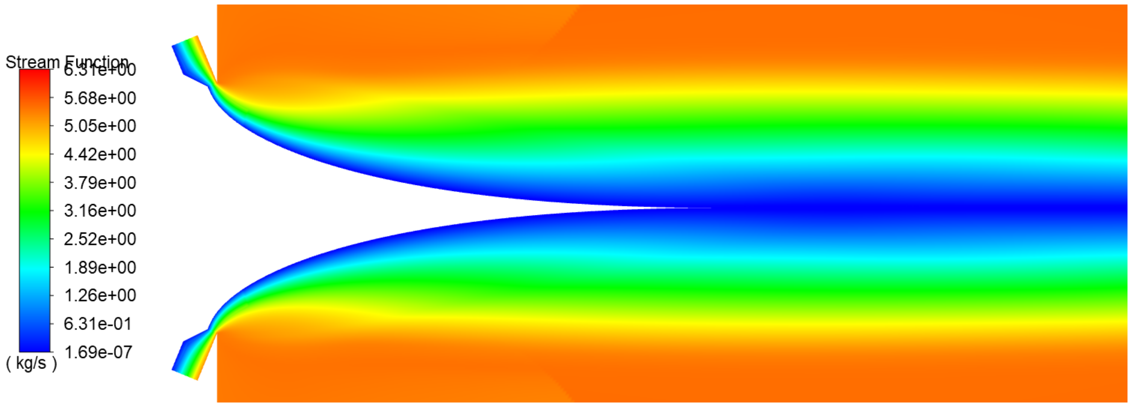

Figure 5.12: Stream function (kg/s) contour for inviscid model operating at a 188 PR

Figure 5.4 provides insight into an established flow with minimal isentropic losses. It demonstrates that the total temperature of the chamber is maintained consistently throughout the exhaust plume, indicating a barrier between the exhaust plume and the atmosphere. This barrier is observed to begin at the upper lip of the throat as it represents heat transfer between the exit flow and its surroundings.

The interaction between the plume and the atmosphere is further evident in Figure 5.5. The region at the frontier of the plume experiences significant entropy production, particularly after the sharp geometry of the upper lip of the throat. These isentropic losses are observed through a reduction in the total pressure, as depicted in Figure 5.3. The increase in entropy and the corresponding reduction in total pressure indicate that the flow is becoming more disordered and less energetic as it interacts with the surrounding atmosphere.

As expected, according to Equation 3.19, the speed of sound and static temperature contours shown in Figures 5.6 and 5.10, respectively, are very similar. This similarity highlights a shock wave that originates from the top lip of the throat and extends to a little after the end of the aerospike.

The flow structure mentioned above can also be observed in Figure 5.7. It is evident that the flow still expands beyond the last theoretical Mach line and travels a short distance before encountering a small oblique shock. This shock creates variations in the flow's density, as depicted in Figure 5.11. Nonetheless, it should be noted that this shock is weak and nearly imperceptible in the velocity and static pressure contours shown in Figures 5.8 and 5.9, respectively.

Looking into more detail at the exit values present in Table 5.2, it is observed that the exit MN is lower than the expected value of 4.16. This deviation can be explained by the presence of a locally higher temperature compared to an ideal quasi one-dimensional analysis. This higher temperature leads to a less discrepant exit velocity.

Figure 5.12 illustrates the stream function values, emphasizing the expected behavior of the streamlines, without any mass changes between them.

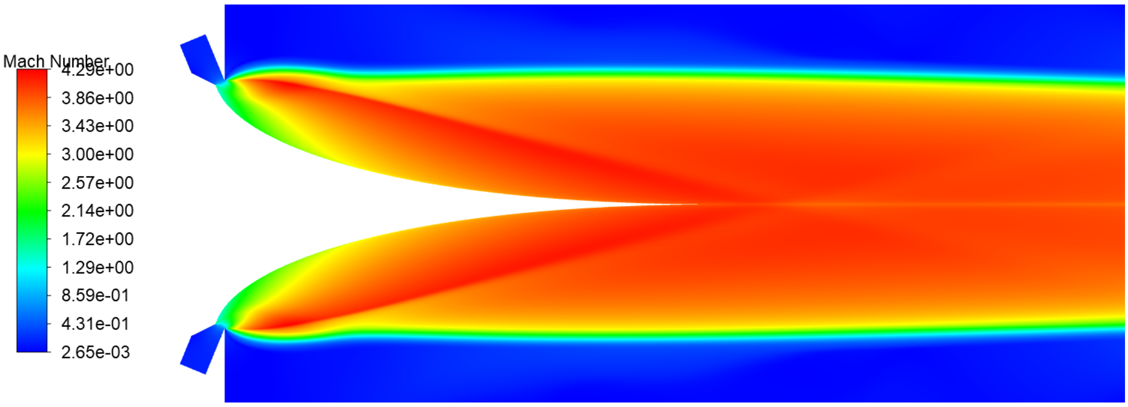

Figure 5.13: Mach number contour at x1.25 mesh for inviscid model operating at a 188 PR

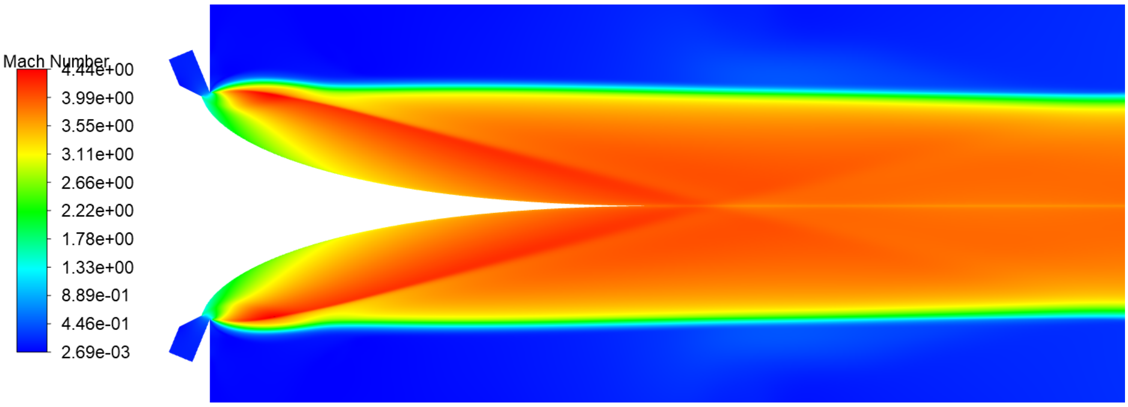

Figure 5.14: Mach number contour at x1.50 mesh for inviscid model operating at a 188 PR

Comparing the MN contours in Figures 5.7, 5.13, and 5.14, it can be inferred that regardless of the mesh density, the flow exhibits the same features. There is expansion until a little further from the theoretical last Mach line, followed by a weak shock. Considering the property values at the exit Mach line and the performance stated in Table 5.2, it can be concluded that the standard mesh used is valid, as increasing its density does not produce significantly different results.

The properties contours shown in Figures 5.3 to 5.12 exhibit a close resemblance to those presented in Reference [60], depicted in Figure 5.15. These contours indicate similar flow behavior between the two studies. In particular, Figures 5.15e), 5.15f), and 5.15h) also display the presence of an oblique shock after the exit. The exit MN is even smaller than the expected value of 4.16, while the exit static temperature is higher. Furthermore, the exit velocity in the Reference's case is higher compared to the present study but it has a lower mass flux. These differences in flow parameters contribute to a slightly lower specific impulse in the case of Reference [60].

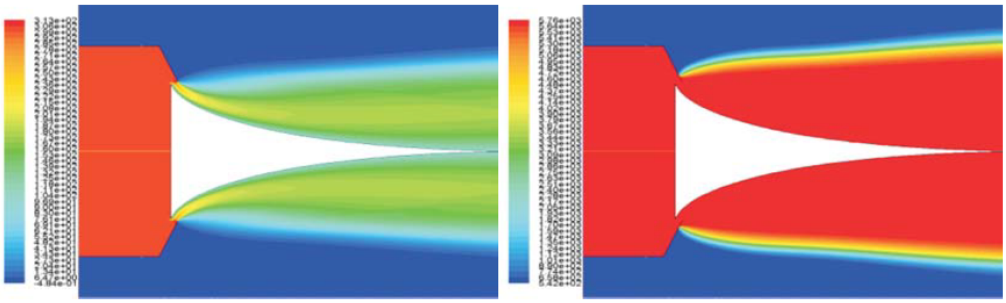

a) Total Pressure (psi) **b)** Total Temperature (R)

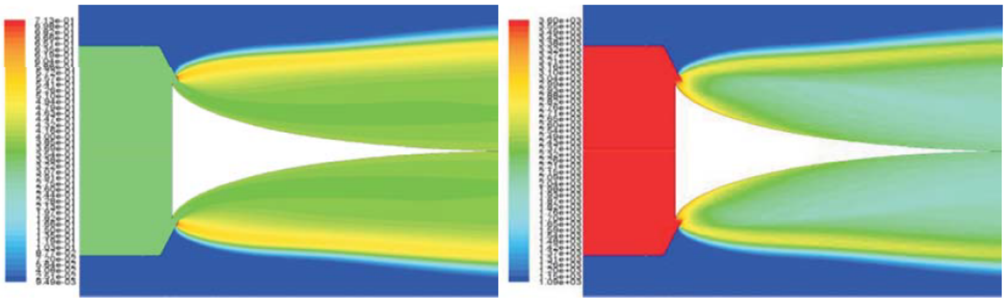

e) Entropy (btu/lb$_m$.R) **d)** Speed of Sound (ft/s)

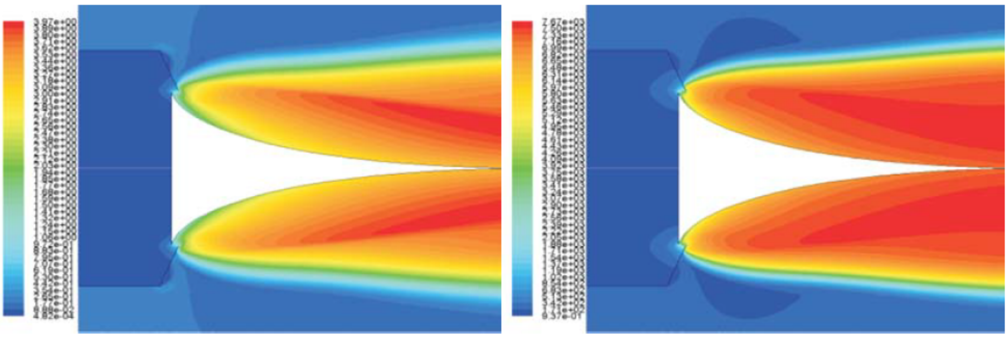

e) Mach number **f)** Velocity (ft/s)

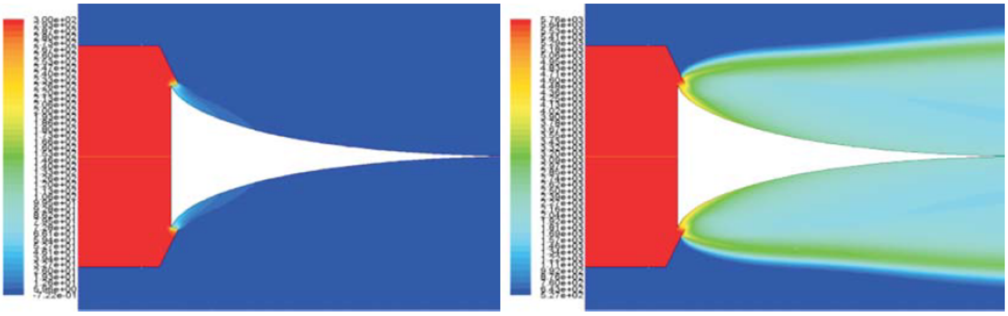

g) Pressure (psi) **h)** Temperature (R)

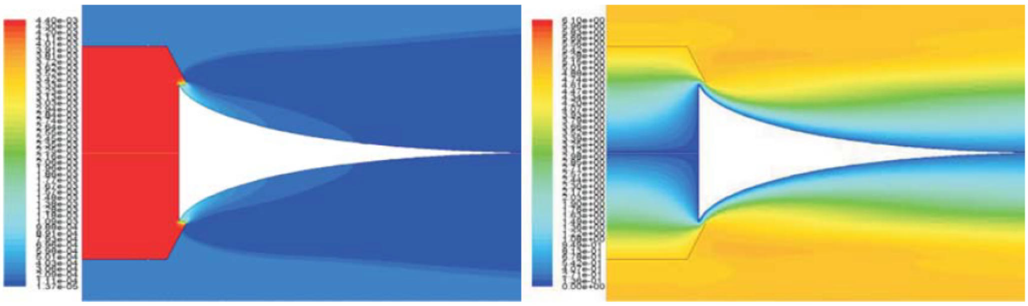

i) Density (slug/ft^3) **j)** Stream Function (kg/s)

Figure 5.15: Properties' Contours from Reference [60]

5.2.2 Other Inviscid Simulations for Several Operating Altitudes

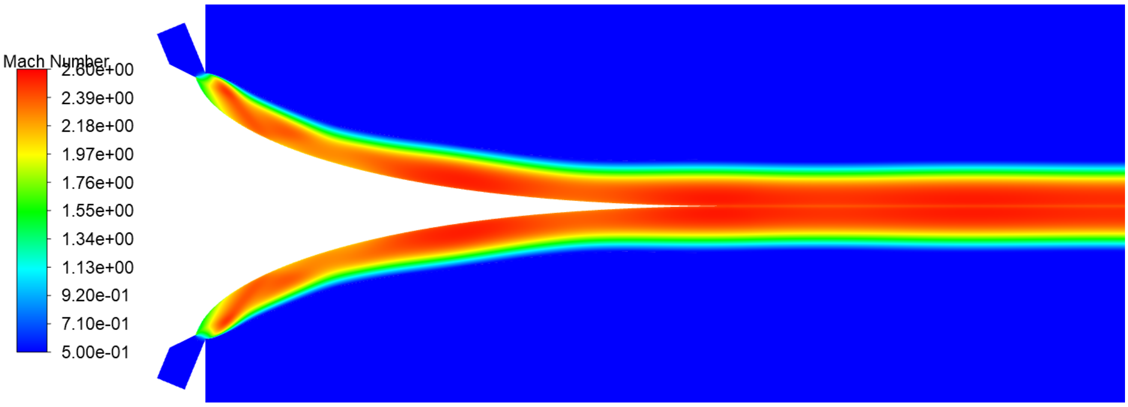

Figure 5.16: Mach number contour for inviscid model operating at a 20 PR

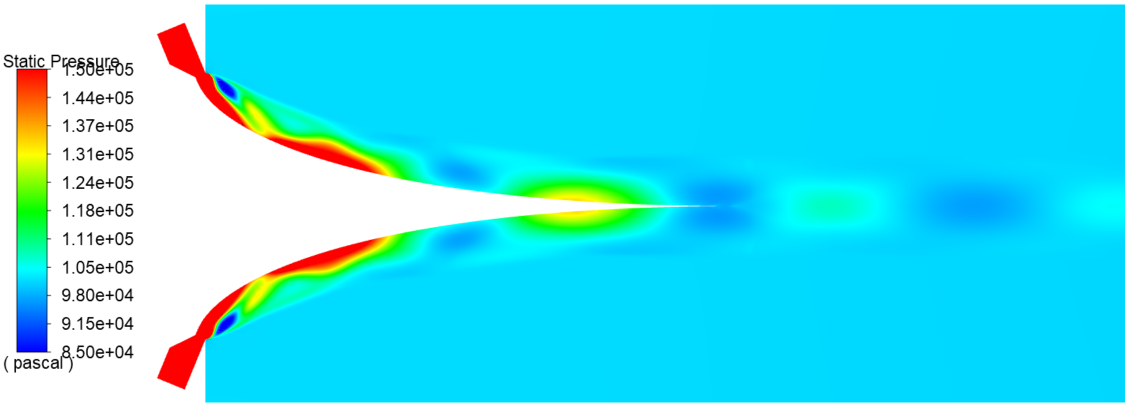

Figure 5.17: Static pressure (Pa) contour for inviscid model operating at a 20 PR

When the aerospike is operating at a PR corresponding to an ambient pressure at sea level, it behaves as expected, since the flow depicted in Figure 5.16 shows the exhaust plume is compressed against the spike's wall, typical in an overexpanding scenario.

Figure 5.17 illustrates the expansion and compression fans that enable the flow to remain attached to the nozzle and maintain its axiality. It must be noted that in the zones between compression and expansion fans, the flow should reach ambient pressure, being in reality higher. These regions are crucial for the flow to achieve a balanced state with the environment, and their absence means that the real behavior of the flow is not observed.

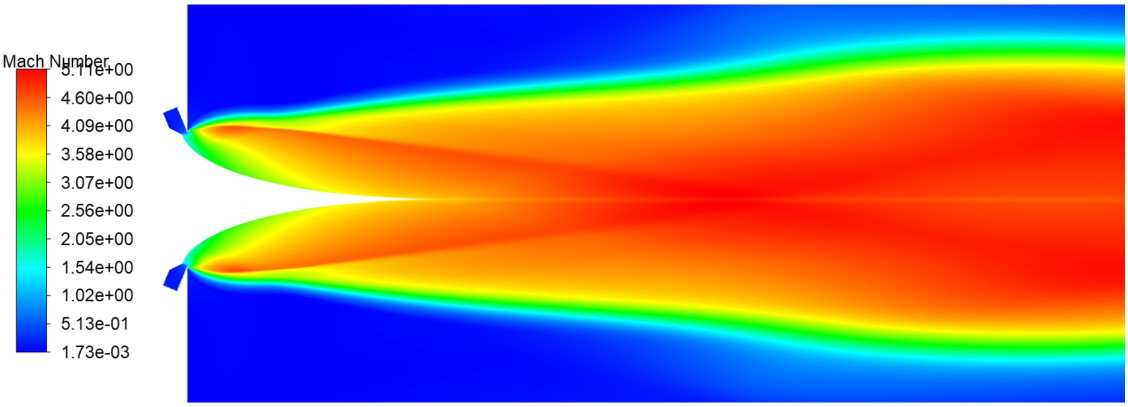

Figure 5.18: Mach number contour for inviscid model operating at a 288 PR

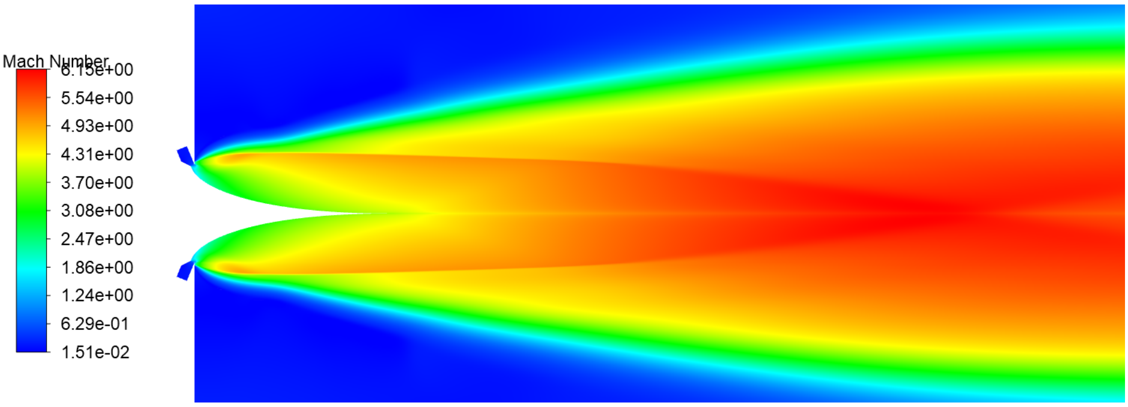

Figure 5.19: Mach number contour for inviscid model operating at a 20480 PR

At higher PR (compared to design conditions), the MN contours depicted in Figures 5.18 and 5.19 reveal evidence of underexpansion in the exhaust plume. The flow expands past the exit Mach line, resulting in zones with higher MN. Additionally, a pair of shock amd expanding fans becomes apparent in the flow.

As the ambient pressure decreases, it can be observed that the flow expands to even higher Mach numbers, and the location of the first shock moves further away from the aerospike. Anyhow, the exhaust plume doesn't get much wider, showcasing the first evidence of the aerospike's capability for altitude adaptation.

5.2.3 Turbulent Simulation at Design Altitude

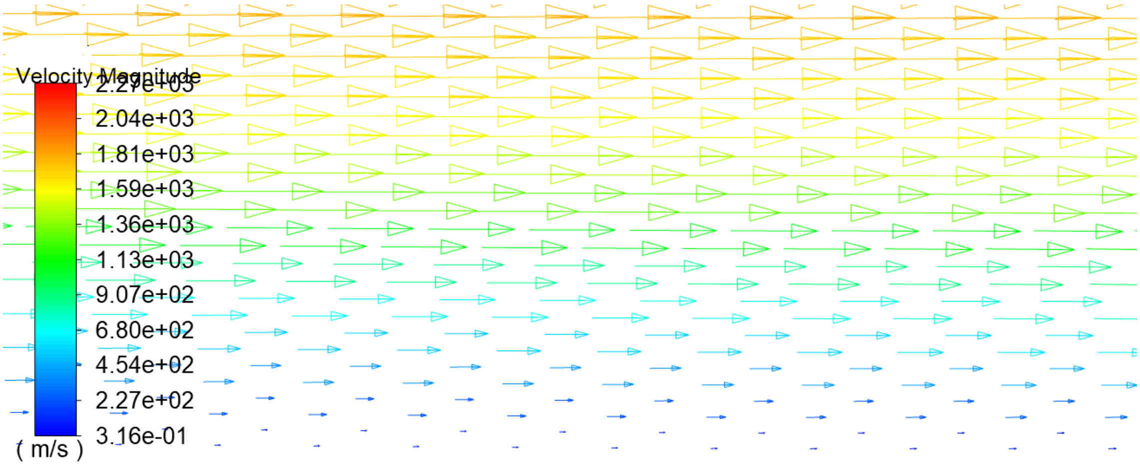

Figure 5.20: Velocity vectors near aerospike's wall for turbulent model operating at a 188 PR

Once the inviscid model is abandoned, the presence of the wall requires the consideration of the no-slip condition, which contributes to the turbulent effects. Modulating these effects correctly is an essential aspect of the turbulent simulation. Figure 5.20 shows that, near the wall, an abrupt reduction in velocity magnitude appears, indicating a stagnation zone due to the no-slip condition.

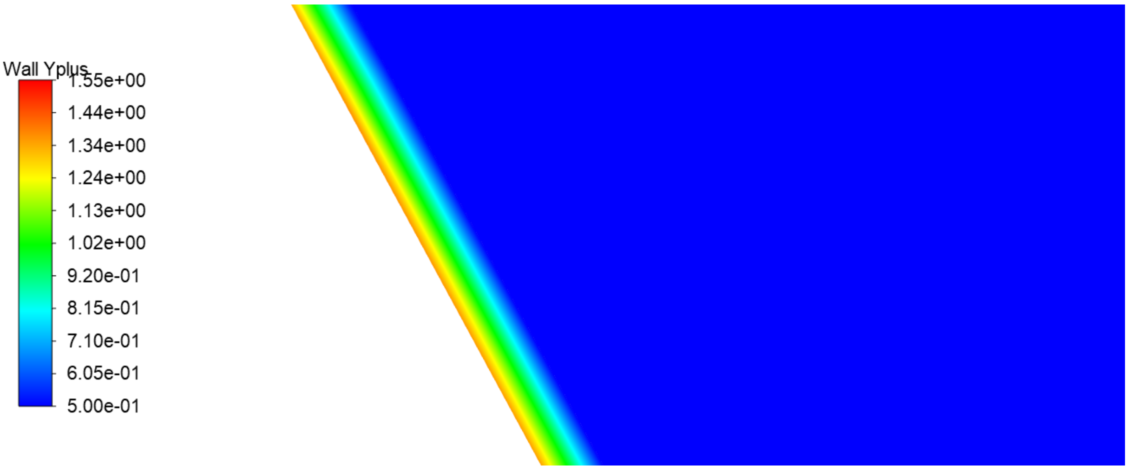

Figure 5.21: y^+ maximum values at aerospkie's wall for turbulent model operating at a 188 PR

The enhanced wall treatment, applied as the wall function to simulate the boundary layer, can only be utilized effectively if the mesh satisfies the condition of $y^+ < 5$. In Figure 5.21, it can be observed that the highest registered value of y^+ is 1.38, confirming that this was the best approach to simulate the boundary layer effects.

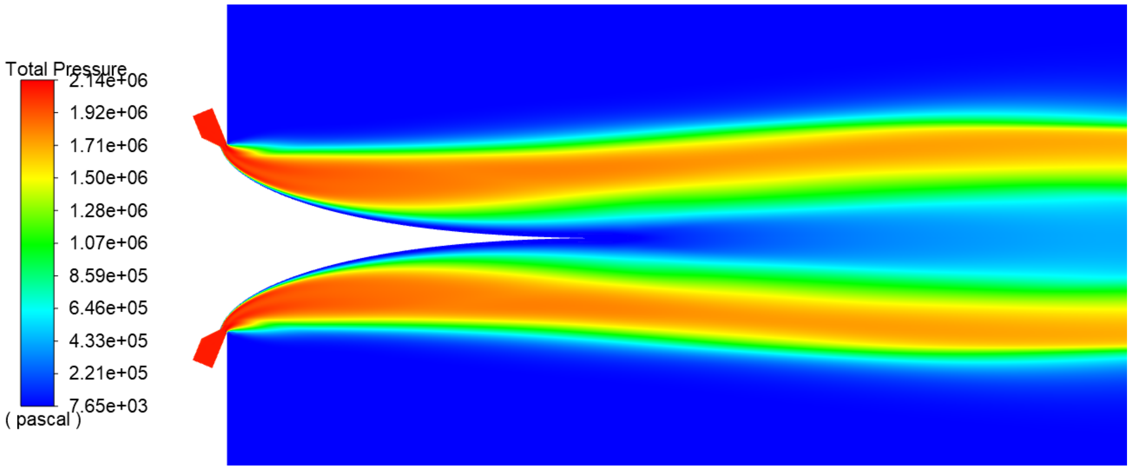

Figure 5.22: Total pressure (Pa) contour for turbulent model operating at a 188 PR

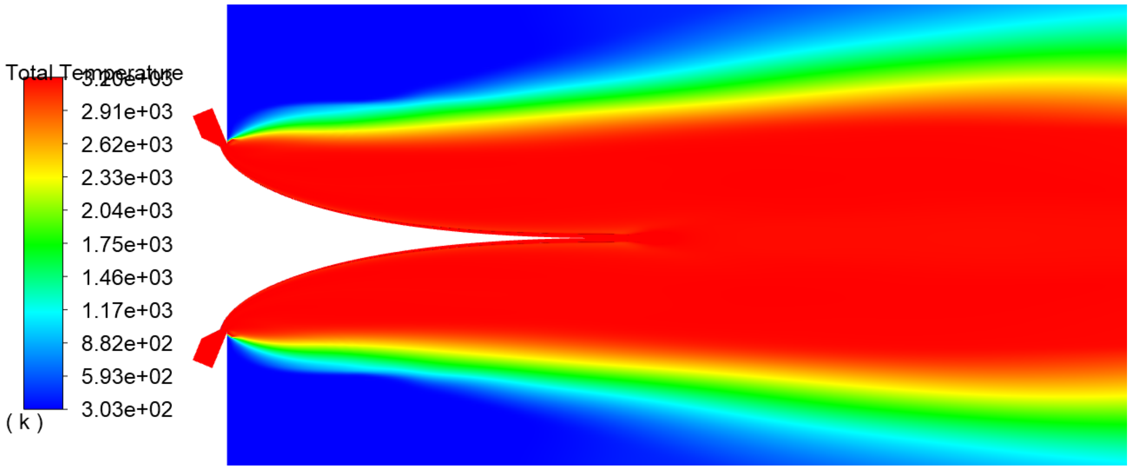

Figure 5.23: Total temperature (K) contour for turbulent model operating at a 188 PR (1)

The first evidence of the effects produced by the consideration of a turbulent model can be observed in Figure 5.23, specifically in the stagnation temperature contour. In comparison to the inviscid case, the boundary between the hot exhaust plume and the ambient is more gradual, indicating the high mixing capability of the turbulent flow. This mixing causes the temperature gradient to become less sharp as the two different fluids interact.

Figure 5.24 presents the same property on a different scale, revealing a second influence of the turbulent flow, which is the generation of heat due to friction within the boundary layer. The stagnation temperature value rises to more than 7000K, but this must be read with caution, as the simulation options may fail in such an extreme environment, where molecular dissociation effects should be taken into account. Additionally, it is important to note that the enhanced wall treatment may have limitations, particularly in modulating the energy equation. However, these limitations do not significantly impact the results, and the behavior exhibited by the aerospike in the simulation aligns with what is expected.

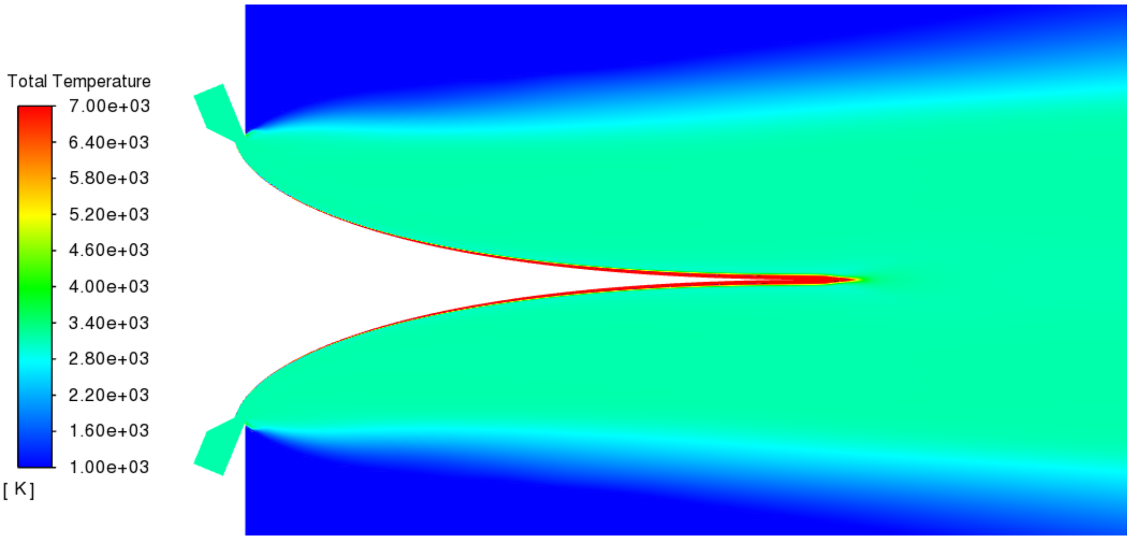

Figure 5.24: Total temperature (K) contour for turbulent model operating at a 188 PR (2)

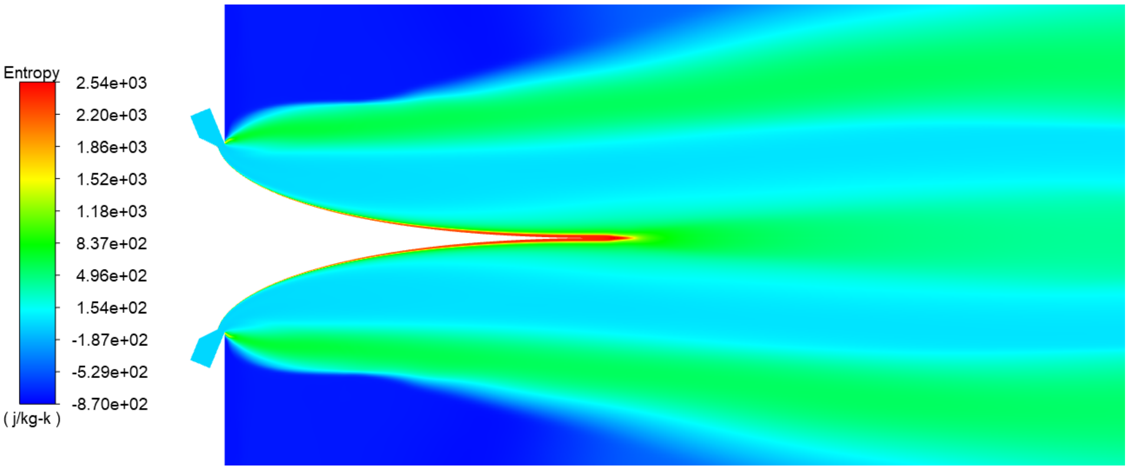

Figure 5.25: Entropy (J/kg.K) contour for turbulent model operating at a 188 PR

The effects of boundary layer generated friction are also evident in other properties contours. Friction causes irreversible work, being particularly visible in the entropy contour shown in Figure 5.25, where at the end of the aerospike's wall, there is a significant generation of this property. This increase in entropy is reflected in a drop in stagnation pressure, as seen in Figure 5.22.

Once again, the static temperature and sound speed contours, as shown in Figures 5.30 and 5.26 respectively, are in agreement. The static temperature near the end of the aerospike reaches high values, which is expected as this region is a zone of stagnation.

Comparing the MN and velocity magnitude contours in Figures 5.27 and 5.28, the effects of the increasing static temperature become evident. In all of the expanding plume, the velocity is mostly constant, except for the thin boundary layer. However, the MN exhibits more pronounced variations due to the local sound speed being affected by the increasing static temperature caused by stagnation.

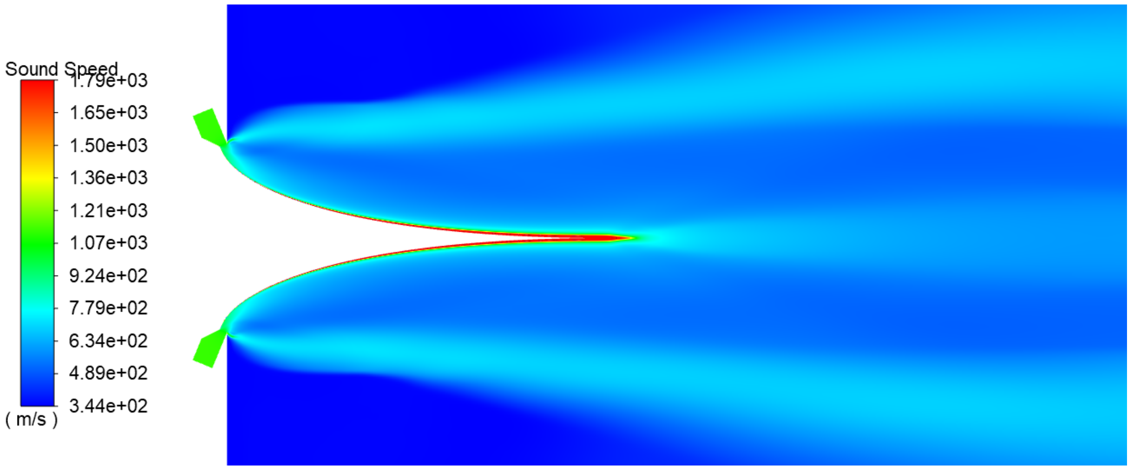

Figure 5.26: Sound speed (m/s) contour for turbulent model operating at a 188 PR

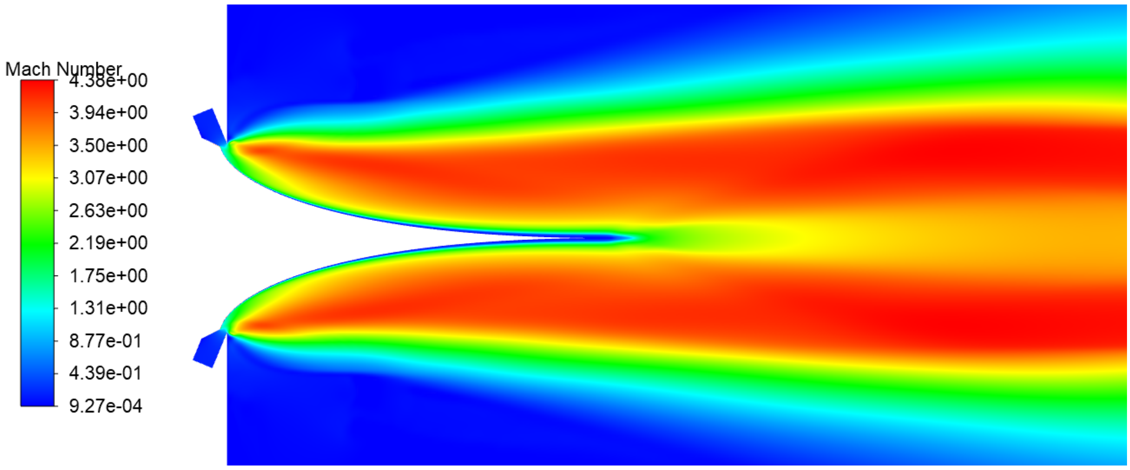

Figure 5.27: Mach number contour for turbulent model operating at a 188 PR

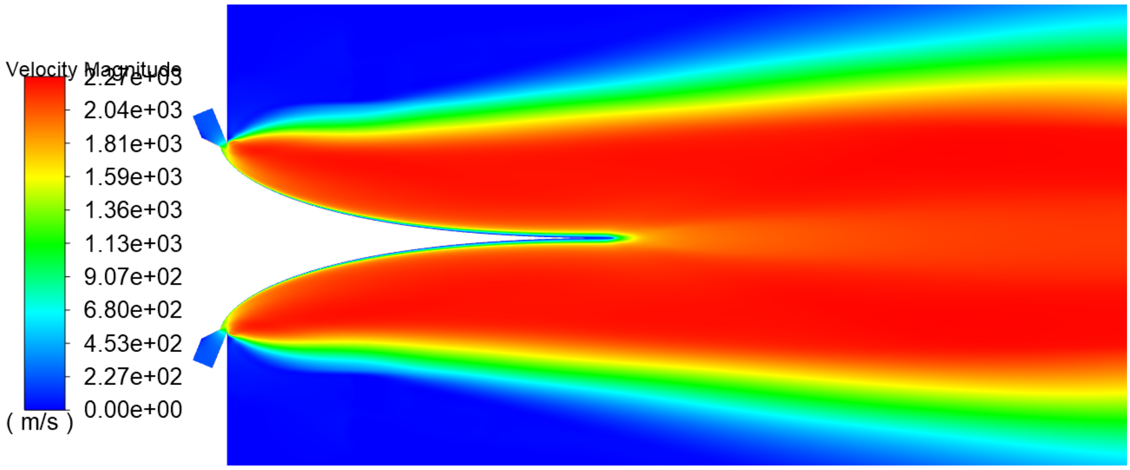

Figure 5.28: Velocity (m/s) contour for turbulent model operating at a 188 PR

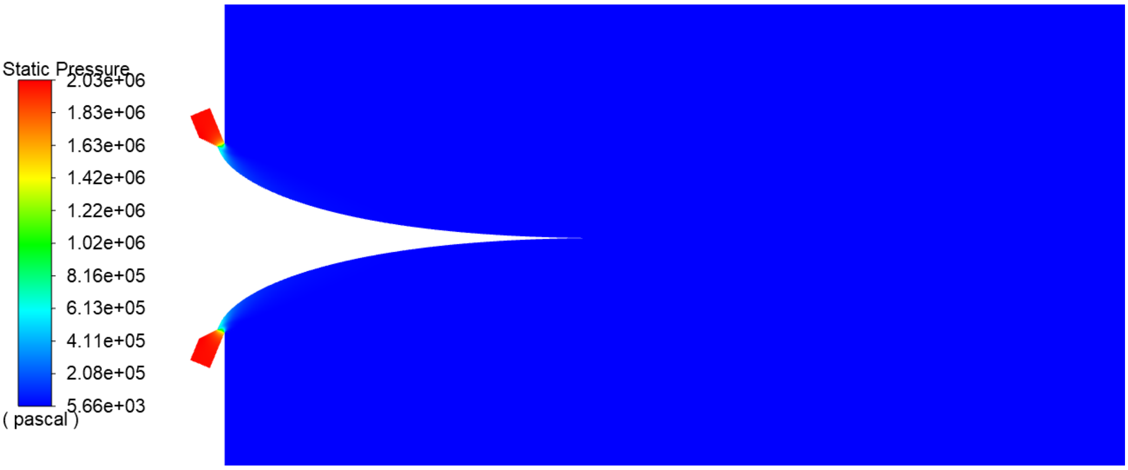

Figure 5.29: Static pressure (Pa) contour for turbulent model operating at a 188 PR

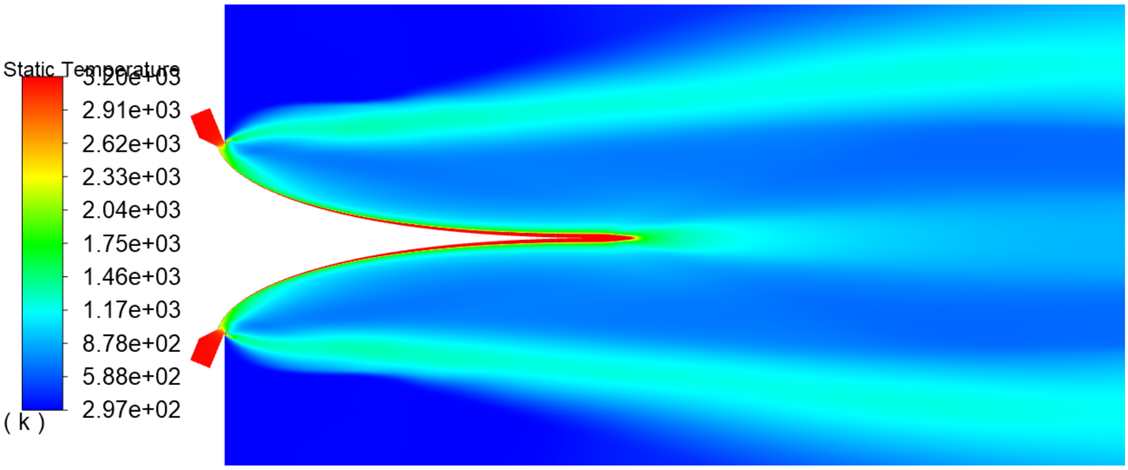

Figure 5.30: Static temperature (K) contour for turbulent model operating at a 188 PR

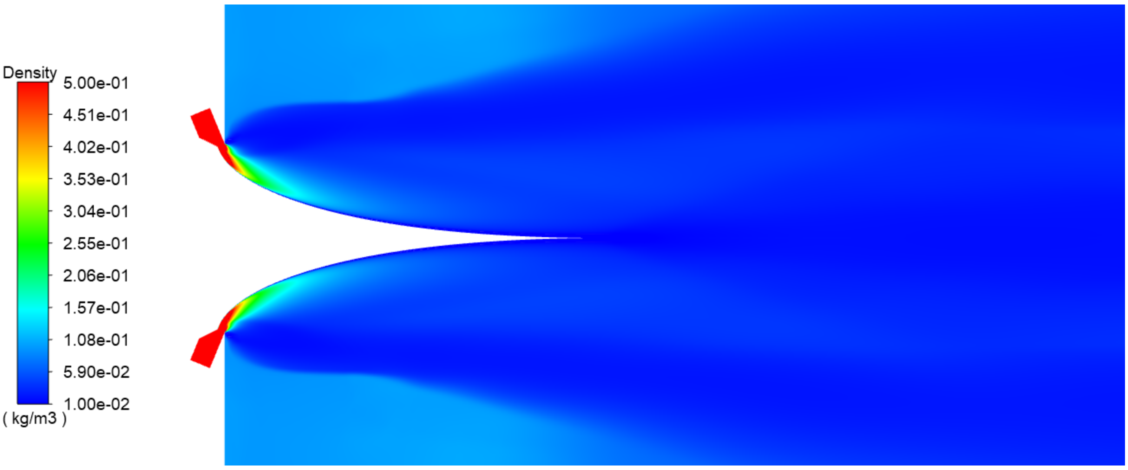

Figure 5.31: Density (kg/m^3) contour for turbulent model operating at a 188 PR

Both the static pressure and density contours, depicted in Figures 5.9 and 5.31 respectively, emphasize the expansion of the flow. The density contour aspect is particularly influenced by pressure, which tends to have higher values compared to temperature. It must be noted that turbulence promotes the mixing of the low density expanded flow with the ambient.

The stream function of Figure 5.32 shows that when turbulence is introduced, its effects reflect on the flow's properties but the streamlines still don't mix between each other.

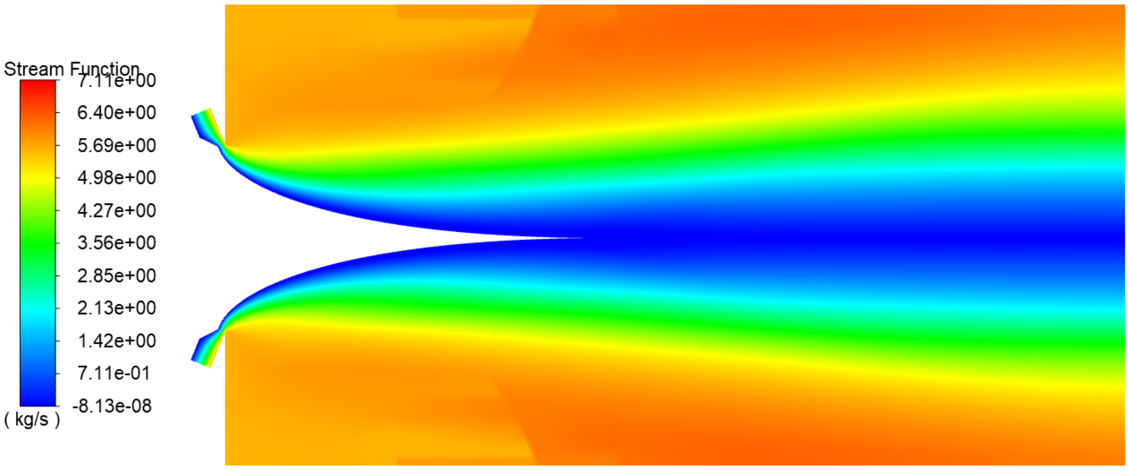

Figure 5.32: Stream function (kg/s) contour for turbulent model operating at a 188 PR

Indeed, despite all the turbulent effects and complexities introduced by considering a turbulent model for viscosity, the simulation results show that the flow passes the exit plane with total axiality. This is clearly evident from the vectors shown in Figure 5.33.

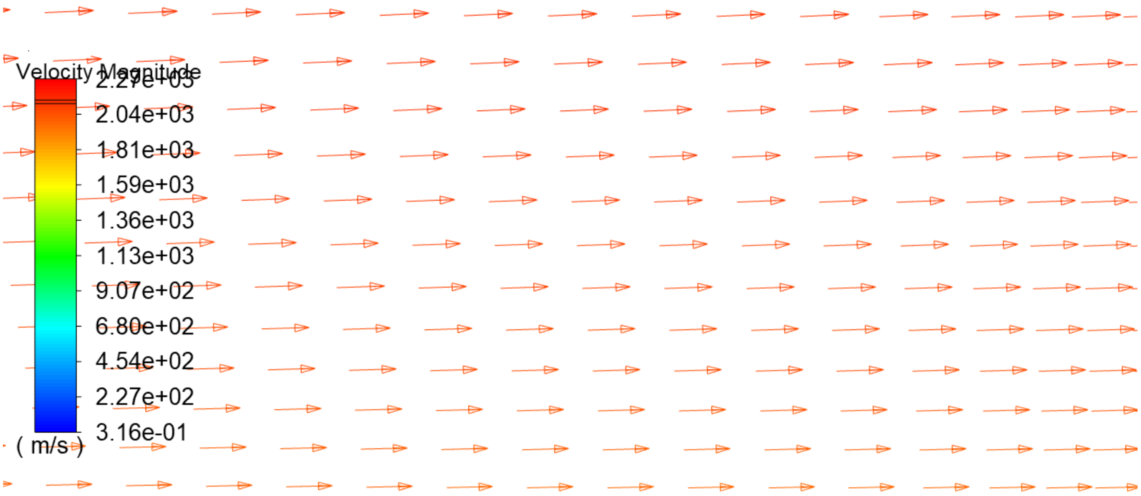

Figure 5.33: Velocity vectors near the end of the spike for inviscid model operating at a 188 PR

5.2.4 Other Turbulent Simulations for Several Operating Altitudes

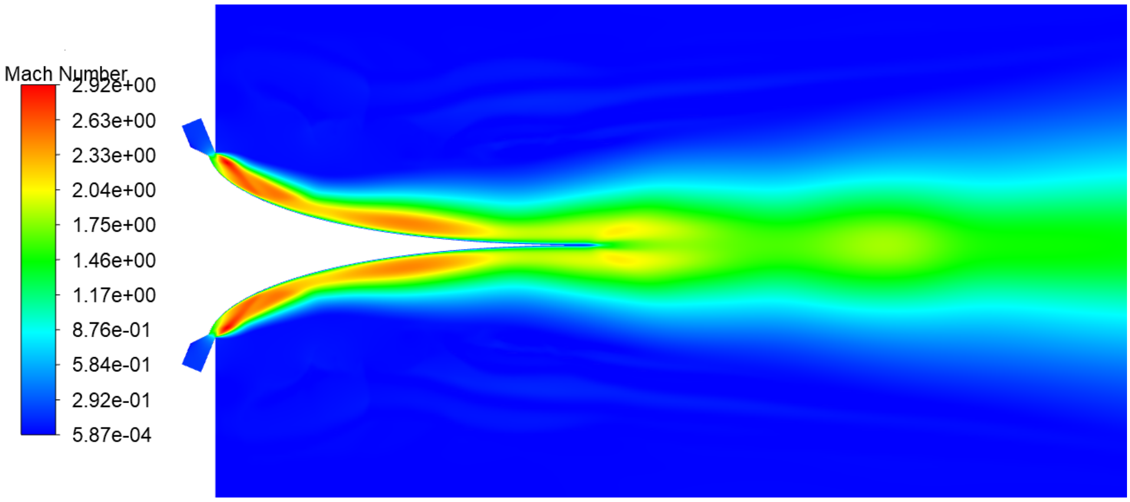

Figure 5.34: Mach number contour for turbulent model operating at a 20 PR

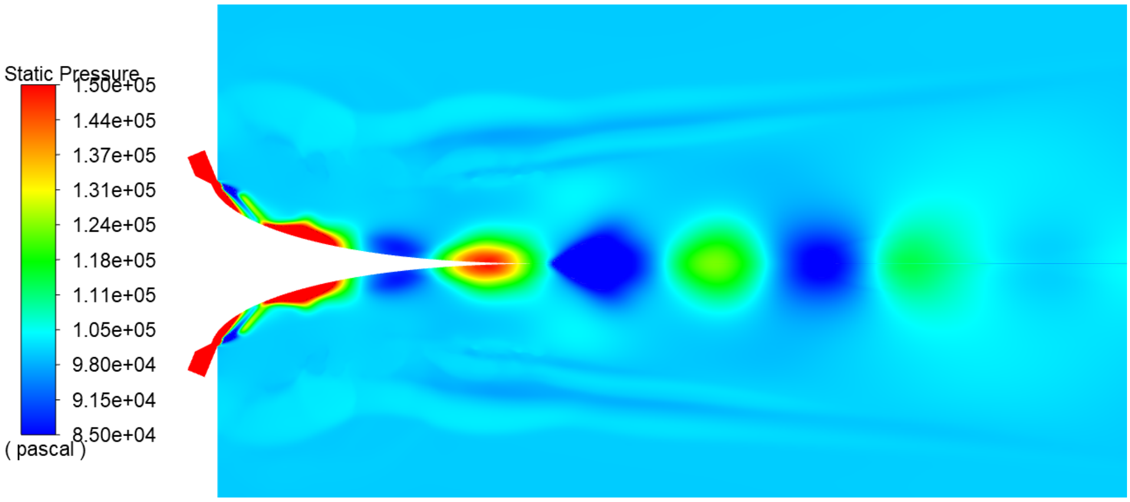

Figure 5.35: Static pressure (Pa) contour for turbulent model operating at a 20 PR

In an overexpanding scenario, the presence of a Mach diamond becomes evident, as shown in Figure 5.34. Flow detachment, which may occur in a full aerospike operating under these conditions, is not observable. Figure 5.35 further illustrates this phenomenon. In contrast to the inviscid case, zones of atmospheric pressure are clearly visible between expansions and compressions.

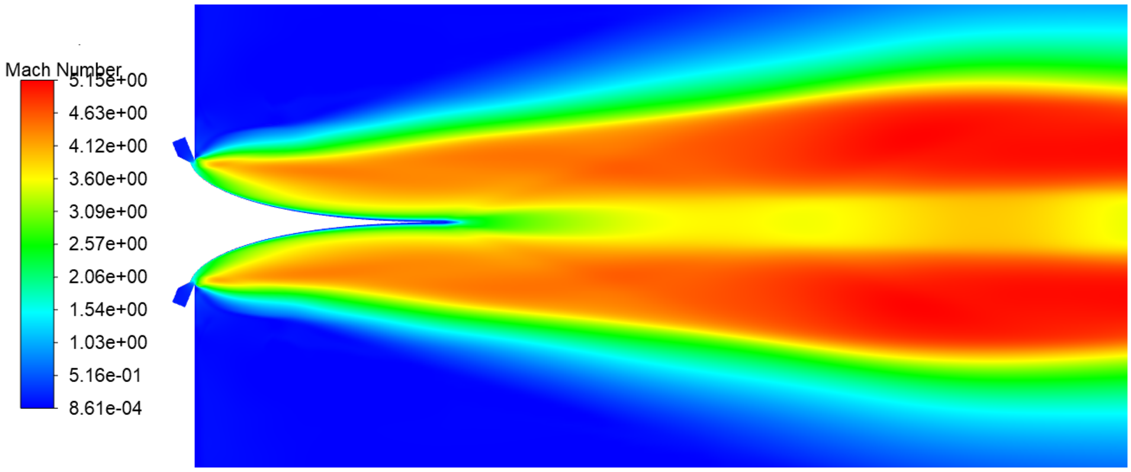

Figure 5.36: Mach number contour for turbulent model operating at a 288 PR

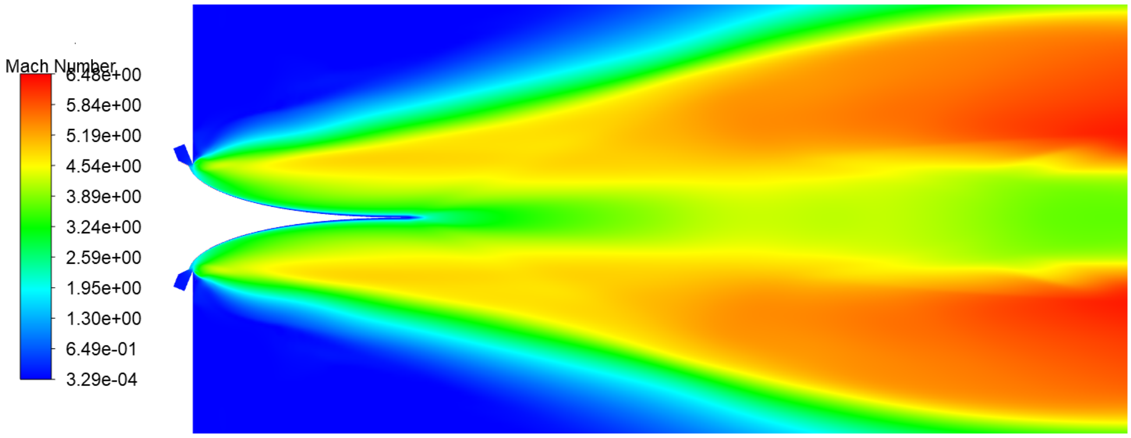

Figure 5.37: Mach number contour for turbulent model operating at a 20480 PR

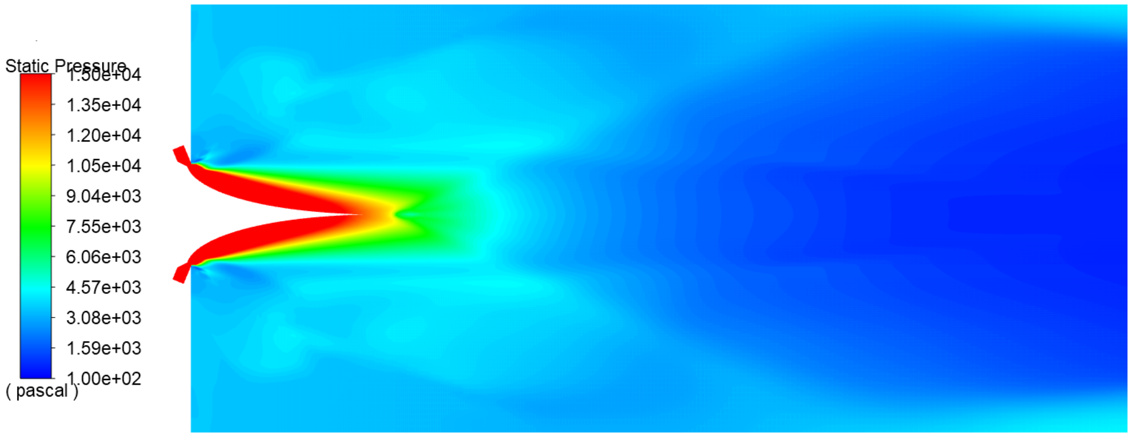

Figure 5.38: Static pressure (Pa) contour for turbulent model operating at a 20480 PR

In underexpanding scenarios, the exit plume widens as the pressure decreases, which is perceivable when comparing Figures 5.36 and 5.37. In the exhaust plume, there are zones of expansion, which are presumably followed by compressions, as seen in the static pressure contour for higher PR operating conditions, shown in Figure 5.38.

Nonetheless, the flow leaves the aerospike relatively axial, as depicted in Figure 5.39. The velocity vector at the exit makes an angle of 7 ° with the horizontal, which only slightly decreases thrust by approximately 1%.

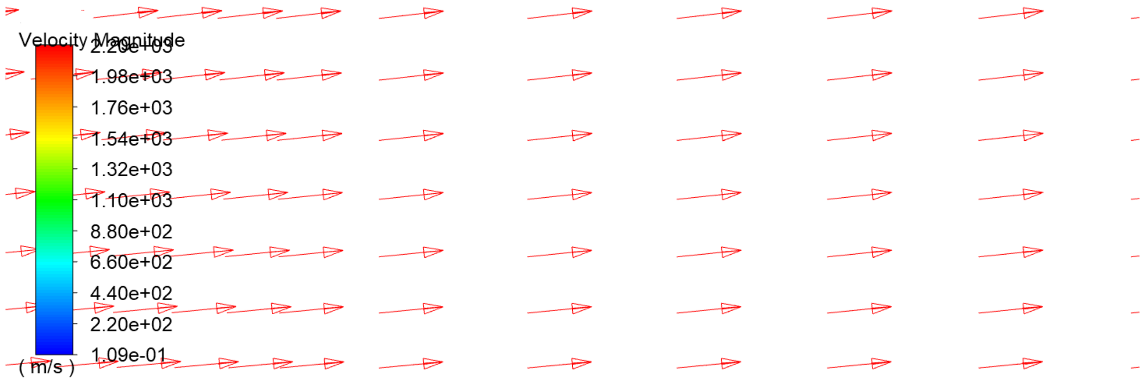

Figure 5.39: Velocity vectors for inviscid model operating at a 20480 PR (similar for turbulent model)

5.2.5 Results Summary

Firstly, examining Figure 5.41, it is evident that the specific impulse for all cases is similar, with the largest discrepancy observed for the Reference [60], but still less than 5%. This discrepancy can be explained by some differences in the implementation. The fact that in the present study, the inviscid case for the design conditions yields a specific impulse very close to the quasi-1D ideal scenario increases confidence in the results.

In fact, for the design operating condition, both the ideal, inviscid, and turbulent cases show a very similar specific impulse, showcasing that the nozzle is well-designed, inducing close to none isentropic losses.

Figure 5.40 presents the specific impulse plotted as a function of altitude for both studied cases, along with a Quasi-1D case. In the Quasi-1D case, it is assumed that the flow expands until it reaches atmospheric pressure, and then exits the nozzle at the corresponding velocity.

In the overexpanding scenario, the inviscid case behaves almost like the ideal nozzle, but the turbulent case does not. In fact, it is in the overexpanding scenario that the turbulent case shows the poorest performance, with losses of 12.6%. This aligns with theoretical knowledge, as the aerospike should have an almost ideal behavior in overexpansion, but without truncation, significant losses can occur due to flow detachment and other dissipative phenomena.

In the underexpansion scenario, the turbulent case closely approaches the performance of the ideal aerospike, with specific impulse losses of less than 2%.

Table 5.2: Parameters' summary of numerical simulations

CASE	M_{exit}	V_{exit} (m/s)	P_{exit} (Pa)	T_{exit} (K)	ρ_{exit} (kg/m^3)	Area-Ratio	$\dot{m}$ kg/s	Thrust (kN)	$\mathrm{I}_s(s)$	C_F
Quasi-1D Analytical (PR=188)	4.16	2229	11030	717	0.054	12.4	11.8	26.9	232.4	3.25
Inviscid Reference [60] (PR=188)	3.46	2235	9256	958	0.038	12.7	9.72	20.9	219	2.55
Inviscid (PR=20)	2.49	1885	99500	1479	0.234	2.90	10.7	20.8	197.3	2.51
Inviscid (PR=188)	3.85	2198	10330	796	0.046	12.5	10.8	24.5	230.4	2.95
Inviscid (PR=288)	3.84	2195	10314	792	0.046	16.3	10.8	24.8	233.4	2.99
Inviscid (PR=20480)	3.91	2199	10330	790	0.045	22.9	10.8	26.2	247.1	3.17
Inviscid mesh x1.25 (PR=188)	3.85	2200	10350	797	0.047	12.3	10.9	24.6	230.7	2.97
Inviscid mesh x1.50 (PR=188)	3.88	2193	10390	792	0.046	12.5	10.9	24.6	230.1	2.96
Turbulent (PR=20)	1.96	1591	117000	1657	0.246	4.6	11.2	19.0	172.6	2.29
Turbulent (PR=188)	4.1	2234.5	11410	790	0.050	14.0	11.2	25.4	231.0	3.06
Turbulent (PR=288)	4.12	2215	11980	724	0.058	16.3	11.2	26.1	237.8	3.15
Turbulent (PR=20480)	4.15	2211	12600	712	0.062	22.4	11.2	27.6	251.2	3.33

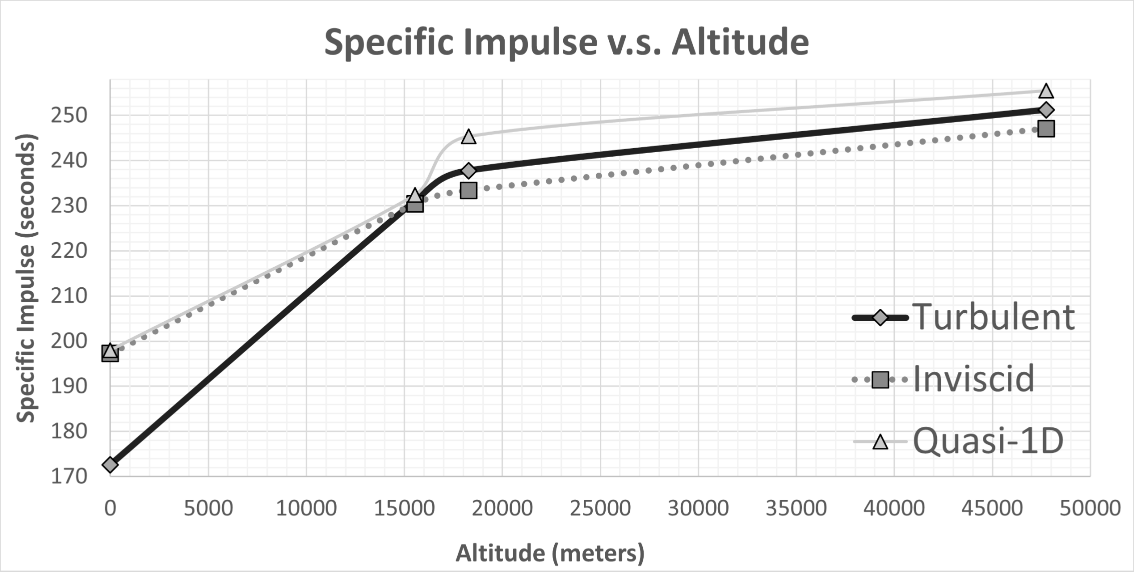

Figure 5.40: Specific impulse comparison for several altitudes

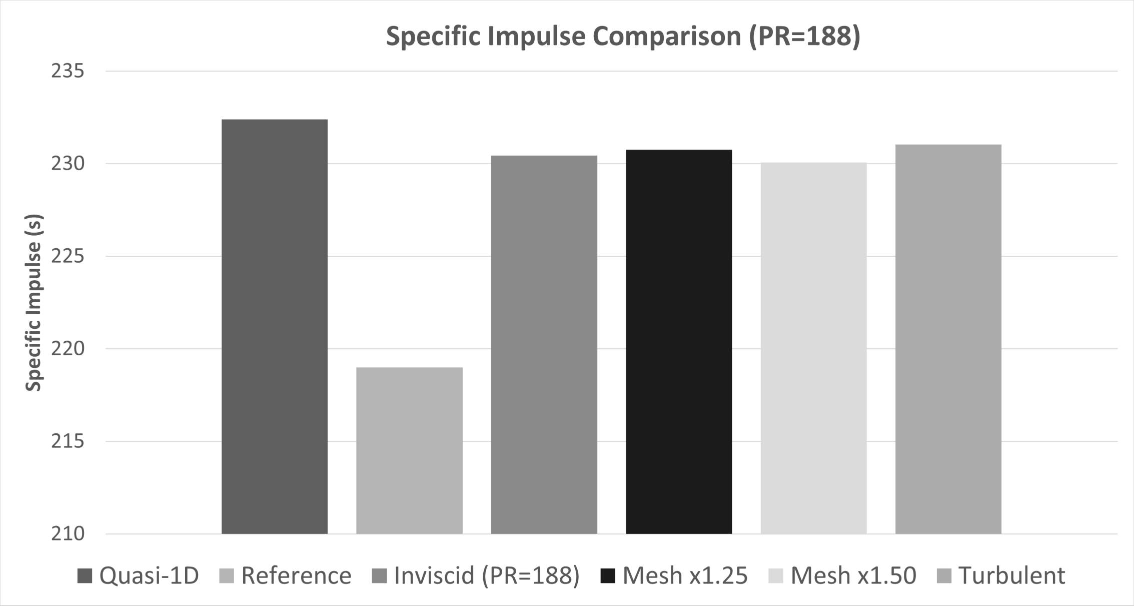

Figure 5.41: Specific impulse comparison for the design altitude

5.2.6 Discussion and Conclusions

When comparing the two viscosity models, it can be observed that the turbulent model closely resembles the expected behavior of an aerospike. At a greater extent, the inviscid model exhibits a Mach line representing the desired MN ($M_{exit} = 4.16$) that connects the lip with the centerline, although not at the tip of the spike but further from it. In contrast, the turbulent model has an exit Mach number that is closer to the design value, with little expansion after it, meaning if the turbulent model is assumed to be closer to the actual aerospike behavior, the designed wall contour (both Angelino's method and implementation) can be validated.

Furthermore, the inviscid model fails to capture important multidisciplinary details, such as the extreme temperatures experienced at wall of the aerospike.

Nonetheless, it is important to note that despite the differences in flow behavior and detailed features, the inviscid model still yields reasonably close results for the prediction of generated specific impulse, as depicted in Figure.

Even at lower PR, the inviscid model contour of pressure exhibits the presence of expansion and compression fans throughout the contour. Anyhow, it should be noted that the inviscid model does not capture the same level of detail and accuracy as the turbulent model, where the flow between the expansion and compression fans reaches the ambient pressure.

Another important point to mention is that the inviscid model solves the flow using a first-order upwind discretization, whereas the turbulent model employs a second-order upwind discretization. This difference in discretization schemes can also contribute to the divergent behavior observed between the two models in capturing flow features.

So, it can be concluded that the turbulent viscosity model yields more accurate results that closely resemble experimental investigations. It captures the detailed flow features and provides a more comprehensive analysis of the aerospike's overall performance. However, if a less detailed and faster analysis is required, the inviscid model can still provide reasonably similar performance results, even though it does not account for turbulent effects, that are important for a multidisciplinary design.

Traditional nozzles lose thrust, especially in underexpanded operation, due to the flow not being axial at the exit plane. When examining the exit flow for a PR=20480, its observed that the angle of the velocity vectors is small, resulting in a thrust reduction of less than 1%. In underexpanded conditions, the specific impulse increases because the flow exits the nozzle at approximately the design velocity and pressure. As a result, the pressure difference between the exhaust gases and the environment contributes positively to generate extra thrust. Essentially, at higher altitudes, the exhaust gases leave the aerospike in a much wider plume, while still maintaining a reasonable axiallity.

At overexpanded conditions, the flow exits the nozzle at a lower MN but with a higher temperature. This higher temperature increases the local sound speed, preventing the exit velocity from being significantly smaller than that at design conditions. Despite the lower MN, the exit velocity remains relatively close to the design condition velocity due to the higher temperature's compensatory effect.

Nevertheless, is in overexpanded condition where the aerospike struggles to achieve an ideal behavior and were it experiences most losses. However, the losses in performance do not make the aerospike less efficient than a traditional nozzle. The aerospike design still showcases its advantages and provides competitive overall performance.

In conclusion, the phenomena mentioned peak the aerospike's capabilities for altitude adaptation, making it a suitable choice for SSTO vehicles.

Chapter 6

Conclusion

In the end of the present disseration, it is safe to infer that all the proposed goals were achieved.

A comprehensive theoretical foundation containing subjects such as compressible aerodynamics, thermodynamics and CFD has been established. Additionally, an extensive review of the state of the art in rocket propulsion has been conducted, covering the history, characterization, limitations, and advancements in the field. This literature review serves as a valuable resource for referencing and consulting.

A Python code capable of designing the contour of an aerospike using Angelino's method was successfully developed and validated. The contour generated by the code was thoroughly compared with another work and numerical simulation, demonstrating its accuracy and reliability. Throughout the process, the complete CFD process was followed with success, and two different approaches for viscosity modelating were utilized and compared, both yielding results that were in good agreement with other studies.

The realizable k-ε turbulence model exhibited excellent flow detail, effectively capturing the complex behavior of the aerospike. It successfully highlighted the aerospike's altitude adaptability, showcasing its capabilities in adjusting to different operating conditions, increasing its specific impulse with altitude.

6.1 Limitations

The major limitation encountered during the development of this dissertation was time. The project was intended to be completed within the span of one semester, allowing for four months of work.

Time constraints imposed significant challenges during the numerical studies, especially in terms of selecting appropriate simulation geometry, mesh refinement and parameter settings to ensure convergence of the results. The simulation process required a considerable amount of time to generate meaningful and accurate data. Consequently, due to time limitations, it was only possible to investigate four operating conditions and utilize two viscosity models. Despite these constraints, valuable insights and conclusions were still obtained within the scope of the available time.

Nonetheless, it must be recognized that the extensive published literature on aerospike nozzles greatly contributed to the understanding and development of this work. The existing collection of knowledge provided valuable insights and served as a foundation for the analysis and interpretation of the results obtained in this dissertation.

6.2 Future Work

There are several ways to further development this work, with the immediate focus being on expanding the range of operating conditions for the same aerospike contour. By exploring a wider range of pressure ratios and other relevant parameters, a more comprehensive understanding of the aerospike's performance can be achieved.

Additionally, it would be beneficial to incorporate truncation effects into the analysis. By considering the influence of base pressure effects on the overall performance of the aerospike, a more accurate assessment of its capabilities can be obtained, knowing the truncation can eliminate extreme heat flows and reduces weight.

Once additional results are available, including nozzles designed for different altitudes, a comprehensive multidisciplinary assessment should be conducted to determine the optimal solution. This assessment would involve considering various factors such as performance, efficiency, structural integrity and cost. By integrating inputs from different disciplines, such as aerodynamics, thermodynamics, structural analysis and economics, a more informed decision can be made and depart to experimental studies with commercial applications at sight.

Bibliography

[1] G. B. Sanders, “Space Resource Utilization: Technologies and Potential Synergism with Terrestrial Mining,” May 2015. [Online]. Available: https://ntrs.nasa.gov/api/citations/20150003499/downloads/20150003499.pdf. 1

[2] G. Hagemann, H. Immich, T. van Nguyen, and G. Dumnov, “Advanced rocket nozzles,” *Journal of Propulsion and Power*, vol. 14, pp. 620–633, Sept. 1998. 1, 14, 15, 17, 18, 19, 20, 21, 23, 24, 25, 26, 28

[3] P. P. Nair, A. Suryan, and H. D. Kim, “Computational study of performance characteristics for truncated conical aerospike nozzles,” *Journal of Thermal Science*, vol. 26, pp. 483–489, Nov. 2017. DOI: 10.1007/s11630-017-0965-0. 1, 18, 23, 24

[4] T. Bui, J. Murray, C. Rogers, S. Bartel, A. Cesaroni, and M. Dennett, “Flight research of an aerospike nozzle using high power solid rockets,” in *41st AIAA/ASME/SAE/ASEE Joint Propulsion Conference & Exhibit*, American Institute of Aeronautics and Astronautics, July 2005. DOI: 10.2514/6.2005-3797. 2

[5] A. F. El-Sayed, “Rocket propulsion,” in *Fundamentals of Aircraft and Rocket Propulsion*, pp. 907–991, Springer London, May 2016. DOI: 10.1007/978-1-4471-6796-9_11. 6, 7, 8

[6] J. Kluger, “Billionaires Are Racing to Space — and the Climate is Paying the Price ,” June 2022. [Online]. Available: https://time.com/6191846/billionaire-space-race-climate/. 6

[7] G. V. R. RAO, “Recent developments in rocket nozzle configurations,” *ARS Journal*, vol. 31, pp. 1488–1494, Nov. 1961. DOI: 10.2514/8.5837. 8, 9

[8] S. Khare and U. K. Saha, “Rocket nozzles: 75 years of research and development,” *Sādhanā*, vol. 46, Apr. 2021. DOI: 10.1007/s12046-021-01584-6. 8, 10, 11, 12

[9] G. Sutton and O. Biblarz, *Rocket Propulsion Elements*. A Wiley Interscience publication, Wiley, 2001. ISBN: 9780471326427. 10, 11, 13

[10] G. V. R. RAO, “Exhaust nozzle contour for optimum thrust,” *Journal of Jet Propulsion*, vol. 28, pp. 377–382, June 1958. DOI: 10.2514/8.7324. 11, 28, 29

[11] J. *Ö*stlund and B. Muhammad-Klingmann, “Supersonic flow separation with application to rocket engine nozzles,” *Applied Mechanics Reviews*, vol. 58, pp. 143–177, May 2005. DOI: 10.1115/1.1894402. 11

[12] M. Frey and G. Hagemann, “Critical assessment of dual-bell nozzles,” *Journal of Propulsion and Power*, vol. 15, pp. 137–143, Jan. 1999. DOI: 10.2514/2.5402. 16, 17

[13] R. H. Schmucker, “Flow processes in overexpanded chemical rocket nozzles. Part 1: Flow separation,” in *NASA Technical Reports Server*, Technische Univ. Munich, Germany, July 1973. [Online]. Available: https://ntrs.nasa.gov/citations/19750017939. 17

[14] N. Goncharov, V. Orlov, V. Rachuk, A. Shostak, and R. Starke, “Reusable launch vehicle propulsion based on the RD-0120 engine,” in *31st Joint Propulsion Conference and Exhibit*, American Institute of Aeronautics and Astronautics, July 1995. DOI: 10.2514/6.1995-3003. 17

[15] D. Chasman, M. Birch, S. Haight, and R. Graffam, “A multi-disciplinary optimization method for multi nozzle grid (MNG) design - final report,” in *43rd AIAA Aerospace Sciences Meeting and Exhibit*, American Institute of Aeronautics and Astronautics, Jan. 2005. DOI: 10.2514/6.2005-706. 22

[16] A. Ferrero, A. Conte, E. Martelli, F. Nasuti, and D. Pastrone, “Dual-bell nozzle with fluidic control of transition for space launchers,” *Acta Astronautica*, vol. 193, pp. 130–137, Apr. 2022. DOI: 10.1016/j.actaastro.2021.12.048. 22

[17] N. Taylor, J. Steelant, and R. Bond, “Experimental comparison of dual bell and expansion deflection nozzles,” in *47th AIAA/ASME/SAE/ASEE Joint Propulsion Conference &ampamp Exhibit*, American Institute of Aeronautics and Astronautics, July 2011. DOI: 10.2514/6.2011-5688. 23, 26

[18] J. P. P., P. P. Nair, A. Suryan, J. P. M. M, and H. D. Kim, “Numerical simulation on optimization of pintle base shape in planar expansion-deflection nozzles,” *Journal of Spacecraft and Rockets*, vol. 57, pp. 539–548, May 2020. DOI: 10.2514/1.a34559. 23

[19] Y. Wang, Y. Lin, Q. Eri, and B. Kong, “Flow and thrust characteristics of an expansion–deflection dual-bell nozzle,” *Aerospace Science and Technology*, vol. 123, p. 107464, Apr. 2022. DOI: 10.1016/j.ast.2022.107464. 23

[20] S. Corda, *Flight Testing the Linear Aerospike SR-71 Experiment (LASRE)*. NASA technical memorandum, NASA Dryden Flight Research Center, 1998. [Online]. Available: https://books.google.pt/books?id=mbM3AQAAMAAJ. 23

[21] J. Scott, “Aerospike Aerodynamics,” Oct. 1999. [Online]. Available: https://aerospaceweb.org/design/aerospike/aerodynamics.shtml. 24

[22] A. Lai, S. S. Wei, C. H. Lai, J. L. Chen, Y. H. Liao, J. S. Wu, and Y. S. Chen, “Comparison of the propulsion performance of aerospike and bell-shaped nozzle using hydrogen peroxide monopropellant under sea-level condition,” *Journal of Mechanics*, vol. 35, pp. 427–440, July 2018. DOI: 10.1017/jmech.2018.18. 26

[23] T. Mizukaki and S. Watabe, “Visualization of stagnation point inside the closed wake of a 20%-truncated plug nozzle at starting process,” *Aerospace Science and Technology*, vol. 50, pp. 25–30, Mar. 2016. DOI: 10.1016/j.ast.2015.12.013. 26, 27

[24] T. Ito and K. Fujii, “Numerical analysis of the base bleed effect on the aerospike nozzles,” in *40th AIAA Aerospace Sciences Meeting &amp Exhibit*, American Institute of Aeronautics and Astronautics, Jan. 2002. DOI: 10.2514/6.2002-512. 26

[25] G. Hagemann, H. Immich, and M. Terhardt, “Flow phenomena in advanced rocket nozzles - the plug nozzle,” in *34th AIAA/ASME/SAE/ASEE Joint Propulsion Conference and Exhibit*, American Institute of Aeronautics and Astronautics, July 1998. DOI: 10.2514/6.1998-3522. 26

[26] M. C. Karia, M. A. Popat, and K. B. Sangani, “Selective laser melting of Inconel super alloy-a review,” in *AIP Conference Proceedings*, July 2017. DOI: 10.1063/1.4990166. 26

[27] H. F. R. Schoyer, “Thrust vector control for (clustered modules) plug nozzles: Some considerations,” *Journal of Propulsion and Power*, vol. 16, pp. 196–201, Mar. 2000. DOI: 10.2514/2.5583. 27

[28] C. Bach, J. Sieder-Katzmann, M. Propst, and M. Tajmar, “Evaluation of the performance potential of aerodynamically thrust vectored aerospike nozzles,” Sept. 2016. 27

[29] N. Erni, C. Frazier, and D. Baker, “Attitude control using aerodynamic vectoring on an aerospike nozzle,” Nov. 2011. 27, 28

[30] C. Aukerman, “Plug nozzles - The ultimate customer driven propulsion system,” in *27th Joint Propulsion Conference*, American Institute of Aeronautics and Astronautics, June 1991. DOI: 10.2514/6.1991-2208. 27

[31] Ansys, “Method of Characteristics - Internal Compressible Flows – Lesson 6,” Nov. 2020. [Online]. Available: https://courses.ansys.com/index.php/courses/internal-compressible-flows/lessons/method-of-characteristics-lesson-6/. 28, 52, 53, 54

[32] K. Foelsch, “The analytical design of an axially symmetric laval nozzle for a parallel and uniform jet,” *Journal of the Aeronautical Sciences*, vol. 16, pp. 161–166, Mar. 1949. DOI: 10.2514/8.11758. 29

[33] L. V. Gogish, “A study of short supersonic nozzles,” *Fluid Dynamics*, vol. 1, pp. 122–126, Mar. 1968. DOI: 10.2514/8.11758. 29

[34] J. D. Hoffman, “Design of compressed truncated perfect nozzles,” *Journal of Propulsion and Power*, vol. 3, pp. 150–156, Mar. 1987. DOI: 10.2514/3.22967. 29

[35] M. Nazarinia, A. Naghib-Lahouti, and E. Tolouei, "Design and numerical analysis of aerospike nozzles with different plug shapes to compare their performance with a conventional nozzle," Mar. 2005. 29, 67

[36] H. Greer, "Rapid method for plug nozzle design," *ARS Journal*, vol. 31, pp. 560–561, Apr. 1961. 30, 63

[37] G. Angelino, "Approximate method for plug nozzle design," *AIAA Journal*, vol. 2, pp. 1834–1835, Oct. 1964. DOI: 10.2514/3.2682. 30, 63, 64, 65

[38] D. Garanin, "Thermodynamics," Feb. 2021. [Online]. Available: https://www.lehman.edu/faculty/dgaranin/Statistical_Thermodynamics/Thermodynamics.pdf. 31, 32, 33, 34, 35

[39] M. Bahrami, "The Second Law of Thermodynamics," Sept. 2011. [Online]. Available: https://www.sfu.ca/ mbahrami/ENSC%20388/Notes/Second%20Law%20of %20Thermodynamics.pdf. 35

[40] M. Bahrami, "Entropy," Sept. 2011. [Online]. Available: https://www.sfu.ca/ mbahrami/ENSC%20388/Notes/Entropy.pdf. 36

[41] R. W. Fox, A. T. McDonald, and P. J. Pritchard, *Introduction to Fluid Mechanics*. 6^{th} edition, John Wiley Sons, Inc., 2004. ISBN: 978-0471202318. 37

[42] J. Anderson, *Modern Compressible Flow, with Historical Perspective*. McGraw-Hill series in Aeronautical and Aerospace Engineering, McGraw-Hill, 1982. ISBN: 9780070016545. 37, 39, 41, 43, 44, 45, 46, 50, 53, 55

[43] A. A. Hussaini, "Chapter Eleven/Normal shock in converging–diverging nozzles ," Sept. 2013. [Online]. Available: https://cnj.atu.edu.iq/wp-content/uploads/2019/09/Gas-Dynamic-3.pdf . 48

[44] A. A. Hussaini, "Chapter Sixteen / Plug, Underexpanded and Over-expanded Supersonic Nozzles," Sept. 2013. [Online]. Available: https://cnj.atu.edu.iq/wp-content/uploads/2020/03/Gas-Dynamic-4.pdf . 50

[45] N. Hampl, "Advanced simulation techniques in vehicle noise and vibration refinement," in *Vehicle Noise and Vibration Refinement*, pp. 174–188, Elsevier, 2010. DOI: 10.1533/9781845698041.2.174. 55

[46] Ansys, "Conservation of Mass Equation -Governing Equations of Fluid Dynamics – Lesson 3," Dec. 2019. [Online]. Available: https://courses.ansys.com/index.php/courses/governing-equations-of-fluid-dynamics/lessons/conservation-of-mass-equation-lesson-3/. 55

[47] Ansys, "Conservation of Momentum Equations - Governing Equations of Fluid Dynamics – Lesson 4," Dec. 2019. [Online]. Available:

https://courses.ansys.com/index.php/courses/governing-equations-of-fluid-dynamics/lessons/conservation-of-momentum-equations-lesson-4/. 56

[48] Ansys, “Conservation of Energy Equation - Governing Equations of Fluid Dynamics – Lesson 5,” Dec. 2019. [Online]. Available: https://courses.ansys.com/index.php/courses/governing-equations-of-fluid-dynamcs/lessons/conservation-of-energy-equation-lesson-5/. 56

[49] J. W. Slater, “CFD Analysis Process,” Feb. 2021. [Online]. Available: https://www.grc.nasa.gov/www/wind/valid/tutorial/process.html. 57

[50] MIT, “Basics of Turbulent Flow.” [Online]. Available: http://web.mit.edu/1.061/www/dream/SEVEN/sevenpage.htm. 58

[51] L. Davidson, “An Introduction to Turbulence Models,” Aug. 2022. [Online]. Available: https://www.tfd.chalmers.se/ lada/postscript_files/kompendium_turb.pdf. 59

[52] Ansys, “Ansys Fluent Theory Guide,” July 2021. [Online]. Available: https://dl.cfdexperts.net/cfd_resources/Ansys_Documentation/Fluent/Ansys_Fluent_Theory_Guide.pdf. 60, 61

[53] C.-H. Wang, Y. Liu, and L.-Z. Qin, “Aerospike nozzle contour design and its performance validation,” *Acta Astronautica*, vol. 64, pp. 1264–1275, June 2009. DOI: 10.1016/j.actaastro.2008.01.045. 65

[54] K. N. Kumar, M. Gopalsamy, D. Antony, R. Krishnaraj, and C. B. V. Viswanadh, “Design and optimization of aerospike nozzle using CFD,” *IOP Conference Series: Materials Science and Engineering*, vol. 247, p. 012008, Oct. 2017. DOI: 10.1088/1757-899x/247/1/012008. 65

[55] S. Dakka and O. Dennison, “Numerical analysis of aerospike engine nozzle performance at various truncation lengths,” *International Journal of Aviation, Aeronautics, and Aerospace*, June 2021. DOI: 10.15394/ijaaa.2021.1601. 65

[56] D. H. C. M. S. S. Ayub Padania, Sanjay Kumar Sardiwal and S. Artham, “Numerical solution for the design of a traditional aerospike nozzle using method of characteristics,” *IOSR Journal of Mechanical and Civil Engineering (IOSR-JMCE)*, Feb. 2015. [Online]. Available: https://www.iosrjournals.org/iosr-jmce/papers/vol12-issue1/Version-4/L012146369.pdf . 65

[57] M. Reedy, “The Most Popular Coding Languages Used In Aerospace,” Dec. 2021. [Online]. Available: https://www.ilovelanguages.com/the-most-popular-coding-languages-used-in-aerospace/. 65

[58] M. S. Khoirom, M. Sonia, B. Laikhuram, J. Laishram, and T. D. Singh, "Comparative analysis of Python and Java for beginners," 2020. [Online]. Available: https://www.semanticscholar.org/paper/Comparative-Analysis-of-Python-and-Java-for-Khoirom-Sonia/d787d59179cc56b412fd880fe407b3c1cbca71c5. 66

[59] P. Nagarajan and T. D.Kulandaivel, *Numerical Simulation of Truncated Aerospike Nozzle*, vol. 7 of *Issue 3*, pp. 1810–1814. Someplace: International Journal of Scientific Research Engineering Trends, 1 ed., may 2021. [Online]. Available: https://ijsret.com/wp-content/uploads/2021/05/IJSRET_V7_issue3_432.pdf. 67

[60] S. Khan, A. Khan, and A. Munir, "Design and analysis approach for linear aerospike nozzle," *Science Vision*, vol. 20, pp. 25 – 37, 07 2014. [Online]. Available: https://www.researchgate.net/publication/280342589_Design_and_Analysis_Approach_for_Linear_Aerospike_Nozzle. 71, 73, 74, 79, 80, 91, 92

Appendix A

Python Algorithm

```
#author: João Cristóvão, Universidade da Beira Interior

import math
import numpy as np
import matplotlib.pyplot as plt
import pandas as pd

""" The user inputs the flow's adiabatic index, aerospike exit mach
and the number of characteristic lines.
Each characteristic line will correspond to a close interval partisian
between M=1 and M=M_exit
For each M number, a length and inclination will be given to the
characteristic line.
In the end, the aerospike countour will be built and both an image and an Excell
file will be exported.
!!Everything is dimensionless by the throat diameter
"""

def main():
#user defined values
    gamma, M_exit, n_char_lines = get_values()
#coordenates of the lip
    lip_coord = [0 , 3]
# step between each charatrictic line
    m_disc = (M_exit - 1) / (n_char_lines - 1)
#iniciate the matrix [Mach, length, angle] and the throat Mach number
    flow_field = np.zeros(shape=(n_char_lines, 3))
    M=1
    pm_angle_exit = pm_angle(M_exit, gamma)
#calculate the length and angle of the mach lines and pressure ration
    for line in range (n_char_lines):
        flow_field[line,0] = M
        flow_field[line,1] = M*epsilon(M, gamma)
        flow_field[line,2] = pm_angle_exit+mach_angle(M)-pm_angle(M, gamma)
        M=M+m_disc
    PR=(1+0.5*(gamma-1)*(M_exit**2))**(gamma/(gamma-1))
#generate the points, then draw the contour and save it
    points, lip_coord = set_point(flow_field, lip_coord)
```

```
    draw_figure(points,lip_coord)
    simulation = f”me_{M_exit}_gamma_{gamma}_nchar_{n_char_lines}”
    export_points(points, lip_coord, simulation, PR, pm_angle_exit)


#FUNCTIONS


def get_values():
    #get the values from the user
    while True:
        try:
            gamma = float(input (”Define the Adiabatic Coeficient => ”))
            M_exit = float(input(”Define the Mach Number at the exit => ”))
            n_char_lines = int(input(”Define the Number of Characteristic Lines => ”))
        except ValueError:
            print(”Invalid Usage”)
        if 1<gamma<2 and 1<M_exit<5 and n_char_lines>2:
            break
    return gamma, M_exit, n_char_lines


def epsilon(mach, gamma):
#returns the area ratio needed to expand until M=mach
    A = 1/(mach**2)
    B = 2*(1+0.5*(gamma-1)*mach**2)/(gamma+1)
    C =(gamma+1)/(gamma-1)
    epsilon = math.sqrt(A*(B**C))
    return epsilon


def pm_angle(mach, gamma):
#returns the Prandtl-Meyer angle
    A = math.sqrt((gamma+1)/(gamma-1))
    B = math.atan(math.sqrt((gamma-1)*(mach**2-1)/(gamma+1)))
    C = math.atan(math.sqrt(mach**2-1))
    pm = A*B-C          #rad
    return pm



def mach_angle(mach):
#returns the mach angle
    miu = math.asin(1/mach)   #rad
    return miu

```

```


def set_point(flow, P):
#creating the points
    size = len(flow)
    points = np.zeros(shape=(size, 2))
    for point in range(size):
        points[point, 0] = P[0]+math.cos(flow[point, 2])*flow[point, 1]    #x
        points[point, 1] = P[1]-math.sin(flow[point, 2])*flow[point, 1]    #y
#moving the geometry to a ref where x_first_pint=0 and y_last_point=0
    new_x=points[0,0]
    new_y=points[size-1,1]
    for point in range(size):
        points[point, 0] = points[point, 0] - new_x    #x
        points[point, 1] = points[point, 1] - new_y    #y
    new_lip_coord=[0,0]
    new_lip_coord[0]=P[0]-new_x
    new_lip_coord[1]=P[1]-new_y
    return points, new_lip_coord

def draw_figure(points, P):
#it will draw the nozzle contour
#the lip
    P_1 = [P[0]+0.02, P[1]+0.02]
    P_2 = [P[0]-0.3, P[1]+0.02]
    plt.plot([P[0], P_2[0]],[P[1], P_2[1]], color=”blue”)
    plt.plot([P[0], P_1[0]],[P[1], P_1[1]], color=”blue”)
    plt.plot([P_1[0], P_2[0]],[P_1[1], P_2[1]], color=”blue”)
#plot the countour
    plt.plot(points[:,0],points[:,1], color= ”black” )
#plot the char lines
    for point in points:
        plt.plot([P[0], point[0]],[P[1], point[1]], color=”red”, linewidth=1)
    plt.show()


def export_points(points, P, file_name, PR, pm_angle_exit):
# creating the DataFrame of pandas library
    save_points = pd.DataFrame(points, columns=[”X”, ”Y”])
    save_lip = pd.DataFrame(P)
    save_pr=pd.DataFrame([PR])
    save_pm_exit=pd.DataFrame([math.degrees(pm_angle_exit)])
# exporting to an Excell file for redundancy
    with pd.ExcelWriter(f”{file_name}.xlsx”) as writer:
        save_points.to_excel(writer, sheet_name=”Contour”)
        save_lip.to_excel(writer, sheet_name=”Lip”)
        save_pr.to_excel(writer, sheet_name=”Pressure Ratio”)
```

```
        save_pm_exit.to_excel(writer, sheet_name=”Angle of the Throat  ”)
# export txt file with coordenates
    with open(f”{file_name}.txt”, ’w’) as f:
        n=1
        f.write(”polyline=true”)
        f.write(’\n’)
        f.write(”3d=false”)
        f.write(’\n’)
        for line in points:
            f.write(f”{int(1)} {line[0]} {line[1]}”)
            f.write(’\n’)
            n=n+1


if __name__==”__main__”:
    main()
```